UNIVERSITÀ DEGLI STUDI DI ROMA "TOR VERGATA"

FACOLTA' D'INGEGNERIA ELETTRONICA

DOTTORATO DI RICERCA IN

ING. DELLE TELECOMUNICAZIONI E MICROELETTRONICA

CICLO DEL CORSO DI DOTTORATO

XXII

Sealing materials - Encapsulation procedures and Ageing tests for Dye sensitized solar cells

Nome e Cognome del dottorando

ENRICO LEONARDI

A.A. 2009/2010

Docente Guida/Tutor: Prof. ALDO DI CARLO & Prof. ANREA REALE

Coordinatore: Prof. GIUSEPPE BIANCHI

A LONG TIME AGO,

IN A GALAXY FAR,

FAR AWAY…

Summary

Table of figures

1. Introduction

Photoelectrochemical solar cells (PSCs) have been studied extensively. Several semiconductor materials, including single-crystal and polycrystal forms of *n*- and *p*-Si, *n*- and *p*-GaAs, *n*- and *p*-InP, and *n*-CdS, have been used as photoelectrodes. These materials, when used with a suitable redox electrolyte, can produce solar light-to-current conversion efficiency of approximately 10%. However, under irradiation, photocorrosion of the electrode in the electrolyte solution frequently occurs, resulting in poor stability of the cell, so efforts have been made worldwide to develop more stable PSCs.

Oxide semiconductor materials have good stability under irradiation in solution. However, stable oxide semiconductors cannot absorb visible light because they have relatively wide band gaps. Sensitization of wide band gap oxide semiconductor materials, such as TiO2, ZnO, and SnO2, with photosensitizers, such as organic dyes, that can absorb visible light has been extensively studied in relation to the development of photography technology since the late nineteenth century. In the sensitization process, photosensitizers adsorbed onto the semiconductor surface absorb visible light and excited electrons are injected into the conduction band of the semiconductor electrodes. Dye-sensitized oxide semiconductor photoelectrodes have been used for PSCs.

Gerischer and Tributsch studied a ZnO electrode sensitized by organic dyes including rose bengal, fluorescein, and rhodamine B [(1) (2)]. In early studies, however, singlecrystal and polycrystal materials, which cannot adsorb a large amount of dye, were used for the photoelectrode, which resulted in low light-harvesting efficiency (LHE) and, consequently, low photon-to-current conversion efficiencies. Additionally, the organic dyes that were used had a narrow absorption range in visible light, which also contributed to low solar cell performance. Thus, to improve light-harvesting efficiencies and cell performance, researchers used two approaches: developing photoelectrodes with larger surface areas that could adsorb large amount of dye and synthesizing dyes with broader absorption ranges. Significant improvements in the performance of a dye-sensitized solar cell (DSC, or Graetzel

cell) have been mainly due to the development of high-performance nanoporous TiO_2 thin-film electrodes that have a large surface area capable of adsorbing a large amount of photosensitizer, and due to the synthesis of new Ru complex photosensitizers capable of absorbing in the wide visible and near-IR region from 400 to 800 or 900 nm.

Ru bipyridyl complexes are suitable photosensitizers because the excited states of the complexes have long lifetimes and oxidized Ru(III) has long-term chemical stability. Therefore, Ru bipyridyl complexes have been studied intensively as photosensitizers for homogeneous photocatalytic reactions and dye-sensitization systems. An Ru bipyridyl complex, bis(2,2'_-bipyridine)(2,2'_-bipyridine-4,4'_-dicarboxylate)ruthenium(II), having carboxyl groups as anchors to adsorb onto the semiconductor surface, was synthesized and single-crystal TiO_2 photoelectrodes sensitized by the Ru complex were studied in 1979 to 1980 [(3), (4)].

Recent drastic improvements in the performance of DSC have been made by Graetzel and coworkers at the Swiss Federal Institute of Technology (EPFL). They achieved a solar energy efficiency, η, of 7 to 12% under AM1.5 irradiation using a DSC consisting of a nanocrystalline TiO2 thin-film electrode having a nanoporous structure with large surface area, a novel Ru bipyridyl complex, and an iodine redox electrolyte [(5)]. They also developed a Ru terpyridine complex that absorbs in the near-IR region up to 900 nm as a photosensitizer for a nanocrystalline TiO_2 photoelectrode: the resulting cell obtained η = 10.4% under AM1.5 with a short-circuit photocurrent density, J_{SC}, of 20.5 $mAcm^{-2}$, an open-circuit voltage, V_{OC}, of 0.72 V, and a fill factor (*ff*) of 0.70 [(6), (7)].

The DSC is an attractive and promising device for solar cell applications that have been intensively investigated worldwide, and its PV mechanism is well understood [(8), (9)]. Recently, commercial applications of the DSC have been under intensive investigation. The cost of commercially fabricating DSCs is expected to be relatively low because the cells are made of low-cost materials and assembly is simple and easy [(10)].

1.1 Structure and Materials

The schematic structure of the DSC constructed by the Graetzel group is shown in Fig. 1. The composition of the DSC is described in this section. [(10)]

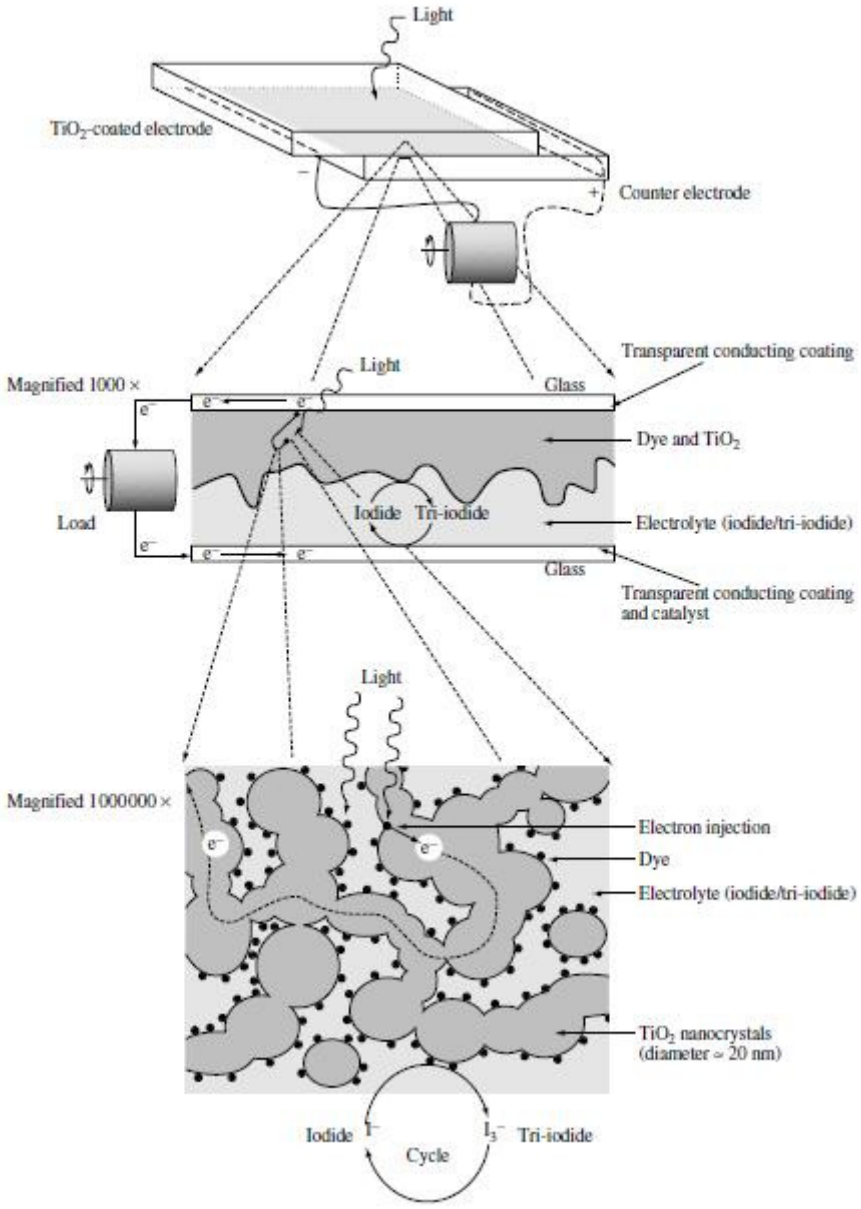

Fig. 1: Schematic structure of the DSC constructed by the Graetzel group

1.1.1 *Transparent conducting oxide-coated glass substrate*

Transparent conducting oxide (TCO)-coated glass is used as the substrate for the TiO_2 photoelectrode. For high solar cell performance, the substrate must have low sheet resistance and high transparency. In addition, sheet resistance should be nearly independent of the temperature up to 500◦C because sintering of the TiO_2 electrode is carried out at 450 to 500◦C. Indium–tin oxide (ITO) is one of the most famous TCO materials. In spite of having low resistance at room temperature, ITO resistance increases significantly at high temperature in air. Usually, fluorine-doped SnO_2 is used as the TCO substrate for DSCs (e.g. Nippon Sheet Glass Co., R = 8–10 Ω⁄square). [(10)]

1.1.2 *TiO2 photoelectrode*

Photoelectrodes made of such materials as Si, GaAs, InP, and CdS decompose under irradiation in solution owing to photocorrosion. In contrast, oxide semiconductor materials, especially TiO_2, have good chemical stability under visible irradiation in solution; additionally, they are nontoxic and inexpensive. The TiO_2 thin-film photoelectrode is prepared by a very simple process. TiO_2 colloidal solution (or paste) is coated on a TCO substrate and then sintered at 450 to 500◦C, producing a TiO_2 film about 10 μm in thickness. Because this film is composed of TiO_2 nanoparticles (10–30 nm), giving it a nanoporous structure, the actual surface area of TiO_2 compared to its apparent surface area, roughness factor (rf), is >1000; that is, a 1 cm^2 TiO_2 film (10 μm thickness) has an actual surface area of 1000 cm^2. The dye is considered to be adsorbed on the TiO_2 surface in a monolayer.

Thus, if the nanoporous TiO_2 film has a high rf, the amount of dye adsorbed is drastically increased (on the order of 10^{-7} mol cm^{-2}), resulting in an increase of LHE that is near 100% at the peak absorption wavelength of the dye. In comparison, the amount of adsorbed dyes on the surface of single-crystal and polycrystal materials is quite small, with only 1% LHE even at the peak wavelength.

Normally, the TiO_2 film contains large TiO_2 particles (250–300 nm), which can

scatter incident photons effectively, to improve the LHE as shown later. The porosity of the film is also important because the electrolyte, which contains the redox ions, must be able to penetrate the film effectively to suppress the rate-determining step via diffusion of redox ions into the film. Appropriate porosity, 50 to 70%, is controlled in the sintering process by the addition of a polymer such as polyethylene glycol (PEG) and ethyl cellulose (EC) into the TiO_2 colloidal solution or paste. Fig. 2 shows a scanning electron microscope (SEM) photograph of a typical nanocrystalline TiO2 film. [(10)]

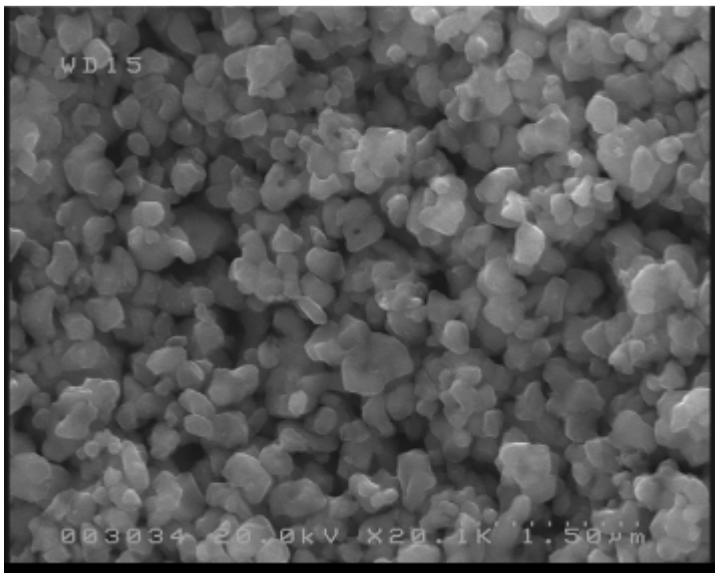

Fig. 2 SEM image of a TiO_2 layer

1.1.3 *Ru complex photosensitizer*

The Ru complex photosensitizer, which contributes the primary steps of photon absorption and the consequent electron injection, is adsorbed onto the TiO2 surface. The chemical structure of typical Ru complex photosensitizers developed by Graetzel's group are shown in Fig. 3 (TBA is tetrabutylammonium cation, $(C_4H_9)_4N^+$), and Fig. 4 shows absorption properties of the complexes in solution. The *y*-axis is represented by absorbance (A) and $1 - T$ ($= 1 - 10^{-A}$), where T is the transmittance. The *cis*-bis(4,4'-dicarboxy-2,2'-bipyridine)dithiocyanato ruthenium(II) ($RuL_2(NCS)_2$ complex), which is referred to as N3 dye (or red dye), can absorb over a wide range of the visible regions from 400 to 800 nm. The trithiocyanato 4,4'4''-

tricarboxy-2,2':6',2''-terpyridine ruthenium(II) (black dye) ($RuL'(NCS)_3$ complex), absorbs in the near-IR region up to 900 nm. Absorption by these dyes in the visible and near-IR regions is attributed to the metal-to-ligand charge-transfer (MLCT) transition. The highest occupied molecular orbital (HOMO) and the lowest unoccupied molecular orbital (LUMO) are mainly derived from the d-orbitals of the Ru metal and the π^* orbital of the ligand, respectively. The NCS ligand shifts the HOMO level negatively, leading to a red shift in the absorption property of the complex, and also contributes electron acceptance from reduced redox ions
(I^-). These Ru complexes have carboxyl groups to anchor to the TiO2 surface. Anchoring causes a large electronic interaction between the ligand and the conduction band of TiO_2, resulting in effective electron injection from the Ru complex into the TiO_2. The Ru complex is adsorbed on the TiO_2 surface via either carboxylate bidentate coordination or ester bonding ($-C(=O)O-$) as measured by FT–IR absorption analysis [(11) , (12)]. Fig. 5 shows the anchoring structure of the N3 dye adsorbed on the (101) surface of TiO_2. The coverage of the TiO_2 surface with the N3 dye reaches near 100% as derived from the surface area of TiO_2 and the amount of the dye. [(10)]

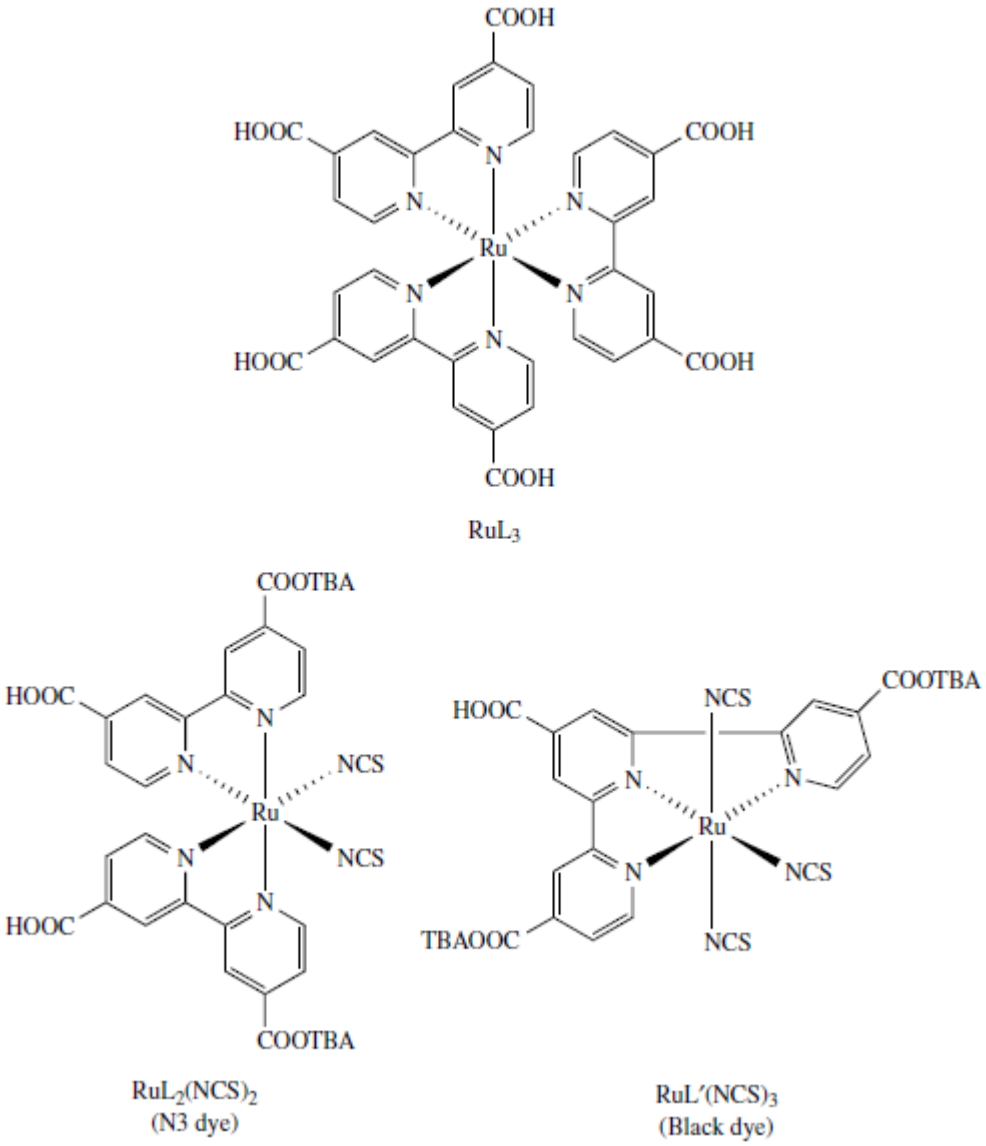

Fig. 3: Molecular structures of typical Ru complex photosensitizers

1.1.4 *Redox electrolyte*

The electrolyte used in the DSC contains I^-/I_3^- redox ions, which mediate electrons between the TiO_2 photoelectrode and the counter electrode. Mixtures of iodides such as LiI, NaI, KI, tetraalkylammonium iodide (R_4NI), and imidazolium-derivative iodides with concentrations of 0.1 to 0.5 M (M: molar concentration) and 0.05 to 0.1 M I_2 dissolved in nonprotonic solvents (e.g. acetonitrile, propionitrile, methoxyacetonitrile, propylene carbonate, and their mixture) are employed.

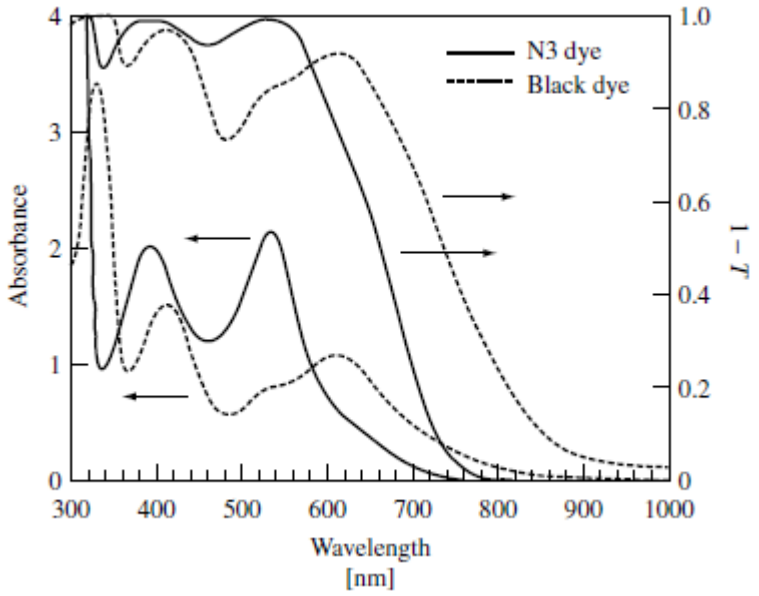

Fig. 4: Absorption spectra of N3 dye and black dye represented by absorbance and light-harvesting efficiency, 1–*T* (*T* : transmittance): (-) N3 dye, (---) black dye

Cell performance of DSCs depends on counter cations of iodides such as Li^+, Na^+, K^+, and $R_4\ N^+$ owing to different ion conductivity in the electrolyte or adsorption on the TiO_2 surface, leading to a shift of the conduction-band level of the TiO_2 electrode [(13), (14)]. Viscosity of solvents directly affects ion conductivity in the electrolyte, and consequently the cell performance. To improve cell performance, low-viscosity solvents are desired. The diffusion coefficient of I_3^- in methoxyacetonitrile is estimated as $5.4–6.2 \times 10^{-6}$ cm^2 s^{-1} [(13)]. Basic compounds such as *tert*-butylpyridine are added to the electrolyte solution to improve cell performance, as shown later [(15)]. Br^-/Br_2 and hydroquinone have also been used as redox electrolyte for DSC [(14), (16)], but the iodine redox electrolyte gives the best performance. [(10)]

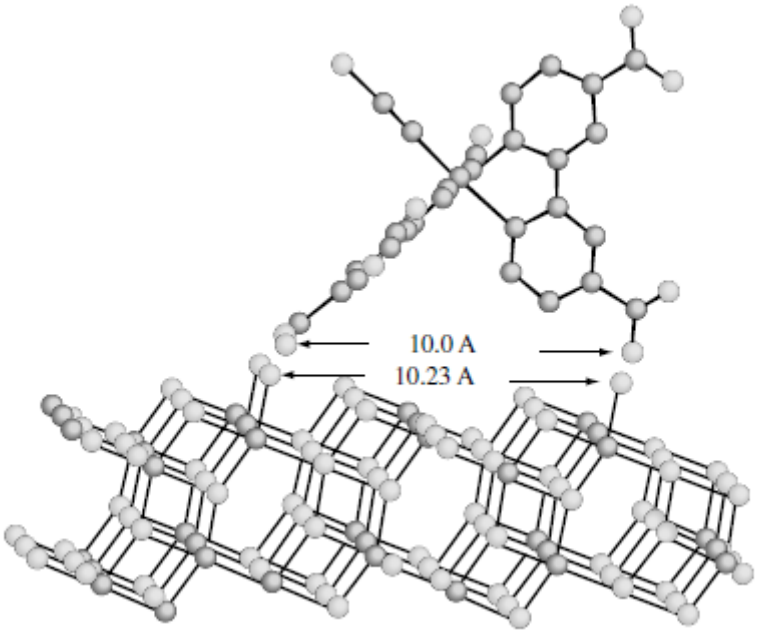

Fig. 5: Anchoring structure of N3 dye adsorbed on the (101) surface of TiO_2: the top is N3 dye and the bottom is TiO_2 [(10)]

1.1.5 *Counter electrode*

Tri-iodide ions, I_3^-, formed by the reduction of dye cations with I^- ion, are re-reduced to I^- ions at the counter electrode. To reduce the tri-iodide ions, the counter electrode must have high electrocatalytic activity. Pt coated on TCO substrate (5–10 µg cm^{-2} or approximately 200-nm thickness) or carbon are usually used as the counter electrode. [(10)]

1.1.6 *Sealing materials*

A sealing material is essential to prevent the leakage of the electrolyte, the evaporation of the solvent and to prevent the polluting of the electrolyte itself with moisture and oxygen. Chemical and photochemical stability of the sealing material against the electrolyte component, iodine, and the solvent is required and it also has to be a very good barrier towards moisture and oxygen. During the past years the greatest part of the efforts was focused on all the others DSC elements (photoelectrode, couterelectrode, electrolyte, etc.), these hard investigations leaded to a very good performance and stability of these elements. Nowadays the only element

that needs further investigations to let the device to be comparable, and then competitive, with the standard photovoltaics technology and then to permit the final industrialization of the product are the sealing procedures and materials. This is, in the author opinion, the most important goal to reach in the next future.

1.2 Mechanism

This section describes the primary processes that occur in a DSC and discusses the solar energy–to–current conversion efficiencies of cells. [(10)]

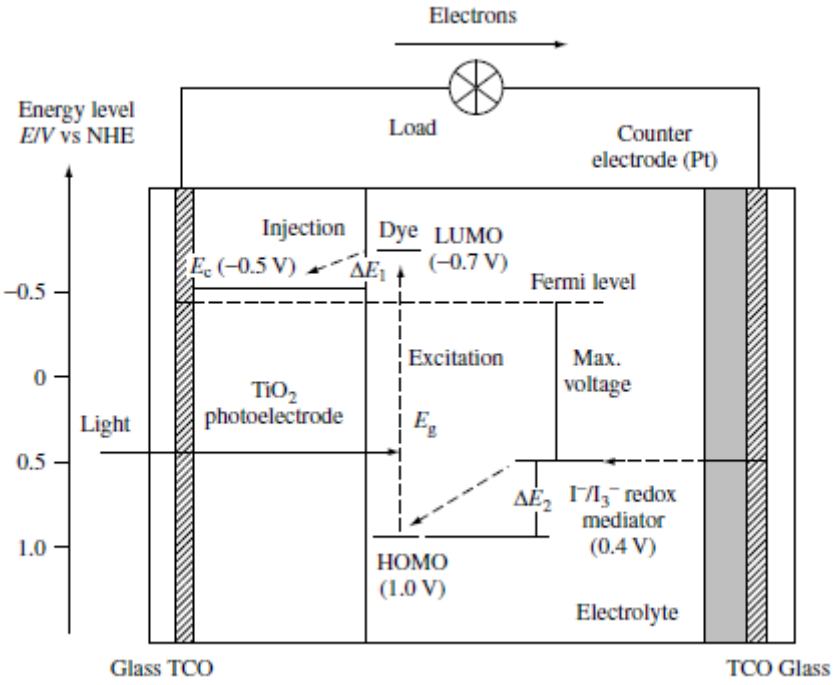

Fig. 6: Schematic energy diagram and operating principle of DSC

1.2.1 Primary processes

Fig. 6is a schematic energy diagram of a DSC. The following primary steps convert photons to current:

1. Ru complex photosensitizers adsorbed on the TiO_2 surface absorb incident photon flux.
2. The photosensitizers are excited from the ground state (S) to the excited state (S^*) owing to the MLCT transition. The excited electrons are injected into the conduction band of the TiO_2 electrode, resulting in the oxidation of the photosensitizer.

$S + h\nu \rightarrow S^*$

$S^* \rightarrow S^+ + e^- (TiO_2)$

3. Injected electrons in the conduction band of TiO_2 are transported between TiO_2 nanoparticles with diffusion toward the back contact (TCO) and consequently reach the counter electrode through the external load and wiring.

4. The oxidized photosensitizer (S^+) accepts electrons from the I^- ion redox mediator, regenerating the ground state (S), and I^- is oxidized to the oxidized state, I_3^-.

$S^+ + e^- \rightarrow S$

5. The oxidized redox mediator, I_3^-, diffuses toward the counter electrode and is rereduced to I^- ions.

$I_3^- + 2e^- \rightarrow 3I^-$

Overall, electric power is generated without permanent chemical transformation.

The performance of a DSC is predominantly based on four energy levels of the component: the excited state (approximately LUMO) and the ground state (HOMO) of the photosensitizer, the Fermi level of the TiO_2 electrode, which is located near the conduction-band level, and the redox potential of the mediator ($I^-/I3^-$) in the electrolyte.

The photocurrent obtained from a DSC is determined by the energy difference between the HOMO and the LUMO of the photosensitizer, analogous to the band gap, *E*g, for inorganic semiconductor materials. The smaller the HOMO–LUMO energy gap, the larger the photocurrent will be because of the utilization of the long-wavelength region in the solar spectrum. The energy gap between the LUMO level and the conduction-band level of TiO_2, $\Delta E1$, is important, and the energy level of the LUMO must be sufficiently negative with respect to the conduction band of TiO_2 to inject electrons effectively. In addition, substantial electronic coupling between the LUMO and the conduction band of TiO_2 also leads to effective electron injection. The HOMO level of the complex must be sufficiently more positive than the redox potential of the I^-/I_3^- redox mediator to accept electrons effectively ($\Delta E2$). The energy gaps, $\Delta E1$ and $\Delta E2$, must be larger than approximately 200 mV as driving force for each of the electron-transfer reactions to take place with optimal efficiency [(17)].

In the case of solid–liquid junction solar cells, PSCs, the voltage is attributed to the energy gap between the Fermi level (near conduction-band level for *n*-type semiconductor) of the semiconductor electrode and the redox potential of the mediator in the electrolyte.

As shown in Fig. 6, the voltage in the DSC is developed by the energy gap between the Fermi level of a TiO_2 electrode and the redox potential of the I^-/I_3^- in the electrolyte.

The conduction-band level of the TiO_2 electrode and the redox potential of I^-/I_3^- were

estimated to be −0.5 V versus normal hydrogen electrode (NHE) and 0.4 V versus NHE, respectively, as shown in Fig. 6 [(9)] (or −0.7 V versus saturated calomel electrode (SCE) and 0.2 V versus SCE, respectively [(18), (17)]. Thus, in the case of a DSC using a TiO_2 electrode and I^-/I_3^- redox mediator, the maximum voltage is expected to be approximately 0.9 V, depending on the electrolyte component because the Fermi level of the TiO_2 electrode depends on the electrolyte components and their concentrations.

In contrast to a conventional *p*-*n*-type solar cell, the mechanism of a DSC does not involve a charge-recombination process between electrons and holes because electrons are only injected from the photosensitizer into the semiconductor and a hole is not formed in the valence band of the semiconductor. In addition, charge transport takes place in the TiO_2 film, which is separated from the photon absorption site (i.e. the photosensitizer); thus, effective charge separation is expected. This photon-to-current conversion mechanism in a DSC is similar to the mechanism for hotosynthesis in nature, in which chlorophyll functions as the photosensitizer and charge transport occurs in the membrane.

In conventional *p*-*n*-type solar cells and classical PSCs using polycrystal or singlecrystal photoelectrodes, electronic contact between the components that form the photovoltaically active junction, and the equilibrium between the electronic charge carriers in them, leads to space charge formation. Photogenerated charges are separated by the electric field in the space charge layer. In DSC, however, the individual particle size is too small to form a space charge layer. Charge separation in DSC has been discussed relative to an electrical field at the electrolyte/semiconductor interface, although not one due to space charge in the semiconductor [(19)]. Small cations, such as Li+, in the electrolyte and H^+ released from the dyes upon binding, can adsorb (or intercalate) on the semiconductor surface. A dipole is formed across the Helmholtz layer between these cations and negatively charged species (iodide ions and the dye). The electrical potential drop across the Helmholtz layer will help separate the charges and reduce recombination with the dye cations or the redox mediator. Under illumination, this potential will decrease, as the electrons injected in the semiconductor will neutralize some of the positive charge at the surface. [(10)]

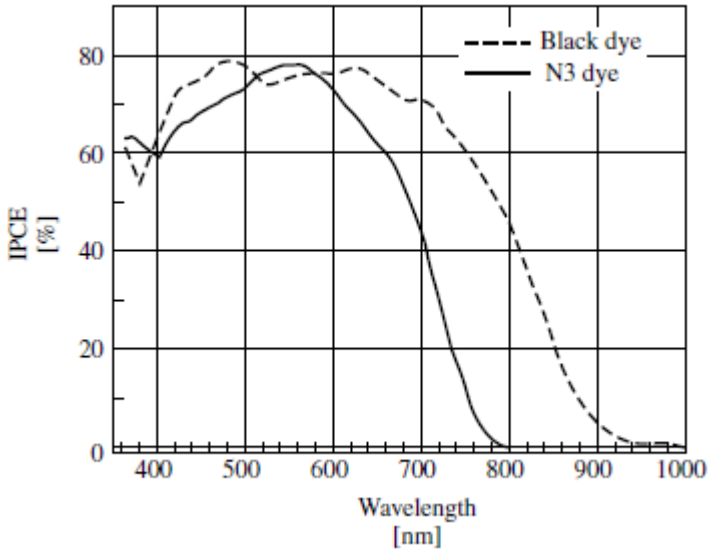

Fig. 7: Spectral response curve of the photocurrent for the DSSC sensitized by N3 and black dyes: (-) N3 dye, (---) black dye. The incident photon-to-current conversion efficiency (IPCE) is plotted as a function of wavelength. The data is used from Reference [(9)]

1.2.2 *Photovoltaic performance*

Fig. 7 shows the external spectral response curve of the photocurrent for nanocrystalline TiO_2 solar cells sensitized by N3 and black dyes with an I^-/I_3^- redox electrolyte, where the incident photon-to-current conversion efficiency (IPCE) is represented as a function of wavelength. IPCE is obtained by the following equation:

$$\mathrm{IPCE}[\%] = \frac{1240[\mathrm{eV}\cdot\mathrm{nm}] \times J_{SC}[\mu\mathrm{A\,cm^{-2}}]}{\lambda[\mathrm{nm}] \times \Phi[\mu\mathrm{W\,cm^{-2}}]} \times 100$$

where J_{SC} is the short-circuit photocurrent density for monochromatic irradiation, λ is the wavelength, and Φ is the monochromatic light intensity. As shown in Fig. 7, solar cells sensitized by the Ru complex photosensitizers can efficiently convert visible light to current. N3 dye ($RuL_2(NCS)_2$) responds to light from 400 to 800 nm, and black dye ($RuL'(NCS)_3$) responds to the near-IR region up to 950 nm. The IPCE of the N3 dyesensitized solar cell reaches 80% at 550 nm and exceeds 70% in the region from 400 to 650 nm. Taking into consideration losses due to light reflection and absorption by the TCO substrate, the internal photon-to-current conversion efficiency is effectively 90 to 100%, indicating high performance of the DSC. IPCE is also given by the following equation:

$\mathrm{IPCE} = \mathrm{LHE}\ \varphi_{inj}\eta_c$

$\mathrm{LHE} = 1 - T = 1 - 10^{-A}$

where LHE is the light-harvesting efficiency, φinj is the quantum yield of electron injection, and ηc is the efficiency of collecting the injected electrons at the back contact. According to equation above reported, if φ_{inj} and η_c are almost equal to unity, IPCE is determined by the LHE (i.e. $1 - T$) of the dye adsorbed on the film (shown in Fig. 4).

Solar energy–to–electricity conversion efficiency, η, under white light irradiation (e.g. AM1.5) can be obtained by the following equation:

$$\eta = J_{SC} \times V_{OC} \times ff / I_0 \times 100$$

where I_0 is the photon flux (approximately 100 $mWcm^{-2}$ for AM1.5). A current versus voltage curve obtained for a nanocrystalline TiO_2 solar cell sensitized by black dye is shown in Fig. 8 [(9)]. As an example is reported the Evaluation of the performance that was carried out at the National Renewable Energy Laboratory (NREL) operated by the US Department of Energy. An efficiency of 10.4% was obtained (cell size = 0.186 cm2, J_{SC} = 20.53 $mAcm^{-2}$, V_{OC} = 0.721 V, and ff = 0.704) [(7), (9), (10)]

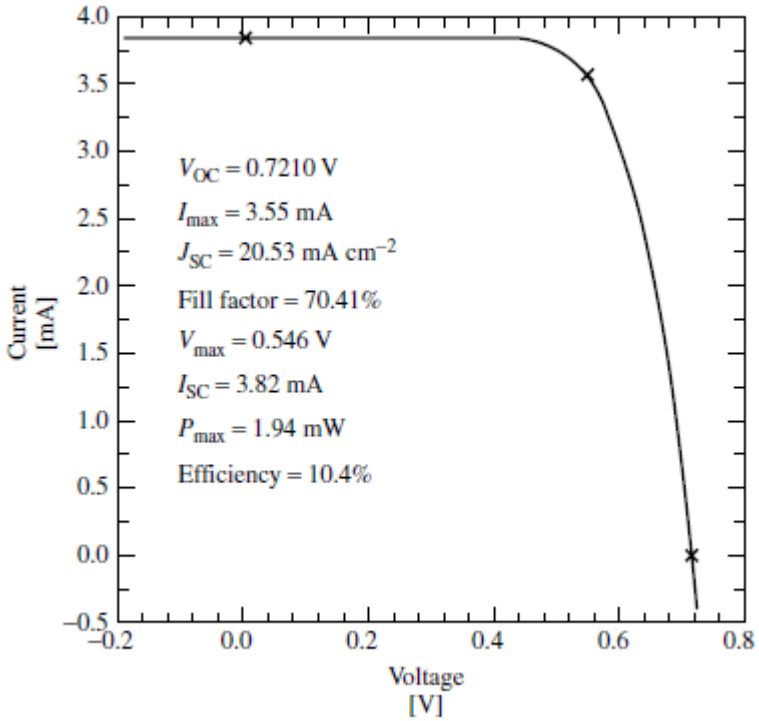

Fig. 8: Photocurrent–voltage curve obtained for a nanocrystalline TiO_2 solar cell sensitized by black dye. The certified results were obtained at NREL (USA). [(9)]

1.3 Charge-transfer Kinetics

1.3.1 Electron injection process

Recently, the electron-transfer kinetics in the DSC, shown as a schematic diagram in Fig. 9, have been under intensive investigation. Time-resolved laser spectroscopy measurements are used to study one of the most important primary processes, electron injection from photosensitizers into the conduction band of semiconductors [(20), (21)].

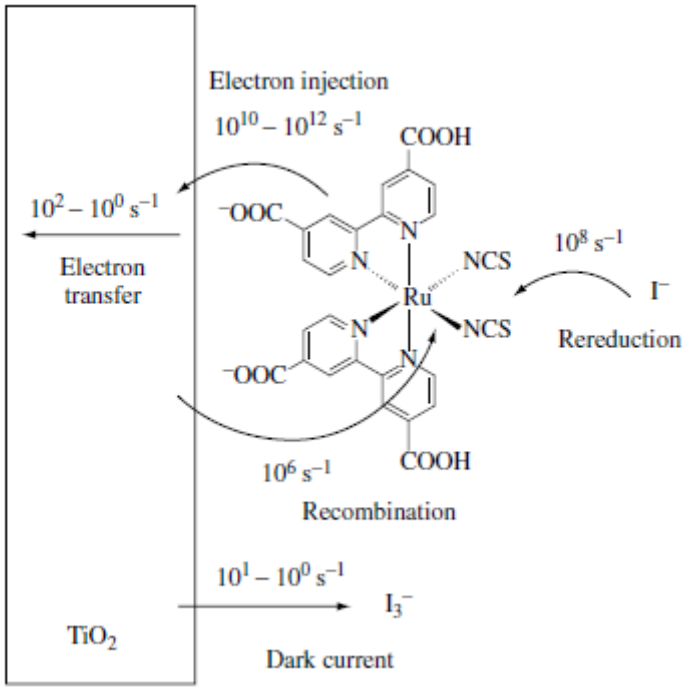

Fig. 9: Schematic diagram of electron-transfer processes in DSC

The electron-transfer rate from the photosensitizer into the semiconductor depends largely on the configuration of the adsorbed photosensitizer material on the semiconductor surface and the energy gap between the LUMO level of the photosensitizer and the conduction-band level of the semiconductor. For example, the rate constant for electron injection, k_{inj}, is given by Fermi's golden rule expression

$$k_{inj} = \left(\frac{4\pi^2}{h}\right)|V|^2\rho(E)$$

where V is the electronic coupling between the photosensitizer and the semiconductor, $\rho(E)$ is the density-of-states of the conduction band, and h is the Planck constant. The

value of V is attributed to overlap between the wavefunction of the excited states of the photosensitizer and the conduction band, and it depends largely on the distance between the adsorbed photosensitizer material and the semiconductor surface. In a DSC, the photosensitizer is strongly adsorbed on the semiconductor surface with carboxyl groups as the anchor, resulting in a very large V between the π^* orbital of the excited state of the photosensitizer and the conduction band of TiO_2, which consists of the unoccupied 3d orbital of Ti^{4+}. In addition, the conduction band of the semiconductor has a continuous and relatively large density-of-states. Thus, electron injection from the photosensitizer to the semiconductor occurs at a higher rate than does the relaxation from the excited state to the ground state (i.e. relaxation via the emission lifetime). For example, it has been observed that electron injection from N3 dye into TiO_2 occurs on the order of femtoseconds as measured by the time-resolved laser spectroscopy [(20), (22)]. This ultrafast rate of electron injection contributes to the high energy-conversion efficiencies of the DSC.

In addition, the rate constant for electron injection depends largely on the semiconductor materials employed. A slower electron injection rate was observed with coumarin dyes and N3 dye injected into ZnO compared to the TiO_2 system [(23), (24), (25)]. The different rate constant may be caused by the difference in the electronic coupling between the π^* orbital of the dye and the accepting orbitals in ZnO and TiO_2 and/or their densityof-states. The states near the conduction-band edge of ZnO consist of the 4s orbitals of Zn^{2+}, while those of TiO_2 consist of the 3d orbitals of Ti^{4+}, which may result in the observed difference in their electronic coupling with the π^* orbital of the dye. [(10)]

1.3.2 *Charge recombination*

The charge-recombination process (Fig. 9) between injected electrons and oxidized dyes must be much slower than electron injection and electron transfer from I^- ion into oxidized dyes (i.e. regeneration of dyes) to accomplish effective charge separation. It was reported that charge recombination between injected electrons on TiO_2 and cations of N3 dye occurs on the order of microseconds to milliseconds, in contrast with ultrafast electron injection [(20), (26), (27), (28), (29)]. The much slower charge

recombination compared to electron injection leads to effective charge separation and consequently high cell performance.

Charge recombination in the N3 dye/TiO_2 system is derived from electron transfer from TiO_2 to Ru(III), while electron injection occurs because of electron transfer from the bipyridyl ligand to TiO_2. Thus, it is considered that long-distance electron transfer from TiO_2 to the Ru metal center leads to a much smaller electron-transfer rate. [(10)]

1.3.3 *Regeneration of the oxidized photosensitizers*

Electron transfer from the I^- ion into oxidized photosensitizers (cations), or regeneration of photosensitizers (Fig. 9), is one of the primary processes needed to achieve effective charge separation. The kinetics of this reaction has also been investigated by time-resolved laser spectroscopy [(28) , (30)]. The electron-transfer rate from the I^- ion into cations of the N3 dye was estimated to be 100 ns [(28)]. This reaction rate is much faster than that for charge recombination between injected electrons and dye cations. Thus, fast regeneration of the oxidized photosensitizer also contributes to the accomplishment of effective charge separation. [(10)]

1.3.4 *Recombination between injected electrons and tri-iodide ions (dark current)*

Recombination of injected electrons with tri-iodide ions (I_3^-) on a semiconductor as shown in Fig. 9, corresponding to dark current, is one of the primary processes in a DSC (reaction [a]).

$I_3^- + 2e^-(TiO2) \rightarrow 3I^-$ [a]

This reaction can also occur on the SnO2 surface because the nanocrystalline TiO_2 does not completely cover the TCO substrate, but predominantly occurs on the TiO_2 surface because of the high surface area of the TiO_2 relative to the SnO_2. This reaction contributes to the loss of PV performance in a DSC analogous to the forward-bias injection of holes and electrons in a *p-n* junction. The V_{OC} in DSC is obtained using the injection current, I_{inj}, as represented by the following equation, as well as *p-n* junction solar cells:

$$V_{OC} = \frac{kT}{q} \ln\left(\frac{I_{inj}}{I_0} + 1\right) \quad [b]$$

where k is the Boltzmann constant, q is the magnitude of the electron charge, T is the absolute temperature, and I_0 is the dark current. I_{inj} and I_0 are represented by the following equations:

$I_{inj} = q\eta\Phi_0$ [c]

$I_0 = q\, n_0 k_{et}[I_3^-]$ [d]

where η is the quantum yield for photogenerated electrons, Φ_0 is the incident photon flux, n_0 is the electron density on the conduction band of the semiconductor in the dark, k_{et} is the rate constant for recombination, reaction [a], and $[I_3^-]$ is the concentration of oxidized redox mediator, I_3^-, in the solution. From equations [b] to [d], we obtain the following equation:

$$V_{OC} = \frac{kT}{q} \ln\left(\frac{\eta\Phi_0}{n_0 k_{et}[I_3^-]} + 1\right) \quad [e]$$

Usually, $\eta\Phi_0 >> n_0 k_{et}[I_3^-]$ and equation [e] is simplified as follows [(15), (18), (31), (32)]:

$$V_{OC} = \frac{kT}{q} \ln\left(\frac{\eta\Phi_0}{n_0 k_{et}[I_3^-]}\right) \quad [f]$$

Dark current is considered to occur at the TiO_2/electrolyte interface where the photosensitizers are not adsorbed. To suppress dark current, pyridine derivatives such as *tert*-butylpyridine (TBP) have been employed as coadsorbates on the TiO_2 surface, resulting in the improvement of photovoltage [(15), (31)]. TBP is considered to adsorb on the uncovered TiO_2 surface.

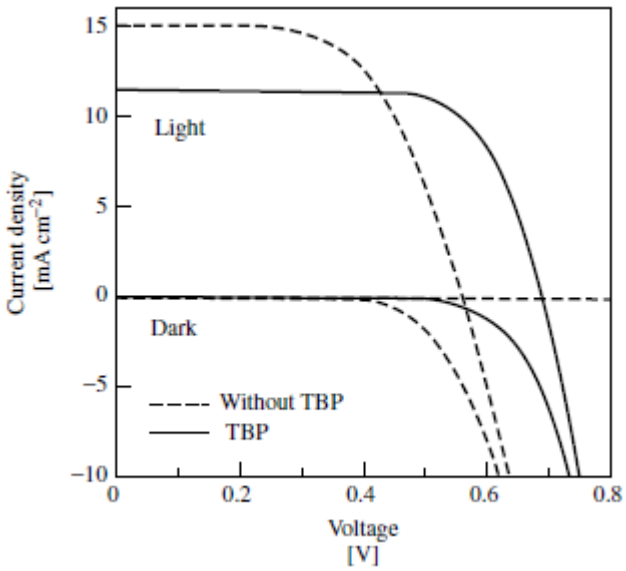

Fig. 10: Current–voltage characteristics of N3 dye-sensitized TiO_2 solar cells under illumination and darkness using electrolyte with and without TBP: (-) without TBP, (---) with TBP

Fig. 10 shows the current–voltage characteristics of the N3 dye-sensitized TiO_2 solar cell under illumination and darkness, using electrolyte with and without TBP. This clearly indicates that TBP suppresses dark current, resulting in the improvement of V_{OC}. A decrease of the J_{SC} by addition of TBP is considered to be due to the negative shift of the conduction-band level of TiO_2 owing to adsorption of TBP, which has basic property, leading to suppression of the electron injection from the dye. The kinetics of recombination, reaction [a], has been investigated and discussed [(15), (31), (33), (34)]. If this reaction occurs predominantly with a large reaction rate, the DSC does not work. Taking into consideration this and the slow transport of the photoinjected electrons through the nanocrystalline TiO_2 film (described in the next section), the recombination must be extremely slow. In fact, the rate of recombination has been estimated to be on the order of 0.1 s to several seconds [(35)]. This slow recombination would be due to a low electrocatalytic activity of TiO_2 for the reduction of tri-iodide ions. [(10)]

1.3.5 *Electron transport in TiO2 film*

Electron transport in TiO_2 film is an important process related to PV performance in the DSC (see Fig. 9) and has been studied by many researchers [(36), (37)]. The electron transport in nanocrystalline TiO_2 film has been discussed with respect to different mechanisms: a diffusion model [(36), (38)], a mechanism that involves

tunneling through potential barriers between the particles [(38)], a trapping/detrapping mechanism [(39), (40)], and an insulator–metal (Mott) transition mechanism [(41)]. Electron conductivity in TiO_2 is very small, resulting in slow response of the photocurrent. For example, diffusion coefficients of the electrons in nanocrystalline TiO_2 film have been estimated to be 1×10^{-7} [(36)] and 1.5×10^{-5} $cm^2\ s^{-1}$ [(42)]. In the DSC, the electron conductivity of TiO_2 film is significantly increased due to electron injection from photosensitizers under photon irradiation [(43), (38)]. In addition, conductivity and response of the photocurrent increase with increasing incident light intensity [(43), (38)]. It has been suggested that when injected electrons fill the trap site and/or surface levels in the TiO_2 film, the diffusion coefficient of the electron increases drastically, leading to elevated electron conductivity and good response of the photocurrent. [(10)]

1.4 Characteristics

As described above, the photovoltaic (PV) mechanism of DSC is different from that of conventional *p*-*n*-type solar cells. The DSC has other unique characteristics such as the following:

1. *High energy conversion efficiency*: A DSSC efficiency equal to that of the amorphous-

Si solar cell has been obtained during laboratory development and efficiencies greater than 10% are now reality.

2. *Low-cost fabrication*: The DSC is very simple to construct and is made of low-cost materials. Fabrication costs will therefore be less than that for conventional solar cells. For example, US$0.60/W, which may be competitive for conventional solar cells, has been estimated for a DSC with 10% efficiency [(44), (45)].

3. *Abundant supply of component materials*: Oxide semiconductors such as TiO_2, dye, and iodine are abundantly available. Although metal deposits of Ru are limited, the amount of Ru complex used in the DSSC is only 1×10^{-7} mol cm^{-2}. Anyway organic dye photosensitizers could be used rather than Ru complexes if resource limitation is a problem.

4. *Good potential for colorful, adaptable consumer products*: Colorful and transparent solar cells can be made using various kinds of dyes, depending on the use of the cell. For example, transparent solar cells could be used in place of windowpanes. Additionally, the use of a plastic substrate, rather than glass, is possible if low temperature processing of the TiO_2 film preparation (<250◦C) is available and would expand the use of DSC.

5. *Low potential for environmental pollution*: The TiO_2, dyes, and iodine used in the DSC are nontoxic. The only component that could potentially cause harm is the organic solvents used in the electrolyte solution. Future research should be directed toward developing a solid-state electrolyte.

6. *Good recyclability*: The organic dye photosensitizers adsorbed on the electrode can be removed by washing the electrode with alkali solutions or combustion, providing recyclability of the DSC.[(10)]

2. Physics of the dye solar cell

In this chapter, the physics are summarized, which are required for an understanding of the dye solar cell (DSC). In section 2.1 the structure and working principle of the dye solar cell is introduced.

The DSC is an electrochemical solar cell, in particular it utilizes a liquid electrolyte, but in recent years there has been a strong push towards the use of gel electrolytes.

Therefore, the interface between a metal (or semiconductor) and an electrolyte must be very well understood in order familiarize oneself with the processes in a DSC. The central quantity here is the electrochemical potential, which is a general concept, that can be applied to liquid electrolytes, as well as solid state bodies. It is introduced in section 2.2.

Mass transport in an electrochemical system occurs down the gradient of the electrochemical potential. In a redox electrolyte, however, the dominant form of mass transport is diffusion, i.e. the field driven current (migration) can be neglected. This is discussed in section 2.3.

The interface between a solid-state electrode and a liquid electrolyte is further addressed in 2.4 and 2.5. In particular, the charge transfer over such an interface is of importance.

And finally, in section 2.6 the I-V curve of a DSC (and a solar cell in general) is discussed. Important electrical parameters of solar cells are introduced and a model for the I-V curve is presented.

2.1 The architecture of the dye solar cell

The architecture of a dye solar cell (DSC) is shown in Fig. 11. The DSC consists of a dye-covered, nanoporous TiO_2 (titanium dioxide) layer and an electrolyte encapsulated between two glass plates.

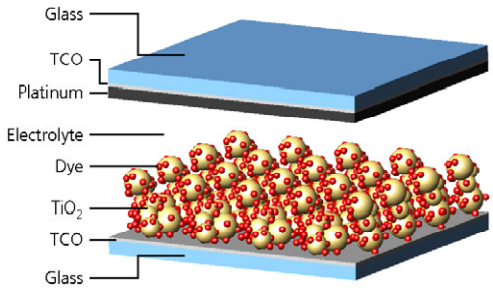

Fig. 11: Architecture of a dye solar cell.

Front and counter substrates are coated with a transparent conducting oxide (TCO). Fluorine doped tin oxide (SnO2:F), FTO is most commonly used. The FTO at the counter electrode is coated with few atomic layers of platinum (Pt), in order to catalyze the redox reaction with the electrolyte.

The front electrode is coated with a nanocrystalline TiO_2 layer with average particle sizes of 10 nm, 25 nm and 250 nm depending on whether you want to obtain respectively a transparent, opaque or scattering film. Assuming a layer thickness of 10 μm, the resulting effective surface is about 1000 times larger as compared to a dense, compact TiO2 layer. Three modification of TiO_2 exist: rutile, anatase and brookit. In the DSC preferably only the anatase modification is used.

On the surface of the TiO2, a monolayer of dye molecules is adsorbed. The huge nanoporous surface allows for an adsorption of a sufficiently large number of dye molecules for efficient light harvesting. During the last years and also today the most efficient and commonly employed dye molecule in DSC is a ruthenium (Ru) metal-organic complex. Anyway in the recent past other complex both metal-organic (Cyclic tetrapyrrole based molecule (46)) and completely organic (i.e. indulines (47) and polynes) have been studied with good results. The spectral absorption of the ruthenium dyes lies more or less between 300 nm and 800 nm but this range can be very different depending on the type of dyes used. The chemical structure of the most widespread dye molecule in DSC, the so called N719 [(48)] is shown in Fig. 12a.

Good adsorption of the dye to the TiO_2 is important and is achieved over the two carboxylic groups of the ligand (L=2,2'-bipyridyl-4,4'-dicarboxylic acid) of the RuL2(NCS)2

Between the two glass substrates, a liquid redox electrolyte is encapsulated. In particular, the liquid electrolyte is able to penetrate the nanopores of the TiO_2. The redox couple iodide/triiodide (I^-/I_3^-) is commonly used. Iodide is usually applied as a room temperature molten salt (ionic liquid), e.g. an imidazolium iodide (Fig. 12b). The ionic iodide liquid acts as a solvent for iodine (I_2), which reacts with iodide to form triiodide (I_3^-):

$I_2 + I^- \rightarrow I_3^-$

During cell operation the following redox reaction takes place:

$I_3^- + 2e \leftrightarrow 3\ I^-$

In general, best efficiencies are obtained upon illumination from the TiO2 side.

However, the DSC is usually semi-transparent and may be illuminated from the counter electrode side as well.

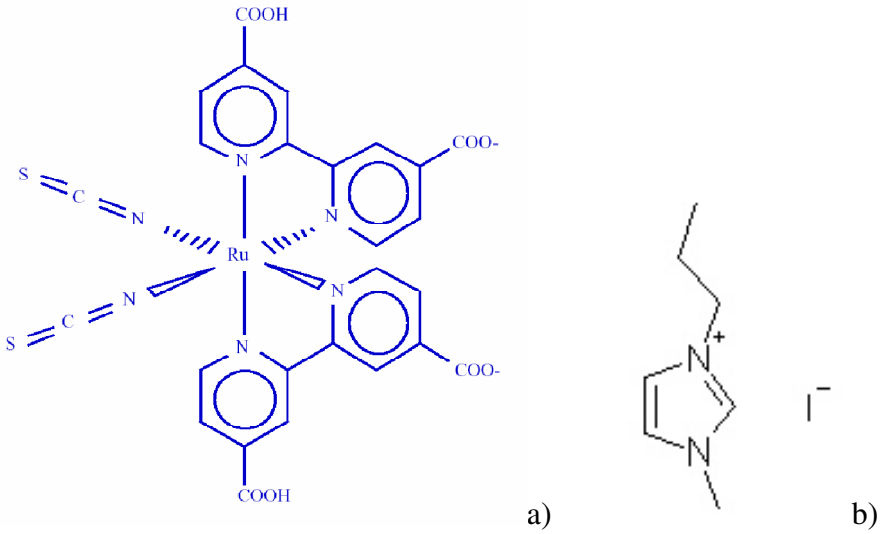

Fig. 12: a) Chemical structure of the N719 b) Chemical structure of propyl-methyl-immidazolium iodide (PMII)

2.1.1 *Energy diagram and working principle of a dye solar cell*

The energy diagram and electron transfer paths of a DSC are shown in Fig. 13. The working principle of a DSC is based on the kinetics of the shown electron transfer reactions. Electrons are injected from the dye into the TiO_2 and the hole is injected into the electrolyte. Therefore, charge separation and charge transport occurs in different media and is spatially separated.

By absorption of a photon, the dye molecule is excited. An electron is excited from the highest occupied molecular orbital (HOMO) to the lowest unoccupied molecular orbital (LUMO). The excited electron is rapidly injected into the conduction band of the TiO2.

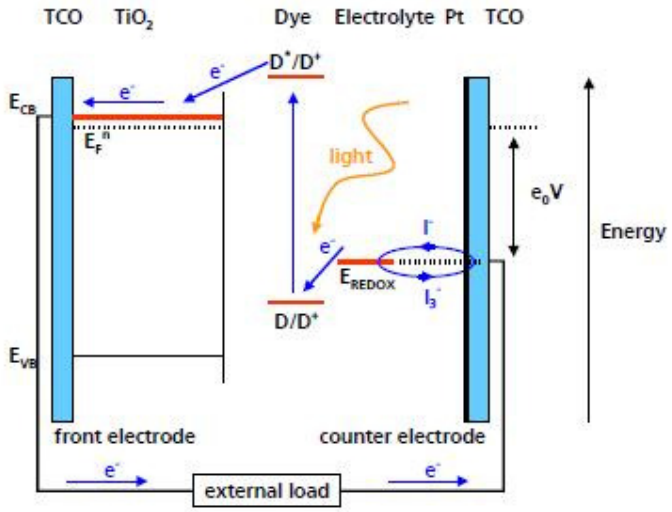

Fig. 13: Energy scheme and electron transfer paths of a dye solar cell

Charge transport occurs in the conduction band of the TiO_2 by pure diffusion of electrons to the FTO electrode. Electric fields in the TiO_2 are screened by the cations in the electrolyte, which penetrates the pores of the TiO_2 on a nano-scale [(49)]. Upon reaching the TCO electrode, the electrons are conducted to the counter electrode via the external circuit. Catalyzed by the platinum on the counter electrode, the electrons are accepted by the electrolyte. This means, that the holes in the electrolyte (the I_3^-) recombine with electrons to form the negative charge carriers,

$I_3^- + 2e^- \rightarrow 3\ I^-$ eq1

By diffusion, the negative charge (I^-) is transported back and reduces the oxidized dye

molecule (D^+). Triiodide (I_3^-) is formed and the electrical circuit is completed:

$2\ D^+ + 3\ I^- \rightarrow I_3^- + 2\ D$ eq2

From Fig. 13 it is clear, that the negative pole of the DSC is at the TiO_2 coated TCO substrate and the positive pole is at the platinum-coated TCO substrate.

It should be noted, that TiO_2 is a semi conductor with a large band gap of 3.2 eV, corresponding to a wavelength of λ=390 nm. Accordingly, visible light is not absorbed by the TiO_2. Direct absorption by UV-light is unwanted, since the created holes in the valence band of the TiO_2 are highly reactive and produce side reactions in the electrolyte, which are destructive for the cell in long term operation (50).

2.1.2 *Recombination losses in a dye solar cell*

Apart from these *current-producing* processes, *loss* processes occur in the DSC. An excited dye molecule may directly relax into its ground state, without injection of an electron into the TiO_2. This process is negligible, as injection is about 1000 times faster [(48)].

Also, electrons from the conduction band of the TiO2 may recombine with the oxidized dye molecule, before the dye is reduced by the electrolyte. However, reduction by the electrolyte is about 100 times faster [(18)].

The most significant loss mechanism in the DSC is the recombination of TiO2 conduction band electrons with the holes in the electrolyte, i.e. I_3^-. The electron tran sport by diffusion in the TiO2, and their recombination with the electrolyte are the two competing processes in the DSC [(51)].

It is important to realize, that for this reason the triiodide concentration in a DSC must be small. On the other hand, the triiodide concentration must be high enough as to provide enough recombination partners for the electrons at the platinum counter electrode. If this is not the case, the maximum current of the DSC will be *diffusion-limited*, i.e. limited by the diffusion of triiodide.

Additionally, it should be noted, that the electrolyte penetrates the TiO_2 and is also in contact with the front FTO electrode. If the charge transfer resistance at the front FTO electrode would be the same as at the counter electrode, the DSC would indeed not operate properly. However, the charge transfer resistance at the counter electrode is reduced by many orders of magnitude by the platinum catalyst. Whereas the charge

transfer resistance between pure, uncoated FTO and the iodide/triiodide redox couple is sufficiently high. This cannot be taken for granted, especially with redox couples other than iodide/triiodide.

As optional layer in the architecture of a DSC, a very thin (<100 nm), dense TiO_2 layer may applied *beneath* the TiO_2. This layer is aimed to further suppress charge transfer from the front FTO to the electrolyte [(52)].

Additionally, an optional light scattering layer may be applied *on top* of the TiO_2 in order to increase light harvesting [(53)]. Thus, transmitted light will be reflected back into the TiO_2 layer. This layer must be an insulator and porous, i.e. penetrable by the electrolyte. Such a scattering layer (e.g. ZrO_2) leads to an opaque (not transparent) DSC.

2.2 Electrochemical potential

An essential concept in understanding the DSC is the *electrochemical potential*. In this section, it will be shown, that the electrochemical potential is a general concept, which is equivalent to the fermi energy of a metal or semiconductor and the redox energy of a redox electrolyte. Such a general concept is needed in the DSC, since charge transfer occurs between different media (semiconductor, metal, redox electrolyte).

The electrochemical potential η is the sum of the chemical potential μ and the electrical potential ϕ [(54)]:

$$\eta = \mu + ze_0\phi \quad \text{eq3}$$

Here, e_0 is the elementary charge and z the number of charges of the considered species. It should be noted, that the electrical potential has the dimension of a voltage. It is given by the macroscopic distribution of charges.

The chemical potential μ of a species is determined by its concentration c:

$$\mu = \mu_0 + k_B T \ln \frac{c}{c_{st}} \quad \text{eq4}$$

Here, μ_0 is determined by the surroundings, k_B is the Boltzmann constant, T the temperature and c_{st} the standard concentration. Obviously, μ_0 is the value of the chemical potential, if the considered species is present under standard concentration $c=c_{st}$.

The electrochemical potential corresponds to the energy, which is required to bring a particle of the considered species from the inside of the interacting system to the interaction-free point of infinity (vacuum level). This definition is equivalent to the definition of the fermi energy EF or the work function of a metal or semiconductor. Therefore, the electrochemical potential and the fermi energy are equivalent [(54)]:

$$\mu = E_F \quad \text{eq5}$$

From semiconductor physics it is known, that the quasi-fermi energy of electrons E_F^n in the conduction band of a semiconductor is given by [(55)]:

$$E_F^n = E_{CB} + k_B T ln \frac{n}{N_C} \quad \text{eq6}$$

Here E_{CB} is the energy level of the conduction band, n is the density of electrons in the conduction band and N_C is density of states in the conduction band. The analogy with eq3 and eq4 is immediately obvious.

The same analogy applies for a redox electrolyte. According to the general redox

$$v_{Ox}Ox + me^- \leftrightarrow v_{RED}Red \quad \text{eq7}$$

a redox electrolyte is able to accept or release electrons. Here, Ox is the oxidized species and Red the reduced species. ν are the stoichiometric coefficient and m the number of transferred electrons.

The redox energy is the energy which is required to remove an electron from the redox electrolyte, similar to the fermi energy of a metal. Therefore, the redox energy of a redox electrolyte E_{Redox} is equivalent to the electrochemical potential of an electron in the electrolyte [(56)]:

$$\eta = E_{Redox} \quad \text{eq8}$$

The Nernst equation allows to calculate the redox potential from the concentrations c of the redox species [(57)]:

$$\eta = E_{Redox} = E^0_{Redox} + \frac{K_B T}{m} \ln\left(\frac{c_{Ox}^{\nu Ox}(c^{st})^{\nu Red}}{c_{Red}^{\nu Red}(c^{st})^{\nu Ox}}\right) \quad \text{eq9}$$

With E^0_{Red} the standard redox potential and c_{st} the standard redox concentration.

2.3 Mass transport in an electrochemical system

In general, in electrochemical systems, it is necessary to consider two modes of mass transport. Mass transport occurs due to [(58)]

- a gradient in the electrochemical potential and convection
- *Convection*

is the movement of a species due to mechanical forces. However, convection is not an important form of mass transport in this work, since the electrolyte layers in a DSC are very thin (<50 µm). In such thin layers, diffusion dominates and no convection regions are formed in the DSC [(59)].

2.3.1 Gradient in the electrochemical potential

In a system, which consists of many subsystems, between which mass and charge transport is possible, a constant electrochemical potential throughout the system defines the *equilibrium* state. In equilibrium no net charge or mass transport occurs. On the other hand, if the electrochemical potential is not equal throughout the system, mass transport will occur in order to compensate all electrochemical potential differences.

The electron current density *j* is determined by the gradient in the electrochemical potential [(54)]:

$$\vec{j} = \frac{\sigma}{e_0}\vec{\nabla}\eta \quad \text{eq10}$$

Here, σ depicts the conductivity of the species. It is given by [(54)]:

$$\sigma = bc\, e_0 \quad \text{eq11}$$

With *b*, the mobility of the species, which already includes the number of charges *z*. According to eq3 and eq10, the current is determined by the sum of the field driven current (migration) and diffusion.

Migration, i.e. the field driven current, is the movement of charged species due to an electrical potential gradient, and it is usually the origin of mass and charge transport through the electrolyte. The current of electrons through the external circuit must be

balanced by the passage of ions through the solution between the electrodes. It is, however, *not* necessarily an important mechanism of mass transport for the redox active species even if it is charged. The forces leading to the field driven current (migration) are purely electrostatic, and hence the charge can be carried by any ionic species in the solution [(58)]. As a result, if a large excess of inert (redox inactive) electrolyte is in the solution, this balances the charge, and little redox active species is transported by migration. The inert electrolyte in a DSC is the cation of the iodide salt, usually Li^+ or an imidazolium$^+$ ion. These inert charges screen the inside of the electrolyte from electrostatic forces by the formation of a Helmholtz double layer at the electrodes (this will be explained in section 2.4.1). It should be noted, that in the electrolyte of a DSC the reduced *and* the oxidized redox species are negatively charged. In case of the hole (I_3^-) migration would therefore work against the intended direction of mass transport.

Diffusion is the movement of a species down a concentration gradient, and it must occur whenever there is a chemical change at a surface. In a redox electrolyte, especially in the DSC, diffusion is the dominant form of mass transport.

2.3.2 *Fick's diffusion laws*

For the case, that the gradient in the electrical potential can be neglected, mass transport will only occur by diffusion. Convection is not an important form of mass transport in this work, since the electrolyte layers are very thin (<50 µm).

According to eq3, eq4 and eq10, the current is therefore:

$$\vec{j} = \frac{\sigma}{e_0}\vec{\nabla}\left(\mu_0 + k_B T \ln\frac{c}{c_{st}}\right) \quad \text{eq12}$$

$$\vec{j} = \frac{\sigma}{e_0} k_B T \frac{1}{C}\vec{\nabla}C \quad \text{eq13}$$

$$\vec{j} = b k_B T \vec{\nabla}C \quad \text{eq14}$$

With the Einstein relation and the diffusion coefficient *D*,

$$D = \frac{k_B T}{e_0} b \qquad \text{eq15}$$

this leads to the well-known *1st Fick's Law* for electrons:

$$\vec{j} = e_0 D \vec{\nabla} C \qquad \text{eq16}$$

With the continuity equation $\frac{\delta n}{\delta t} = div \frac{j}{e_0}$ the *2nd Fick's Law* is obtained (here: in one dimension):

$$\frac{\delta c}{\delta t} = D \frac{\delta^2 C}{\delta x^2} \qquad \text{eq17}$$

2.4 Electrode-electrolyte interface

If a metal (or in general: any solid state body) is immersed into an electrolyte, it is referred to as an *electrode*. In general, the electrochemical potentials of the metal and the electrolyte are not equal. Upon contact, equilibrium will be established by an exchange of species. In case of a redox electrolyte and a noble metal electrode, only electrons are exchanged. In particular, no metal ions from the electrode will go into solution. Such an electrode is then called *redox electrode*.

The exchange of electrons leads to an electrical potential difference between electrolyte and electrode, the so-called *built-in* potential. Since the charges in the electrolyte are freely mobile, opposite charges will arrange themselves at the metalelectrolyte

interface. This double layer is called the *Helmholtz double layer* [(56)].

2.4.1 Helmholtz double layer

The Helmholtz double layer acts like a capacitor with a small (a few angström) plate distance. The capacitance can be measured by impedance spectroscopy. In the simplest model, the potential gradient is linear (Fig. 14).

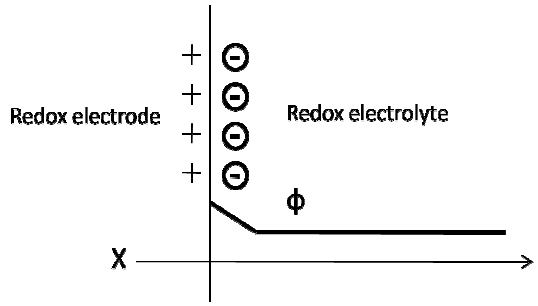

Fig. 14: Arrangement of opposite charges in a Helmholtz double layer

.

In particular, the complete electrical potential drops over the Helmholtz layer. Thus, in the inside of the electrolyte no electrical field exists. In a redox electrolyte, the electrical field can be very efficiently screened. It is important to note, that a redox

electrolyte contains charged species, which do not participate in the redox reaction (redox inactive or inert species). Those species can very effectively arrange themselves in a Helmholtz layer, in order to screen any electrical potential differences. In case of the DSC, the cation of the iodide salt is the redox-inactive species, e.g. an imidazolium$^+$ or Li^+.

2.5 Charge transfer over an electrode-electrolyte interface

In equilibrium, no net charge transport occurs over the electrode-electrolyte interface. The Helmholtz double layer is formed with the built-in potential (see previous section).

However, if an external potential is applied to the electrode, a current will flow over the electrode-electrolyte interface.

In general, the charge transfer reaction is controlled by the applied potential. A higher potential will lead to a higher current flow over the interface. Additionally, the charge transfer will be determined by the concentration of the redox species in the electrolyte at the interface. Here, two cases can be differentiated. If the charge transfer reaction does *not* depend on the concentration of the redox ions at the interface, the reaction is called *potential controlled*. This is the case, if the charge transfer is slow, and/or the concentration of redox partners is high.

If the charge transfer reaction *does* depend on the concentration of the redox ions at the interface, the reaction is called *diffusion controlled*. This is the case, if the charge transfer over the interface occurs very rapidly, and/or the concentration of redox partners is too low. Then the reaction can only proceed, if new redox partners reach the electrode by diffusion.

2.5.1 Potential controlled reaction: Butler Vollmer equation

In a potential controlled charge transfer, the current over the interface is independent of the concentrations of the redox ions at the interface. It is only dependant on the applied potential. In this case, the current-voltage characteristics can be described by the Butler-Vollmer equation [Vetter '61]:

$$j(V) = j_0 \left(exp\left(\frac{e_0}{k_B T} V\right) - exp\left(-(1-\beta)\frac{e_0}{k_B T} V\right)\right) \qquad \text{eq18}$$

The current density j over the interface is determined by the applied potential V, the

exchange current density *j*0 and the symmetry parameter $\beta = 0\ldots1$. A symmetry parameter of 0.5 describes a charge transfer reaction, which is symmetric under positive (forward) and negative (reverse) potential *V*. An asymmetric reaction can be accounted for by $\beta \neq 0.5$, as seen in Fig. 15 .

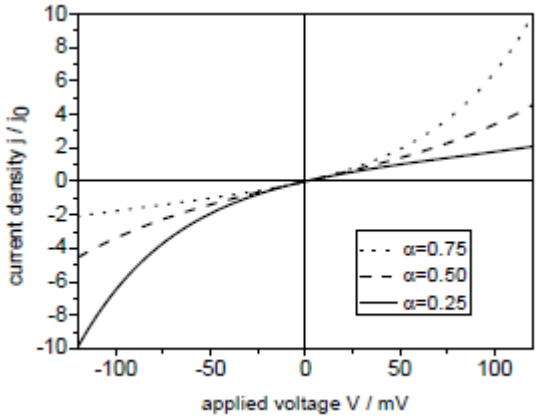

Fig. 15: Current-voltage characteristics of the Butler-Vollmer equation for varying symmetry parameter β

For small potential $V \leq 10\text{mV}$ the Butler Vollmer equation can be approximated by first term Taylor expansion to:

$$j(V) = \underbrace{j_0 \frac{e_0}{k_B T}}_{=\frac{1}{R_{CT}}} V \qquad eq19$$

Thus, the *charge transfer resistance* *R*CT is defined. *R*CT is of dimension Ω cm². This is the same dimension as for a *contact resistance*, the total resistance decreases with electrode (or contact) area.

In the DSC, the charge transfer resistance at the TCO-electrolyte interface can be reduce drastically by the catalyst platinum. Then, if the electrolyte is not diffusion-limited, the approximation eq19 is valid. If the TCO electrode is not coated with platinum, however, the charge transfer is inhibited and the Butler-Vollmer equation (eq18) must be used.

2.5.2 *Diffusion controlled reaction*

In a diffusion controlled charge transfer reaction, the concentration of redox ions at the interface is reduced drastically, because the redox ions are consumed faster, than they can diffuse to the electrode. The change in electrochemical potential caused by the change in concentration in the redox electrolyte is described by the Nernst equation eq9. In the DSC, electrons from the platinum counter electrode react with the triiodide ($I3^-$) in the electrolyte. The change in electrochemical potential $\Delta\ \eta$ due to a change in triodide concentration is then:

$$\Delta\eta = \frac{k_B T}{m} \ln\left(\frac{c^0_{I_3^-}}{c^E_{I_3^-}}\right) \qquad \text{eq20}$$

Here, $C^E_{I_3^-} and\ C^0_{I_3^-}$ are the triiodide concentrations at the electrode, and far away from the electrode (the constant, initial concentration), respectively.

Assuming a linear concentration profile from the electrode to a point inside the ectrolyte, where the initial (constant) concentration of triodide is present, the current density is:

$$j = e_0 D \frac{c^0_{I_3^-} - c^E_{I_3^-}}{\delta} \qquad \text{eq21}$$

Here, δ is the distance to the inside of the electrolyte, where the initial concentration of triiodide is existing, and D is the diffusion constant of triiodide.

By using the *diffusion limited current density* j_{lim} of an electrolyte (this will be described in 2.5.5), the current-voltage characteristics can be obtained. The diffusion limited current density j_{lim} is the current, which flows when the concentration at the electrode has diminished completely $C^E_{I_3^-}$=0:

$$j_{lim} = e_0 D \frac{c^0_{I_3^-}}{\delta} \qquad \text{eq22}$$

It follows:

$$\frac{j}{j_{lim}} = \frac{c^0_{I_3^-} - c^E_{I_3^-}}{c^0_{I_3^-}} = 1 - \frac{c^E_{I_3^-}}{c^0_{I_3^-}} \qquad \Rightarrow \quad \frac{c^0_{I_3^-}}{c^E_{I_3^-}} = \frac{j_{lim}}{j_{lim} - j}$$ eq 23

Substituting this expression into eq20 yields:

$$V = \frac{\Delta\eta}{e_0} = \frac{k_B T}{e_0 m} \ln\left(\frac{j_{lim}}{j_{lim} - j}\right)$$ eq24

The current-voltage characteristics for a diffusion controlled charge transfer reaction is thus:

$$j(V) = -j_{lim}\left[\exp\left(-V\frac{e_0 m}{k_B T}\right) - 1\right]$$ eq25

This curve is shown qualitatively in Fig. 16. For small voltages the current increases roughly linearly and then approaches the diffusion-limited current j_{lim}.

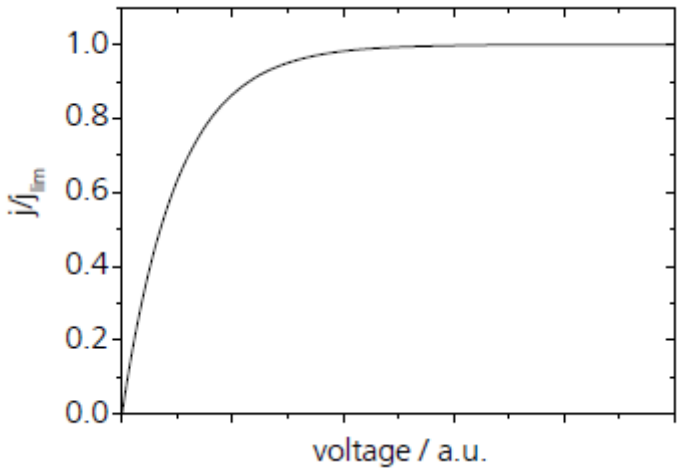

Fig. 16: Current-voltage characteristics for a diffusion controlled charge transfer reaction of an electrode-electrolyte interface. The current j is related to the diffusion limited current j_{lim}

In the DSC, the catalytic platinum layer at the counter electrode reduces the charge transfer resistance drastically. The qualitative curve progression at the platinum counter electrode is therefore given by Fig. 16 (diffusion controlled) rather than Fig. 15 (Butler Vollmer).

2.5.3 *General case*

In general, a combination of the two discussed cases occurs. For small applied potentials, a Butler Vollmerian behaviour is observed and for large applied potentials and large currents, the current approaches the diffusion limited current. In between, a mixed region exists, where both processes are combined Fig. 17.

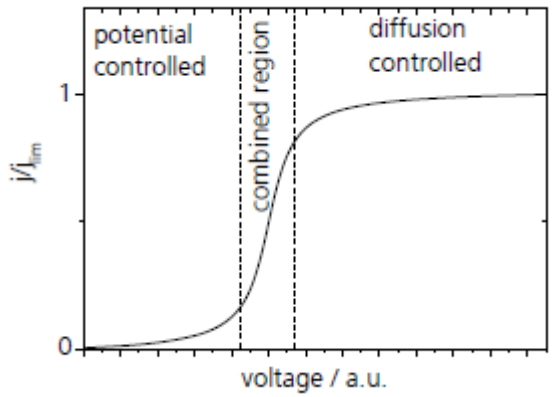

Fig. 17: Current-voltage characteristics of the charge transfer reaction at an electrode-electrolyte interface

In general, three regions can be distinguished: a potential controlled region at low voltages and a diffusion controlled region, where the current approaches the diffusion limited current j_{lim} of the electrolyte. In between, a region exists where both processes are combined.

2.5.4 *Nernst diffusion layer*

From equation eq17 it is clear, that the *steady state* concentration profile will be a linear profile in most cases. Especially, for a one or two electrode set-up, where species are generated and consumed only at one or two points (in a one-dimensional problem), this is the case. From equation eq16 it is clear, that the *steady state* current is then easily determined by the concentration of the considered species.

Fig. 18 and Fig. 19 show the qualitative steady state concentration profiles in a one and two electrode setup, respectively. Upon increasing the applied potential, the redox species is consumed at one electrode and a linear steady state profile is formed.

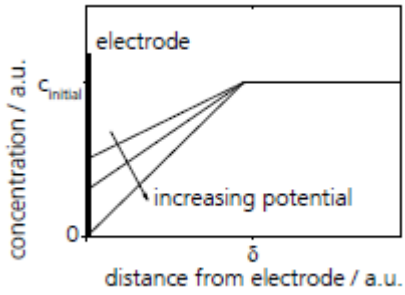

Fig. 18: Qualitative steady state concentration profiles in a one electrode setup

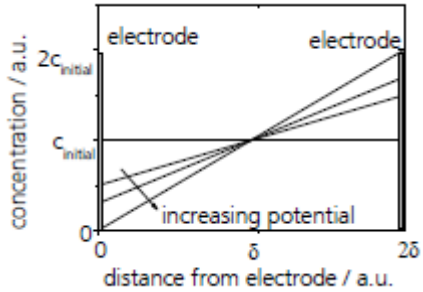

Fig. 19: Qualitative steady state concentration profiles in a two electrode setup

For the case of the one electrode setup the Nernst diffusion layer is defined to thickness δ, where far away from the electrode the initial redox concentrations exist (due to convection). The Nernst diffusion layer is typically about 100 µm in a DSC, but exact values are usually not known and depend on the diffusion constant and convection [(58)].

For the case of the two electrode setup, with electrode distances small enough to prevent convection, the Nernst diffusion layer extends through the whole system. In the two electrode setup, redox species are produced at the 2nd electrode (of opposite polarity), as they are consumed at the 1st electrode. Here, the Nernst diffusion layer is defined to thickness δ, which is half the electrode distance.

2.5.5 *Diffusion-limited current*

In Fig. 18 and Fig. 19 the steady state current is then given by:

$$j = e_0 D \frac{c_{initial} - c(0)}{\delta} \qquad \text{eq26}$$

If the applied potential is increased, the concentration of redox species at the electrode

$c(0)$ diminishes. Obviously, if the concentration reaches zero, the current cannot increase further, even if the potential is increased further. The maximum steady state current is therefore the so-called "diffusion limited current j_{lim}"

$$j_{lim} = e_0 D \frac{c_{initial}}{\delta} \qquad \text{eq27}$$

With the definitions used, it is important to note, that the Nernst diffusion layer δ is half the electrode distance in a two electrode setup.

Furthermore, it should be mentioned, that the diffusion limited current is the maximum possible steady state current. Transient currents can indeed be much larger. Especially, when the potential is stepped from equilibrium to that for a diffusion controlled reaction, the initial currents are very large, since the initial concentration at the electrode is consumed first. The current then drops until it reaches the diffusion limited current.

2.6 I-V characteristics of a solar cell

A typical current-voltage characteristics of a solar cell is shown in Fig. 20. The important electrical parameters are the short-circuit current density *j*SC, the open-circuit voltage V_{OC} and the maximum power point P_{MAX} (or *MPP*) with its corresponding current-density
and voltage (j_{MP}, V_{MP}).

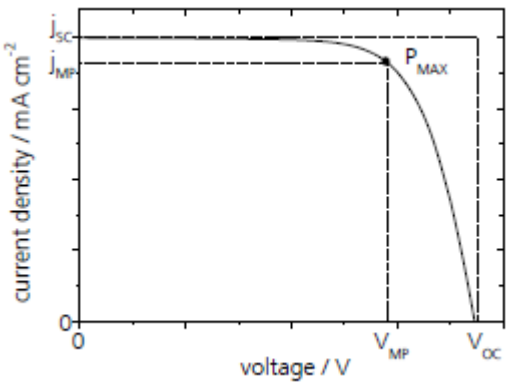

Fig. 20: Typical I-V curve of a solar cell. The important electrical parameters are the short-circuit current density *j*SC, the open-circuit voltage *V*OC and the maximum power point *P*MAX with its corresponding current-density and voltage (*j*MP, *V*OC)

In this work, the current *I* of a solar cell is in the majority of cases related to the area of the cell, in order to obtain a current density *j*, for obvious reasons. The current density-voltage characteristics is nevertheless referred to as *I-V curve*. If the current is plotted instead of the current density, the short-circuit current density is always additionally stated in the Figure caption.

The fill factor FF of a solar cell is defined by:

$$FF = \frac{P_{MAX}}{j_{SC} V_{OC}} \qquad \text{eq28}$$

Here, P_{MAX} is also related to area with the dimension W/cm².

And the efficiency *eta*:

$$eta = \frac{P_{MAX}}{\Phi_{incident}} \qquad \text{eq29}$$

Here, incident Φ is the power of the incident irradiation with dimension W/cm².

The efficiency of a solar cell is highly dependant on the incident irradiation. The standard reporting conditions (SRC) are under the so-called *AM 1.5 global* spectrum. It is equivalent to the spectrum of the sun with an incident angle, such that the light path through the atmosphere is 1.5 times longer than for perpendicular incident irradiation.

The intensity of AM 1.5 global is 100 mW/cm² or 1000 W/m² [(60)]. This light intensity is also referred to as *1 sun*.

2.6.1 *One-diode model*

The I-V curve of a solar cell can be modelled by the *one-diode model* [(54)]. It is valid if the current is not limited by transport resistances. In a DSC, these would be the diffusion in the electrolyte or the diffusion in the TiO2. Thus, if transport limitations can be neglected, the one-diode model from solid-state semiconductor physics can be adopted for the electrochemical DSC.

Many detailed models have been developed, which explain the I-V curve of a DSC from microscopic parameters [(61), (62)]. In this work, however, it is sufficient to describe the macroscopic I-V curve of a DSC by the one-diode model [(54)]:

$$I(V) = I_{sat}\left(\exp\frac{e_0 V}{m_D k_B T} - 1\right) + I_{SC}$$

eq30

Here, *I*sat is the diode saturation current and *m*D is the diode ideality factor. The diode ideality factor is 1 from semiconductor theory. However, it has been empirically found, that real diodes deviate from the ideal diode equation (*m*D=1). Therefore, the ideality factor has been introduced. In real silicon diodes the ideality factor is 2 for low currents and 1 for high currents. The one-diode model is sometimes also called the *standard solar cell equation*.

In a real solar cell, the series resistance and the shunt resistance have to be taken into account (Fig. 21).

The I-V curve then becomes:

$$I(V) = I_{sat}\left(\exp\frac{e_0 V - e_0 R_S I}{m_D k_B T} - 1\right) + I_{SC} + \underbrace{\frac{V - R_S I}{R_{Sh}}}_{I_{Sh}}$$

eq31

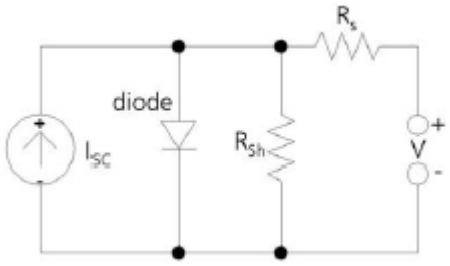

Fig. 21:Equivalent circuit of the one-diode model with series resistance *R*s and shunt resistance *R*Sh

The influence of the series and shunt resistance is shown in Fig. 22.

In Fig. 22 it can be seen, that the one-diode model has been introduced in a form, which yields negative photocurrents. Considering, that a solar cell is essentially a diode this make sense from a physicist's point of view: especially in the dark, a positive voltage leads to a positive current.

In solar cell engineering, however, the I-V curve of a solar cell is often displayed as in Fig. 20: the photocurrent, and thus the produced power is of positive sign.

In this work, both conventions will be used. In particular, if the I-V curves of setups are investigated, which exhibit diode behaviour, but are not a complete solar cell, the physicist's convention will be used. When complete solar cells are investigated, the engineer's convention is mostly used, as to follow the style of most publications in this field [(63)].

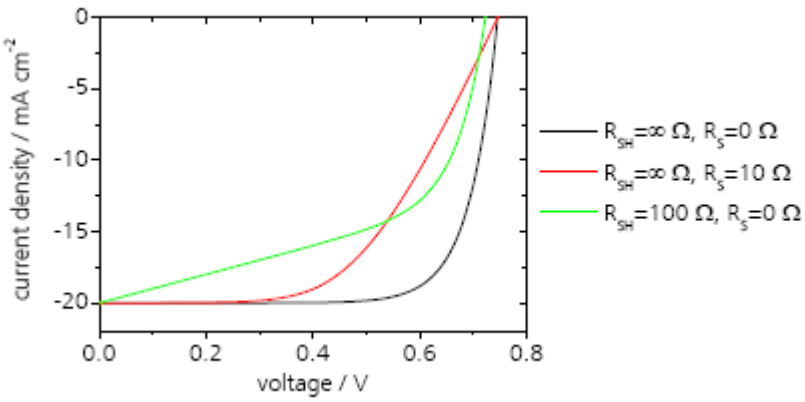

Fig. 22: I-V curves of a solar cell with the one-diode model . The series resi stance *R*s and shunt resistance *R*Sh have been varied

3. Sealing materials

An adhesive, or glue, is a mixture in a liquid or semi-liquid state that adheres or bonds items together. Adhesives may come from either natural or synthetic sources. Some modern adhesives are extremely strong, and are becoming increasingly important in modern construction and industry. The types of materials that can be bonded using adhesives are virtually limitless. They can be electrically and thermally conductive or non-conductive. The effectiveness of an adhesive depends not only on its being inert towards the compounds of the materials with which it is in direct contact, but also on its compatibility with the substrates with which it has to adhere. This mean that a good sealant for plastic substrates could be not good for glass ones. The adhesion capacitance depends mainly on the compatibility of the functional groups of the side chains of the two materials, stronger the bond is more effective the seal will be. This compatibility can be improved or be created by the use of primers, unfortunately these materials have to be develop ad hoc to give the best performance. Essentially their functional groups are compatible with both the ones of the materials with which have to go in contact creating a kind of bridge between substrates.

The oldest known adhesive, dated to approximately 200,000 BC, is from spear stone flakes glued to a wood with birch-bark-tar, which was found in central Italy (64). The use of compound glues to haft stone spears into wood dates back to round 70,000 BC. Evidence for this has been found in Sibudu Cave, South Africa and the compound glues used were made from plant gum and red ochre (65). The Tyrolean Iceman had weapons fixed together with the aid of glue (66).

Nowadays there are several categories of adhesives, the most representatives can be summarized in the following list:

- Natural adhesives:Natural adhesives are made from inorganic mineral sources, or biological sources such as vegetable matter, starch (dextrin), natural resins or from animals e.g. casein or animal glue. They are often referred to as bioadhesives. One example is a simple paste made by cooking flour in water. Animal glues are traditionally used in bookbinding, wood joining, and many other areas but now are largely replaced by synthetic glues. Casein are mainly

used in glass bottle labelling. Starch based adhesives are used in corrugated board production and paper sack production, paper tube winding, wall paper adhesives. Another form of natural adhesive is blood albumen (made from protein component of blood), which is used in the plywood industry. Animal glue remains the preferred glue of the luthier.

- Synthetic adhesives: Elastomers, thermoplastics, Emulsion, and thermosetting adhesives based on polyvinyl acetate, epoxy, polyurethane, cyanoacrylate polymers are examples of synthetic adhesives.
- Drying adhesives: These adhesives are a mixture of ingredients (typically polymers) dissolved in a solvent. White glue and rubber cements are members of the drying adhesive family. As the solvent evaporates, the adhesive hardens. Depending on the chemical composition of the adhesive, they will adhere to different materials to greater or lesser degrees. These adhesives are typically weak and are used for household applications.
- Contact adhesives: Contact adhesives must be applied to both surfaces and allowed some time to dry before the two surfaces are pushed together. Once the surfaces are pushed together, the bond forms very quickly. Natural rubber and polychloroprene (Neoprene) are commonly used contact adhesives.
- Hot adhesives, also known as hot melt adhesives, are simply thermoplastics applied in molten form (in the 65-180 C range) which solidify on cooling to form strong bonds between a wide range of materials.
- Emulsion adhesives Milky-white dispersions often based on polyvinyl acetate. Used extensively in the woodworking and packaging industries. Also used with fabrics and fabric-based components, and in engineered products such as loudspeaker cones
- UV and light curing adhesives also known as light curing materials (LCM), have become popular within the manufacturing sector due to their rapid curing time and strong bond strength. Light curing adhesives can cure in as little as a second and many formulations can bond dissimilar substrates (materials) and withstand harsh temperatures. These qualities make UV curing adhesives essential to the manufacturing of items in many industrial markets such as electronics, telecommunications, medical, aerospace, glass, and optical. Unlike

traditional adhesives, UV light curing adhesives not only bond materials together but they can also be used to seal and coat products.

- Pressure sensitive adhesives (PSA) form a bond by the application of light pressure to marry the adhesive with the adherend. They are designed with a balance between flow and resistance to flow. The bond forms because the adhesive is soft enough to flow (i.e. "wet") the adherend. The bond has strength because the adhesive is hard enough to resist flow when stress is applied to the bond. Once the adhesive and the adherend are in close proximity, molecular interactions, such as Van der Waals forces, become involved in the bond, contributing significantly to its ultimate strength.

Numerous sealing tests were performed by using the most diverse adhesives belonging to the most diverse families and subfamilies. Only a few thermoplastic like Bynel® and Surlyn® (DuPont) and acrylic-based resins, like Dymax 3022 showed good resistance to chemical attack of the electrolyte, all others adhesives have proved ineffective in keeping the liquid inside the internal chamber and in not interacting with the electrolyte itself. In the following paragraphs there will be presented only the sealant that have shown good characteristics for DSC application.

3.1 Thermoplastic materials

A thermoplastic, also known as thermosoftening plastic is a polymer that turns to a liquid when heated and freezes to a very glassy state when cooled sufficiently.

Thermoplastics are elastic and flexible above a glass transition temperature T_g, specific for each one—the midpoint of a temperature range in contrast to the sharp melting point of a pure crystalline substance like water. Below a second, higher melting temperature, T_m, also the midpoint of a range, most thermoplastics have crystalline regions alternating with amorphous regions in which the chains approximate random coils. The amorphous regions contribute elasticity and the crystalline regions contribute strength and rigidity, as is also the case for non-thermoplastic fibrous proteins such as silk. (Elasticity does not mean they are particularly stretchy; e.g., nylon rope and fishing line.) Above T_m all crystalline structure disappears and the chains become randomly inter dispersed. As the temperature increases above T_m, viscosity gradually decreases without any distinct phase change.

Some thermoplastics normally do not crystallize: they are termed "amorphous" plastics and are useful at temperatures below the T_g. They are frequently used in applications where clarity is important. Some typical examples of amorphous thermoplastics are PMMA, PS and PC. Generally, amorphous thermoplastics are less chemically resistant and can be subject to stress cracking. Thermoplastics will crystallize to a certain extent and are called "semi-crystalline" for this reason. Typical semi-crystalline thermoplastics are PE, PP, PBT and PET. The speed and extent to which crystallization can occur depends in part on the flexibility of the polymer chain. Semi-crystalline thermoplastics are more resistant to solvents and other chemicals. If the crystallites are larger than the wavelength of light, the thermoplastic is hazy or opaque. Semi-crystalline thermoplastics become less brittle above T_g. If a plastic with otherwise desirable properties has too high a T_g, it can often be lowered by adding a low-molecular-weight plasticizer to the melt before forming (Plastics extrusion; molding) and cooling. A similar result can sometimes be achieved by adding non-reactive side chains to the monomers before polymerization. Both methods make the polymer chains stand off a bit from one another. Before the introduction of

plasticizers, plastic automobile parts often cracked in cold winter weather. Another method of lowering T_g (or raising T_m) is to incorporate the original plastic into a copolymer, as with graft copolymers of polystyrene, or into a composite material. Lowering T_g is not the only way to reduce brittleness. Drawing (and similar processes that stretch or orient the molecules) or increasing the length of the polymer chains also decrease brittleness.

Thermoplastics can go through melting/freezing cycles repeatedly and the fact that they can be reshaped upon reheating gives them their name. This quality makes thermoplastics recyclable. The processes required for recycling vary with the thermoplastic. The plastics used for soda bottles are a common example of thermoplastics that can be and are widely recycled. Animal horn, made of the protein α-keratin, softens on heating, is somewhat reshapable, and may be regarded as a natural, quasi-thermoplastic material.

Although modestly vulcanized natural and synthetic rubbers are stretchy, they are elastomeric thermosets, not thermoplastics. Each has its own T_g, and will crack and shatter when cold enough so that the crosslinked polymer chains can no longer move relative to one another. But they have no T_m and will decompose at high temperatures rather than melt. Recently, thermoplastic elastomers have become available.

The literature on thermoplastics is huge, and can be quite confusing, as the same chemical can be available in many different forms (for example, at different molecular weights), which might have quite different physical properties. The same chemical can be referred to by many different tradenames, by different abbreviations; two chemical compounds can share the same name; a good example of the latter is the word "Teflon" which is used to refer to a specific polymer (PTFE); to related polymers such as PFA, and generically to fluoropolymers.

Furthermore, over the last 30 years, there has been tremendous change in the plastics industry, with many companies going out of business or merging into other companies. Many production plants frequently changed hands or have been relocated to emerging countries in Eastern Europe or Asia, with different trademarks.

Thermoplastic Bynel® (DuPont), as said above, shows good resistance towards the electrolyte compounds, it comes from the Polyethylene family, more precisely it is a Linear low density polyethylene (LLDPE).

Polyethylene PE

Polyethylene or polythene (IUPAC name polyethene or poly(methylene)) is the most widely used plastic, with an annual production of approximately 80 million metric tons. It is a thermoplastic polymer consisting of long chains of the monomer ethylene (IUPAC name ethene). The recommended scientific name *polyethene* is systematically derived from the scientific name of the monomer. (67) (68) In certain circumstances it is useful to use a structure-based nomenclature; in such cases IUPAC recommends *poly(methylene)* (68) (poly(methanediyl) is an non-preferred alternative (69)). The difference in names between the two systems is due to the *opening up* of the monomer's double bond upon polymerisation.

The name is abbreviated to **PE** in a manner similar to that by which other polymers like polypropylene and polystyrene are shortened to PP and PS respectively. In the United Kingdom the polymer is commonly called **polythene**, although this is not recognized scientifically.

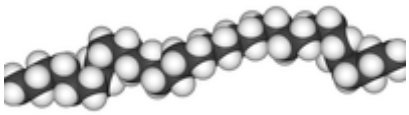

Fig. 23: Space-filling model of a polyethylene **chain.**

The ethene molecule (known almost universally by its common name ethylene) C_2H_4 is $CH_2{=}CH_2$, Two CH_2 groups connected by a double bond, thus:

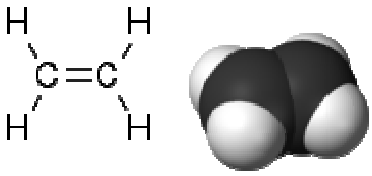

Fig. 24: polyethylene molecule

Polyethylene contains the chemical elements carbon and hydrogen.

Polyethylene is created through polymerization of ethene. It can be produced through radical polymerization, anionic addition polymerization, ion coordination polymerization or cationic addition polymerization. This is because ethene does not have any substituent groups that influence the stability of the propagation head of the polymer. Each of these methods results in a different type of polyethylene.

Polyethylene is classified into several different categories based mostly on its density and branching. The mechanical properties of PE depend significantly on variables

such as the extent and type of branching, the crystal structure and the molecular weight.

- Ultra high molecular weight polyethylene (UHMWPE)
- Ultra low molecular weight polyethylene (ULMWPE or PE-WAX)
- High molecular weight polyethylene (HMWPE)
- High density polyethylene (HDPE)
- High density cross-linked polyethylene (HDXLPE)
- Cross-linked polyethylene (PEX or XLPE)
- Medium density polyethylene (MDPE)
- Linear low density polyethylene (LLDPE)
- Low density polyethylene (LDPE)
- Very low density polyethylene (VLDPE)

Our attention will be focused on the LLDPE family that in past shown good properties for DSC application. This kind of polymers was and are widely utilized in DSC construction architectures, especially in test sell contruction.

3.1.1 *Linear low density polyethylene (LLDPE)*

LLDPE is defined by a density range of 0.915–0.925 g/cm^3. LLDPE is a substantially linear polymer with significant numbers of short branches, commonly made by copolymerization of ethylene with short-chain alpha-olefins (for example, 1-butene, 1-hexene and 1-octene). LLDPE has higher tensile strength than LDPE, it exhibits higher impact and puncture resistance than LDPE. Lower thickness (gauge) films can be blown, compared with LDPE, with better environmental stress cracking resistance but is not as easy to process. LLDPE is used in packaging, particularly film for bags and sheets. Lower thickness may be used compared to LDPE. Cable covering, toys, lids, buckets, containers and pipe. While other applications are available, LLDPE is used predominantly in film applications due to its toughness, flexibility and relative transparency. As mentioned previously one of the materials that showed greater resistance to the electrolyte was Bynel® that belongs right to this family of materials. Bynel is the main sealing material uses in this work, in this chapter there will be also shown the sealing procedure and the machinery involved in such a process.

3.2 Fluid or semi-fluid adhesives

An alternative to the use of thermoplastics as sealing may be the use of liquid or semi-liquid adhesive. There are hundreds of different materials belonging to dozens of different chemical types but for the vast majority turned out to be not inert towards the components of the electrolyte or ineffective in the mechanical encapsulation of the liquid inside the chamber of the device. Use a liquid or semi-liquid adhesive undoubtedly introduce additional evidence of difficulties in the building process of the solar cell. So, the material to be employed must provide one or more advantages that can make it a good substitute against the thermoplastic. An acrylic-based adhesive that is also UV curable provides to the sealing process two very interesting properties, namely speed of processes and operations performed at room temperature, which the thermoplastic cannot provide. In the following paragraphs there will presented first what is a UV curable resin and then a the application as primary sealer of one of this that from preliminary tests gave interesting results (Dymax 3022).

3.2.1 Light curing adhesives

Before introducing the UV curable resin previously named it is interesting to understand what is and how it work an Ultra Violet curable material. Photo-curable (or light-curable) adhesives, which cure when exposed to light, are composed of a number of chemical species. In common with other adhesive formulations, they typically contain low-medium molecular weight polymers, - oligomers -, that impart a major influence on the physical and mechanical properties of the cured system, e.g. whether it is hard or soft, rigid or flexible. In addition to the oligomers, monomers are added to modify the viscosity of the uncured adhesive and control cross-link density during subsequent polymerization. Optional additives in the adhesive composition can include adhesion promoters, wetting agents, pigments and fillers for example. Finally, there is one component that is unique to this class of adhesives, a photo-initiator.

The photo-initiator, typically representing less than 5% of the adhesive formulation, is best regarded as a dormant hardener/curing agent. In the uncured, unexposed adhesive it is unreactive towards the rest of the components in the adhesive. However, when the adhesive is exposed to light of the correct wavelength, and sufficient intensity, the photo-initiator absorbs this radiation and is converted into a highly reactive species that rapidly initiates copolymerisation of the oligomers and monomers. Progression of

this copolymerisation reaction is what we observe as hardening, or curing, of the adhesive, i.e. conversion from a liquid to a solid state.

This feature, where the adhesive only cures upon exposure to light, is sometimes referred to as 'command cure' or 'cure on demand' and means that, as long as the adhesive is not inadvertently exposed to light wavelengths that will initiate curing, pot life of the adhesive is essentially unlimited, thereby giving ample time for positioning of the substrates to be bonded (Fig. 25).

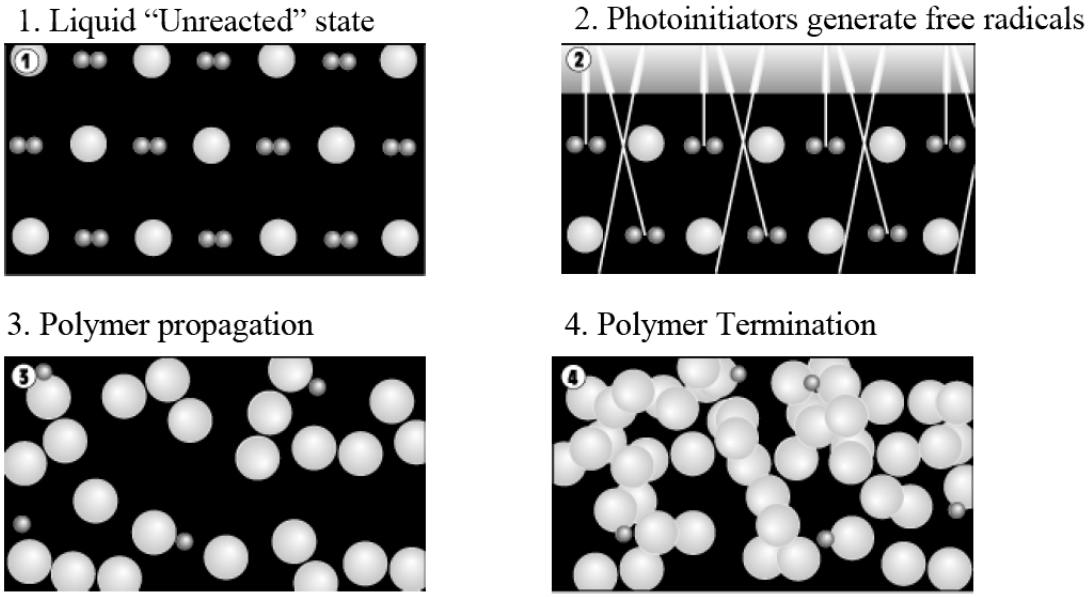

Fig. 25:example of a light cure process (70)

The wavelength of light required to initiate curing typically falls in the long-wavelength UV region of the electromagnetic spectrum, between 325 and 380nm. In industrial applications of these adhesives, such UV light is provided by medium-pressure mercury lamps incorporated into sophisticated curing systems designed to deliver the light either in a focused spot, strip or defocused area ('flood') configuration. With appropriately-formulated adhesives, visible light can also be used to effect cure. Blue light, at a wavelength of 470nm, is usually used and offers advantages in terms of safety and the ability to effect cure of relatively deep sections or filled/pigmented adhesives.

Although perhaps obvious, it is important to note that the spectral emission of the curing system must match the spectral absorption of the photoinitiator(s) present in the adhesive. Suppliers of photocurable adhesives either provide information on recommended wavelength and intensity of light on the technical data sheet of the adhesive, or on request.

The vast majority of photocurable adhesives on the market today are based on acrylate/methacrylate chemistry. The 'toolbox' of such raw materials available to adhesive formulators is very large and this translates into quite a number of suppliers offering adhesives with a very diverse range of properties. In general, this chemistry allows for very rapid cure times, (less than one second in the case of adhesives for DVD production, for example), but any adhesive exposed to air, at the edges of bonded parts for example, can suffer from an effect known as 'oxygen inhibition', where diffusion of atmospheric oxygen inhibits the curing reaction resulting in a tacky and/or greasy surface (a few micrometers thick) on the otherwise cured adhesive. A number of approaches are available to circumvent this effect (e.g. inert gas blanketing during cure).

Less common, but gaining increasing acceptance in a number of applications, are photocurable adhesives based on epoxy chemistry. These adhesives do not fully cure as rapidly as their acrylate counterparts, - often a thermal post-cure is required to achieve optimum properties -, but can provide better adhesion strengths, particularly on certain metals, and do not suffer from the oxygen inhibition effect.

As the curing process is initiated by light, this means that at least one of the substrates to be bonded must be transparent to the initiating wavelength(s). This is often not as apparent as it may seem. For example, many transparent plastics inherently absorb UV light, and this absorbance will be increased if the plastic contains anti-yellowing additives (typically used in outdoor- and medical-grade plastics). Conversely, relatively thin, white alumina, opaque to the human eye, will transmit sufficient blue light to allow the use of visible light-curable adhesives in the assembly of fibre optic connectors, while the ability of blue light to penetrate highly-filled, opaque adhesives allows the use of the latter as dental filling composites in preference to mercury amalgams.

In view of the above, photocurable adhesives will not cure if they are shadowed from the initiating light. The terms 'dark cure' or 'shadow cure', used by some adhesive suppliers, suggest otherwise, but these actually refer to adhesives that continue to cure once the initiating light has been removed, i.e. epoxy-based adhesives. However, the curing reaction does not progress into bond areas initially shadowed from the incident light. For such joint configurations, photocurable adhesives are available with secondary cure capability, typically effected by heat although other options, e.g. moisture- or anaerobic-cure, can also be provided.

For bonding two substrates that are both opaque to the initiating radiation, a handful of epoxy-based photocurable adhesives are available that have a 'delayed cure' feature. With these the adhesive is applied to the bonding surface of one substrate then given a relatively short exposure to the initiating light. This short exposure 'activates' the adhesive which remains in a liquid state for a short period of time, - the so-called 'open time' -, during which the second substrate is attached. Once the open time has expired the adhesive begins to cure, bonding the two substrates (71).

3.2.2 *Urethane Acrylate*

The UV curable resin tested comes from the Urethane acrylates family. These kind of materials are produced by reacting polyisocyanates with hydroxyl alky acrylates, usually along with hydroxyl compounds, to produce the desired set of properties. Urethane acrylates are the most expensive of the acrylates. There are many different types of urethane acrylate oligomers having variations in the following parameters.

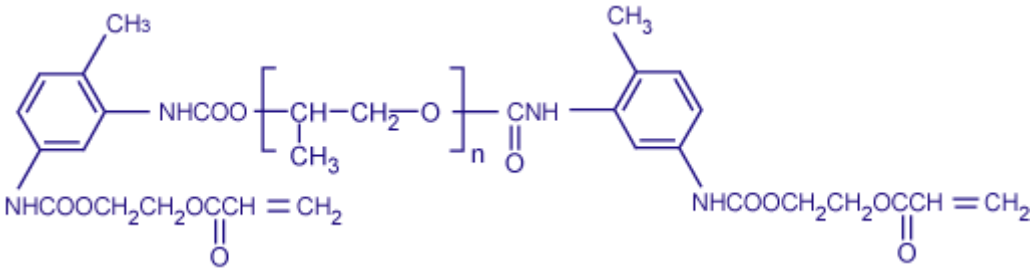

Fig. 26: Example: typical urethane acrylate oligomer

Its functionality varies from one to six. Lower functionality results in lower reactivity, better flexibility, and lower viscosity. Monofunctional urethane acrylates are low viscosity, specialty products used to improve adhesion to difficult substrates and to improve flexibility. High functionality products (4 and higher) have niche applications as well. They are used to improve reactivity, scratch resistance, chemical resistance, and other physical properties. Because of their high viscosity, they are generally blended with other resins.

Four types of isocyanates are used for urethane acrylates. Monoisocyanates are used for monofunctional acrylates only (see above). Diisocyanates are the most widely used and can be divided into aliphatic diisocyanates and aromatic diisocyanates. The incorporation of an aromatic diisocyanate makes the resulting coating harder and abrasion resistant. The higher cost aliphatic diisocyanates are slightly more flexible. However, they are non-yellowing. Aliphatic urethane acrylates are used for topcoats,

optical fibers, flexible packaging, etc. Polymeric isocyanates are used for higher functionality urethane acrylates (see above).

The polyol is the backbone of the urethane acrylate. They are essentially polyether or polyester with functionality ranging from two to four. Polyether urethane acrylates are generally more flexible, provide lower cost, and have slightly lower viscosity. Polyester urethane acrylates have less hydrolytic stability but are non-yellowing. The polyol modifier determines the molecular weight for di- and trifunctional urethane acrylate (72).

3.3 Sealing procedure

Each type of adhesive needs to be treated in a particular manner to achieve the best results, for example, use an improper proportion between the constituents of a two-component epoxy glue may involve obtaining a sealing ineffective against environmental agents. It is extremely difficult to find an adhesive that combines all the characteristics required to be an effective sealant for this technology. It is certainly easier to find different sealants, that applied to a given sequence, can succeed in ensuring a lasting and effective seal thus ensuring the isolation of the constituent components of the solar cell from the external elements (like oxygen and water vapor). For this reason the approach used to encapsulate this type of solar cells involves the application of a primary and a secondary sealant, the first type has essentially the characteristic of being unattackable by the electrolytic solution and it has also to ensures the contents of the liquid into the chamber of the solar cell. Whilst, the secondary sealant is applied externally to work essentially as a barrier against element such as oxygen and water.

In the following paragraphs will be discuss the techniques to apply thermoplastics and UV curable resins as a primary sealant, the evaluation of the sealant procedures there were performed on symmetrical devices (substrate-FTO-electrolyte-Catalyst-FTO-substrate).

3.3.1 Hot approach for thermoplastic

As said above a thermoplastic is a polymer that turns to a liquid when heated and freezes to a very glassy state when cooled sufficiently. The thermoplastic material chose at the beginning of this work was Surlyn® 1701(DuPont), but its melting point (more or less 90 °C) is too low for photovoltaic applications. For this reason the attention passed on Bynel® 4100 series (DuPont) that has a melting point higher than the Surlyn® one. Bynel sheets of thickness of 60 microns are cut in an appropriate form through the use of an automatic cutter (Fig. 27).

Fig. 27: Graphtec craft robo cutter

The masks obtained is then affixed around the active area of the solar cell to be used as primary sealer (Fig. 28)

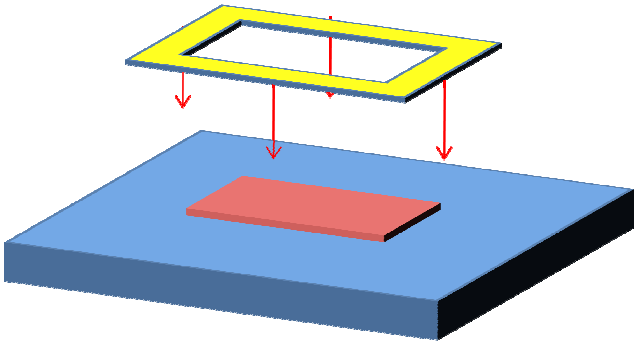

Fig. 28: bynel mask used as primary sealer

To achieve the hot lamination it is used a Memo^{Tm} pneumatic t-shirt hot-press (Fig. 29).

Fig. 29: Memo^{Tm} t-shirt hot press

With this machinery the two substrates (photoelectrode and counterelectrode) are pressed together for some seconds at a define temperature and pressure in order to melt the bynel mask and obtain a fair lamination, then the devise is cooled at room temperature. This procedure by itself doesn't guarantee a good lamination, in fact on the bynel peace after the hot press are often visible signs of an incorrect adhesion, like bubbles or opaque areas as it can be seen in Fig. 30.

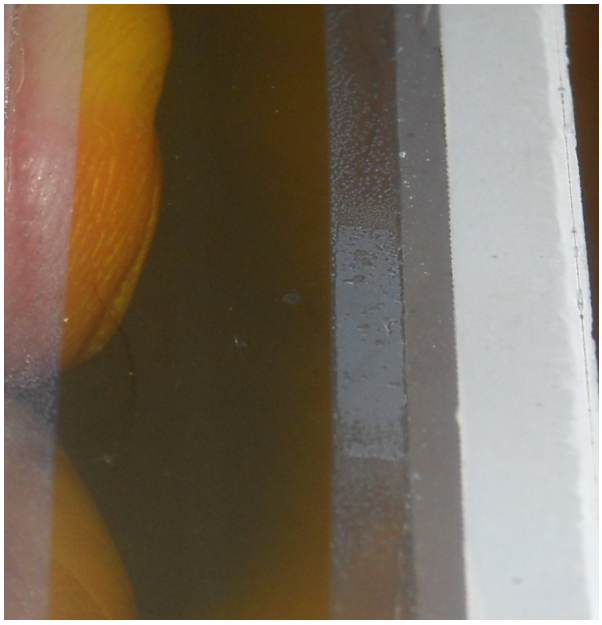

Fig. 30: air bubbles and opaque area on the mail lamination

To resolve this problem another step in the sealing procedure has been introduced: the cold-press

3.3.2 *Hot&cold approach for thermoplastic*

This procedure differs from the one presented in the previous paragraph only in the final part. In fact after the stage of a hot press it was added a stage of a cold-press.
In this manner during the cooling constrains the thermoplastic is obliged to maintain adherence to the two substrates more than what would happen if, such a step, it was performed without the application of external pressure. Generally after the hot-pressed cycle the appearance of thermoplastic band is irregular, in fact it often can be observed the presence of small bubbles or opaque areas. These sealing imperfections disappear after the cold-pressed cycle that obviously has to be run immediately after the hot press. The final appearance of the main lamination as to appear transparent and without air bubbles and/or opaque areas like Fig. 31.

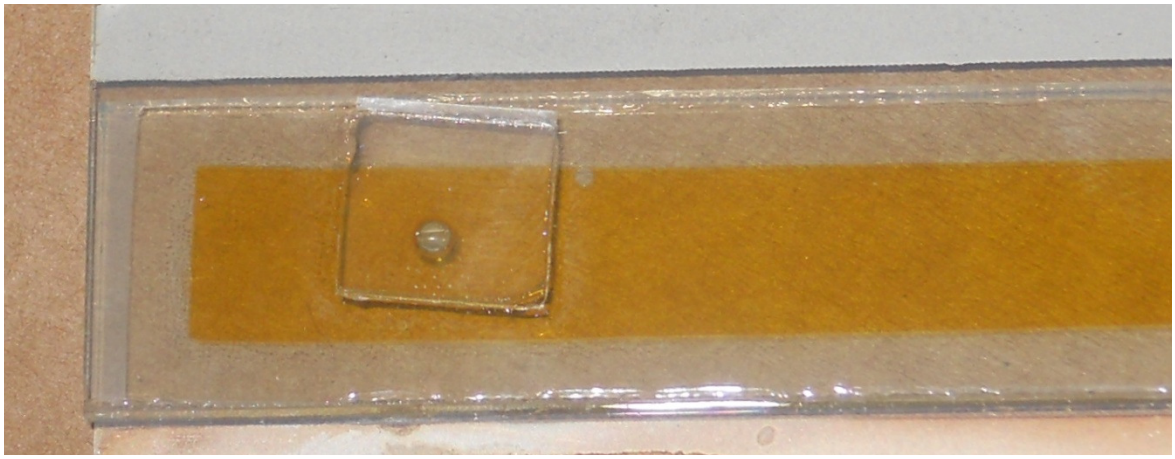

Fig. 31: no air bubbles and/or opaque areas on main lamination

3.3.3 *Differences in performance between hot and hot&cold cycles*

With the introduction of the cold-press step the final quality of the lamination process is significantly improved.

tab. 1: comparison between hot lamination and hot & cold lamination

	Hot press	Hot & cold press
Number of samples	30	30
Number of samples with bubbles and opaque areas	25	10

An encapsulation test was performed to confront the two techniques, 30 devices was sealed with only the hot cycle and other 30 devices with the hot&cold cycle. The incidence of not properly sealed devices is more marked in the only hot cycle case, the results of this test are shown in the tab. 2.

However, the probability of obtaining a correct lamination is still too low. The problem lies in the properties of the material itself, in fact the Bynel, such as Surlyn and many other thermoplastics, is hygroscopic and therefore absorbs a certain percentage of water. Then to further improve the adhesion of a thermoplastic is necessary to perform pre-treatments on the material itself. In the following paragraphs there will be shown the pretreatments adopted to improve Bynel performances differentiating them in pretreatments adopted for the hot and cold stress test.

3.3.4 *Pre-treatment hot stress*

As mentioned in the previous paragraph to obtain a correct lamination of a hygroscopic thermoplastic you must use a pre-treatment. To study what is the best pre-treatment it was performed a preliminary test of lamination with the approach of the hot & cold pressure . In this test the pressing time, the pressure and temperature was kept the same, the only variable parameter was the storage conditions of the Bynel masks used as primary sealer:
The storage period was 1 day long

- Bynel mask storage at the open air;
- Bynel mask storage in a ventilated oven at the temperature of 65°C;
- Bynel mask storage in an active vacuum chamber;
- Bynel mask storage in an active vacuum chamber at 65 °C;

Each sample was subjected progressively to different thermal cycles: 25°C, 45°C, 60°C and 80°C for 3 days each (only the samples that passed the test can be subjected to the following one) to see if pretreatments really improve the adhesion of Bynel. A visual (appearance of bubbles or opaque areas) and mechanical test (hand stress of traction and torsion on external substrates) was performed after each thermal cycle. The results of these test were summarized in the following table (tab. 2):

tab. 2: pretreatments thermal test

pretreatment	Numbers of samples	After 25°C	After 40°C	After 60°C	After 80°C
Open air 25°C	10	■■ 8 ■■ 2	■■ 5 ■■ 1	■■ 2 ■■ 4	■■ 2
Active vacuum chamber	10	■■ 10	■■ 9 ■■ 1	■■ 6 ■■ 3	■■ 1 ■■ 5
65°C	10	■■ 10	■■ 10	■■ 7 ■■ 3	■■ 1 ■■ 6
Active vacuum chamber + 65°C	10	■■ 10	■■ 10	■■ 7 ■■ 3	■■ 1 ■■ 6
		■ air bubbles or opaque areas ■ visual test passed ■ mechanical test passed			

The two pre-treatments, 65 ° C in a ventilated oven and 65°C with active vacuum, are those who have given the best results, but only 10% of the samples passed the test temperature to 80 ° C, this percentage is too low to be acceptable. A more accurate visual inspection found that the root cause of test failure was the appearance of air bubbles in the inner chamber of the solar cell rather than the appearance of opaque areas along the perimeter of the main sealer (a sign of delamination of bynel itself). These bubbles have appeared, in virtually all cases, below the hole of entry of the electrolyte. The sealing of the pinhole with thermoplastic bynel, since from the beginning, was considered the weak point of the structure. The technique used in these tests to seal the pinhole is similar to that used in the main lamination, i.e. the placement of a piece of bynel covered with a glass above the hole and through a first heat press and a subsequent cold one the sealing process is completed. The only major difference lies in the lamination temperature, in fact, to seal the patch we used the press with a only one hot plate (the one in direct contact with the patch) this to not damage or deform the primary sealing.

It was observed that the bubbles appear during the cooling process under the pinhole as it can be seen in Fig. 32

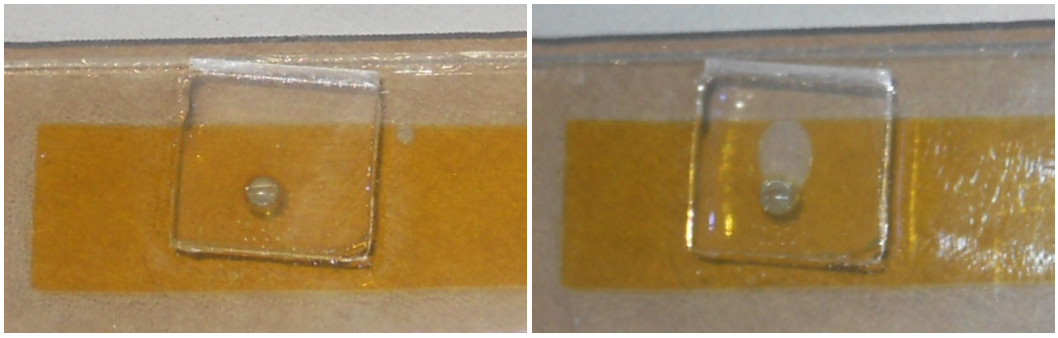

Fig. 32: before and after bubble appearance

Analyzing the EIS measurements of these devices we can see an increase progressively less evident of the diffusion resistance. This probably is due to a reduction of the I_3^- ions concentration in the electrolyte solution, as it can be seen in Fig. 33, in which it is represented the comparison of the Nyquist curves (only diffusion parts) of a device, respectively after a room temperature, a 40 °C, a 60 °C, and a 80°C stress.

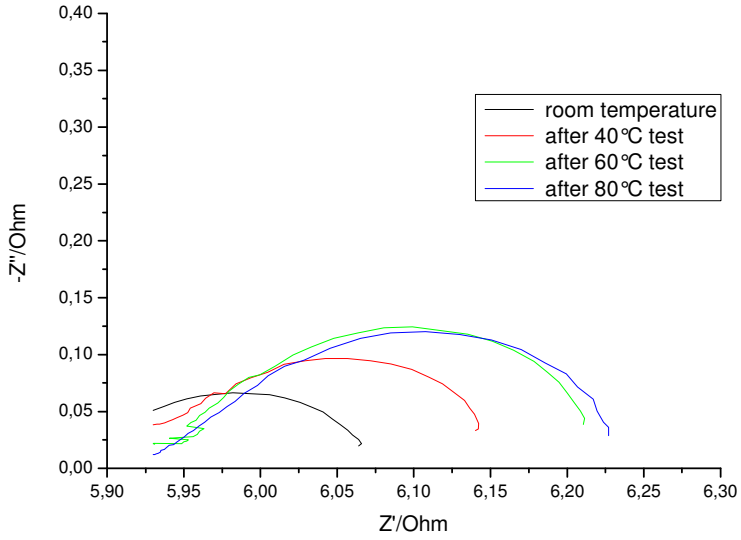

Fig. 33: Comparison of Nyquist curves (only diffusion part)

Whilst considering only the semicircle relative to the counter electrodes what can be seen is instead a decrease of the charge transfer resistance (R_{ct}) with the increase of temperature test, as before progressively less evident (Fig. 34).

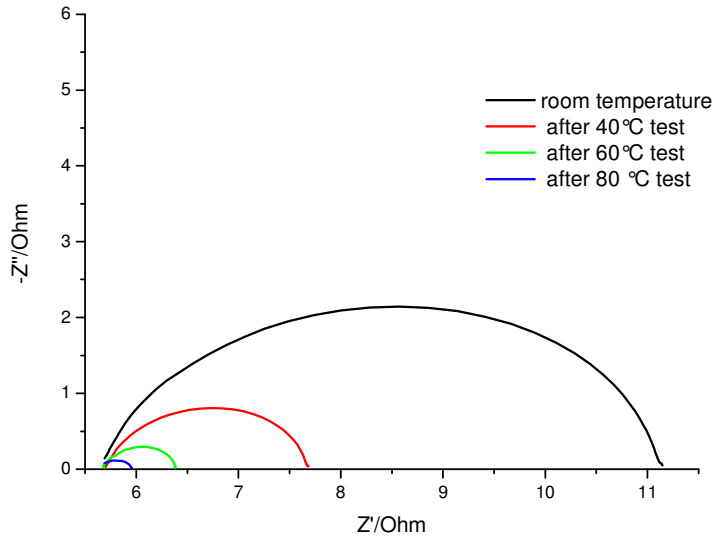

Fig. 34: Comparison of Nyquist curves (only counter electrode part)

Recent experiments seem to improve what has just been said about the role of the patch. In fact observing the device just after the thermal stress at 80°C (still hot) no air bubble are present inside the chamber, whilst during the cooling process small air bubble appear along the main lamination perimeter in the internal chamber.

The pre treatment presented in this paragraph improve the sealing properties of the bynel respect to use it in normal condition, but not enough.

Other test are ongoing to improve furthermore this characteristic like microwave pre treatment (presented below).

3.3.5 *Pre-treatment hot stress microwave approach*

In this paragraph there is presented a different conception of Bynel pre-treatment, the microwave one. In this case the Bynel was put for 30 seconds in a microwave oven at 700 W, than the Bynel masks were used in the main lamination process. Also the Bynel pieces used to seal the pinhole were pre-treated in the same conditions mentioned above. After the first 80 °C 3 days thermal stress only in one device it was notable a partial leakage of the electrolyte trough the main sealer, with a more accurate analyze of this sample it was clear that the leakage of the electrolyte was due to a non accurate cleaning process before the main lamination. In fact there is the presence of dirt under the main sealer just where the electrolyte leaked. The same thermal stress was repeated other two times and also in this case all the devices did

not present any change, no air bubbles appear inside the chamber, apart for two of them that after the third test presented some air bubbles under the pinhole (Tab. 3).

Tab. 3: microwave pretreatment

pretreatment	Numbers of samples	After first 80 °C stress	After second 80 °C stress	After third 80 °C stress
Microwave 700 W for 30 sec	12	■■ 11 ■ 1	■■ 11 ■ 0	■■ 9 ■ 2
		■ air bubbles or opaque areas ■ visual test passed ■ mechanical test passed		

Comparing these results with those obtained by previous pretreatment, microwave treatment ensure a better performance. Since virtually all devices have passed the test at 80 ° C it was decided to perform first a 90°C 3 days test and then a 100 °C 3 days test. After the first test the devices presented any structural modifications, but after the second one the half of the devices presented air bubbles under the pinhole. Summarizing the microwave pretreatment shifts up of 20 °C the temperature limit for observing the onset of structural failure.

3.3.6 *Pre-treatment cold stress*

Until now there were presented only thermal stresses with temperatures higher than 25°C, so to see how Bynel behaves at lower temperature tests at 2°C and at -18°C were performed. In these tests only microwave and hot approach pre-treatments were used. At the end both pre-treatments completely passed the test without any problems, in Tab. 4 it summarized the test.

Tab. 4: Cold stress for microwave and 65°C pre-treatments

pre-treatment	Numbers of samples	2 °C stress	-18 °C stress
Microwave 700 W for 30 sec	6	■■ 6 ■ 0	■■ 6 ■ 0
65°C in a ventilated oven	6	■■ 6 ■ 0	■■ 6 ■ 0
		■ air bubbles or opaque areas ■ visual test passed ■ mechanical test passed	

The EIS analysis shows that after the cold thermal tests the charge transfer resistance of the counter electrode increase. Nothing can be said on the diffusion, apart that it seems to remain quite the same, because its characteristic part in the Nyquist diagram is partially masked from the counter electrode semicircle (Fig. 35).

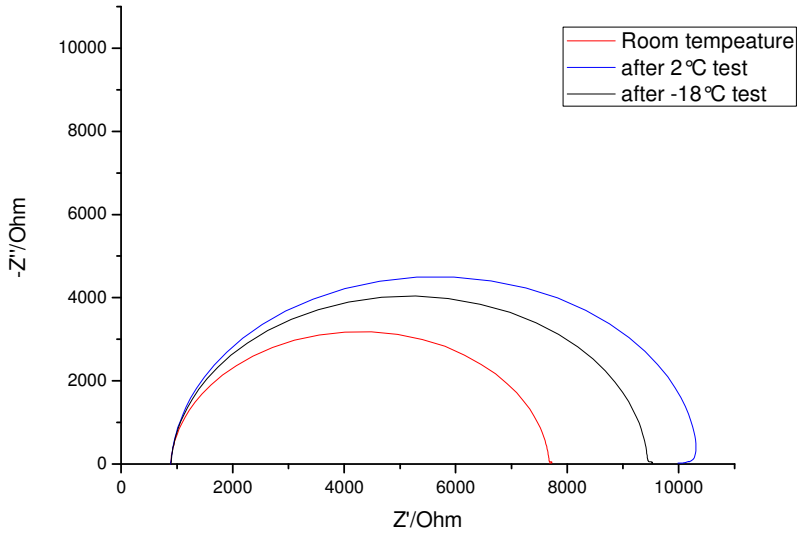

Fig. 35: EIS measurements Nyquist diagram

In the above figure it can be appreciate easily the increasing of the R_{ct} after the cold thermal stresses. It is interesting to observe that going down in temperature the R_{ct} first increase (2°C test) and then decrease (-18°C), it has to say that this phenomena it was observed in the half of the samples analyzed, whilst in the other half it was observed another increase of the R_{ct} after the – 18°C 3 days test (Fig. 36)

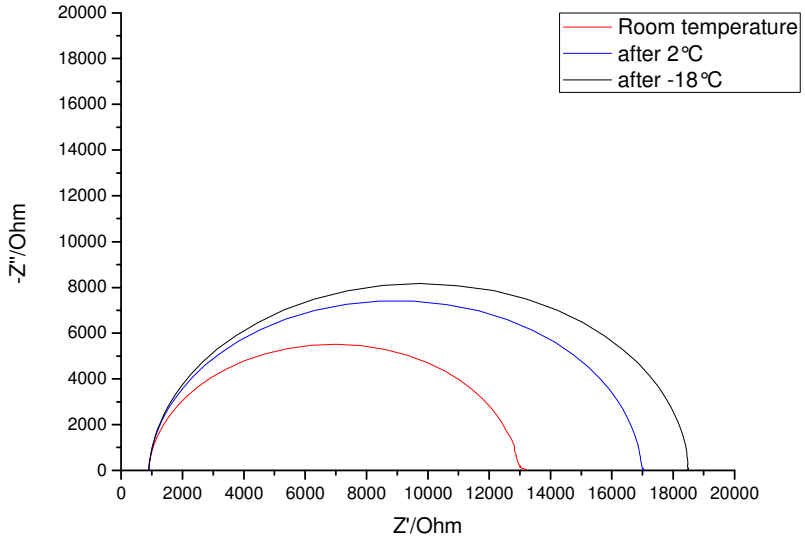

Fig. 36: EIS measurements Nyquist diagram

This R_{ct} increase is reversible, in fact performing, with the same samples, a 80°C 3 days test the R_{ct} decrease considerably, as can be appreciate in Tab. 5.

Tab. 5: Resistances and capacitances of the equivalent circuit of counter electrode semicircle.

	R_{ct} [Ω/cm^2]	C [μF]
Room tempersture	70,16	3,347
After 2°C test	378,9	2,689
After -18°C test	350,4	2,676
After 80°C test	56,28	2,458

3.3.7 *Fluid adhesives dispenser and UV curing*

An alternative to the use of thermoplastic as primary sealing is the use of fluid-sealant. The use of such adhesives can also perform sealing at room temperature in a few seconds or after several hours, depending on the intrinsic properties of the material itself. To obtain a dispensation in the right quantities and especially only in the desired points, the deposition process must be assisted by an automated dispenser (Fig. 37).

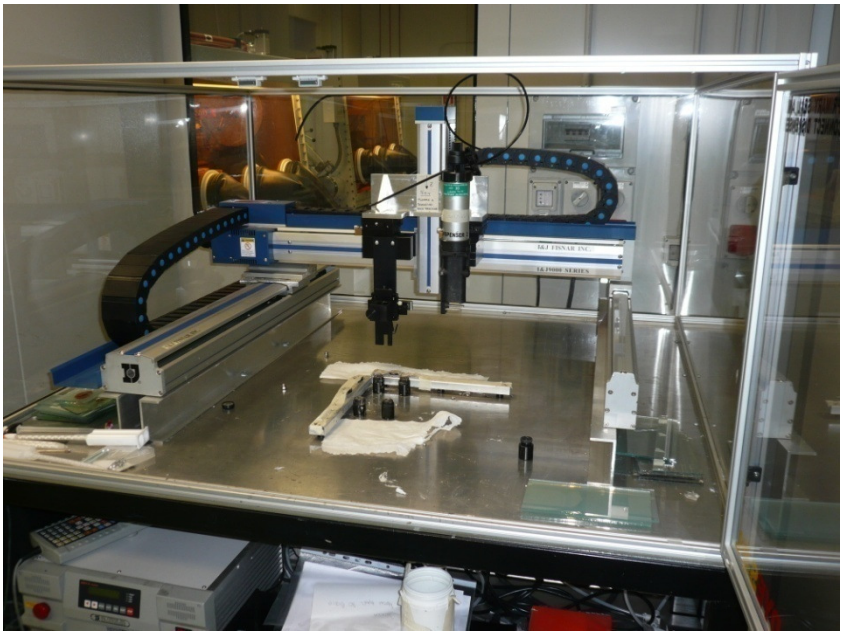

Fig. 37: Automatic sealer applicator

Commercial silicone-based adhesive for DSC technology have been used, but since the preliminary tests at room temperature showed that it is unable to ensure the containment of the electrolyte inside the chamber of the device. This type of adhesive, furthermore, need a thermal treatment at 80 °C for 200 minutes to completely cured.

To perform a sealing within seconds at room temperature imply a considerable saving in terms of time and energy. These features are in great demand in industrial production because they can provide a great safe of money. The use of UV curing resins can provide these features to sealing procedures, different types of these resins were used, but the majority interact with the electrolyte compounds or did not guarantee a perfect adhesion on the used substrates. A commercial UV curing acrylic based epoxy originally designed for electronic use it is applied as primary sealer. In the following paragraphs will be discussed in more detail the use of this UV resin, but first will be shown the effects of UV radiation on the compounds of the DSC solar cell.

3.3.8 *UV degradation*

It is known, that UV-light is a critical degradation factor for DSCs [(73)]. The mechanism of UV-degradation in DSCs is described in detail in [(50)]. Progress has been made in improving UV stability by introducing additives to the electrolyte. Such UV-stabilizing additives, e.g. CaI_2 or MgI_2, dramatically enhance UV-stability [(74)].

However, for outdoor applications an easy and effective option to achieve UV-stability is the application of an UV-filtering polymer foil [(73)]. Clearly then, a long exposure to ultraviolet radiation is undoubtedly damaging to the components of the solar cell. To harden a UV curable adhesive is needed, however, only a few seconds.

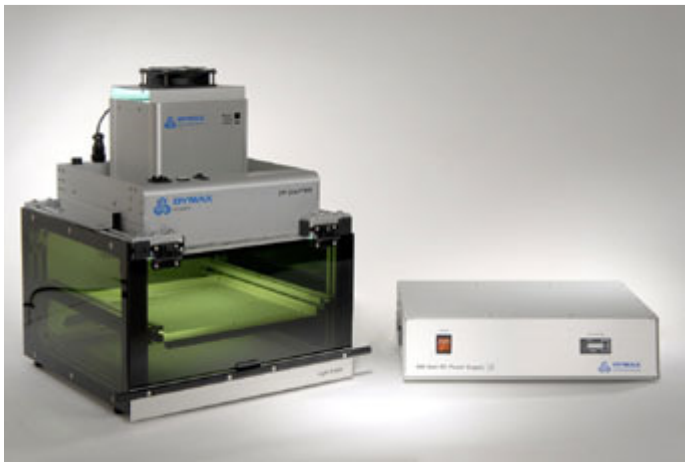

fig. 38: 5000-EC Series UV Curing system

Therefore tests of progressive exposure to ultraviolet radiation (5000-EC Series UV Curing system 250 W/m^2 Dymax fig. 38) of the individual components of the solar cell were carried out to see if brief UV exposure can degrade the materials.

3.3.9 *UV light effects on N3 & N719 Dye*

To see how ultraviolet radiation affects the dye a solution of dye and ethanol in a quartz cuvette was subjected to ultraviolet light in steps of 5 seconds for a total time of 30 seconds. Between each step it was performed a spectrophotometer measurement to observe if or how its own absorption spectrum change after a period of UV illumination. The first dye analyzed was N3 and after 6 steps no changing in its absorption spectra was observed fig. 39.

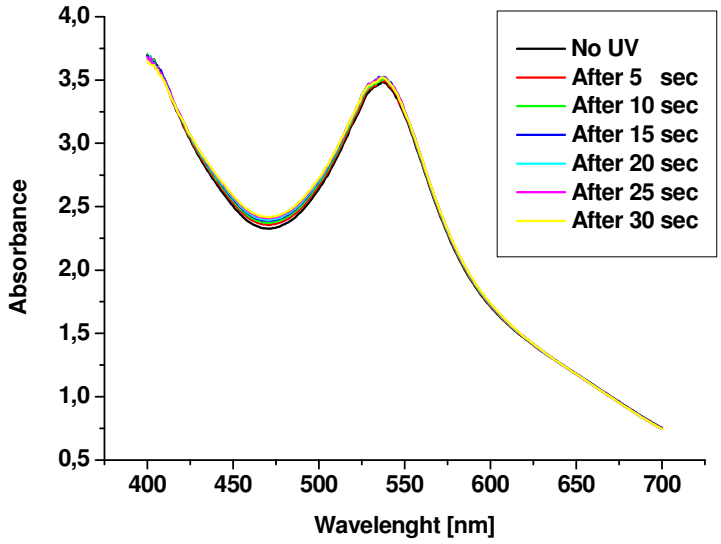

fig. 39: absorption spectra of N3 before and after UV light exposure

The second dye analyzed was N719, also in this materials no changing in absorption spectra was observed as shown in fig. 40

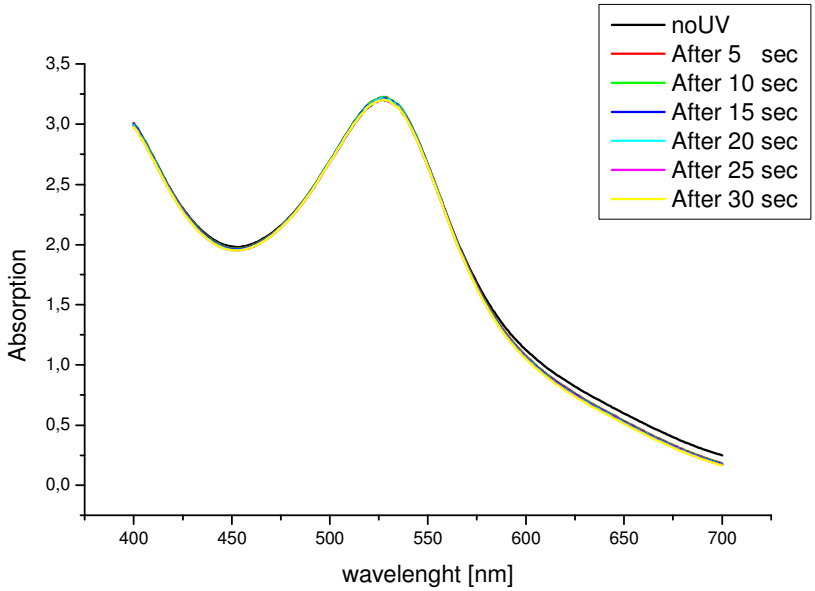

fig. 40: absorption spectra of N719 before and after UV light exposure

The N719 dye solution was also tested under a continuous 30 seconds strong UV light radiation (250 mW/cm^2), the spectrophotometer measurement was performed in wider spectra region from 200 nm to 800 nm also if common sodalime substrates have a 320 nm cutoff . Also after this 30 seconds exposure no changing has observed as it is shown in fig. 41.

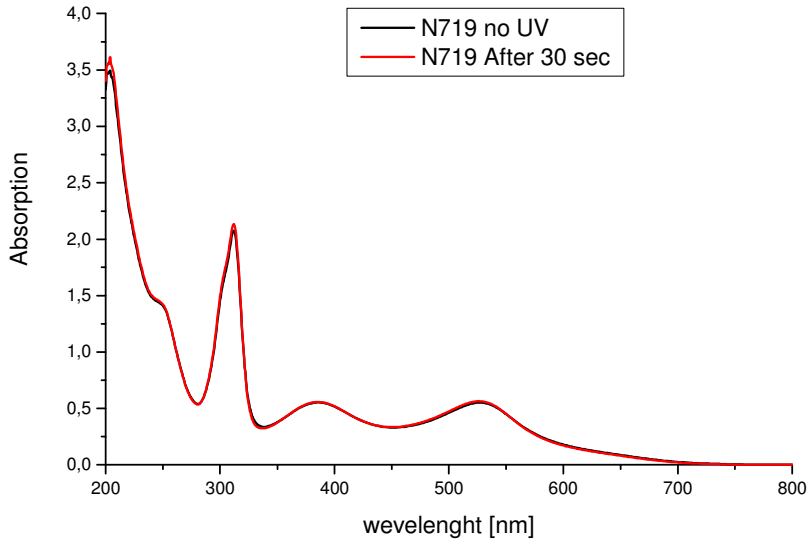

fig. 41: absorption spectra of N719 before and after continuous strong 30 seconds UV light exposure

As shown before a short exposure to UV radiation < 30 seconds does not produce any changing in absorption spectra of N3 and N719 dyes. This make these dyes suitable to be used in a DSC cells sealed with a UV curing adhesives.

3.3.10 *UV light effects on the electrolyte*

A similar analysis to that performed in the previous paragraph, for organic dyes, was performed on the electrolytic solution. Exposure to UV was respectively of 15 and 45 sec. As before, at each step it was measured the absorption spectrum of the material using a spectrophotometer. A change in patterns of this spectrum indicates that the UV light, even for a time so limited, interact with the material in question. Due to the high degree of absorption of the electrolyte, to perform such a measure, it had to dilute the solution with a ratio of 1 to 10 with its solvent base (specifically the metoxypropionitrile MPN). The chamber containing the liquid electrolyte was made using the same substrates and thicknesses used for the construction of test cells:

- Substrates: 3mm thick borosilicate with FTO 8 ohm/square.
- about 40 microns for the thickness for the internal chamber.

Analyzing the absorption spectrum before and after UV treatment, it can be seen (fig. 42) that for such a limited exposure the electrolyte solution does not be damaged.

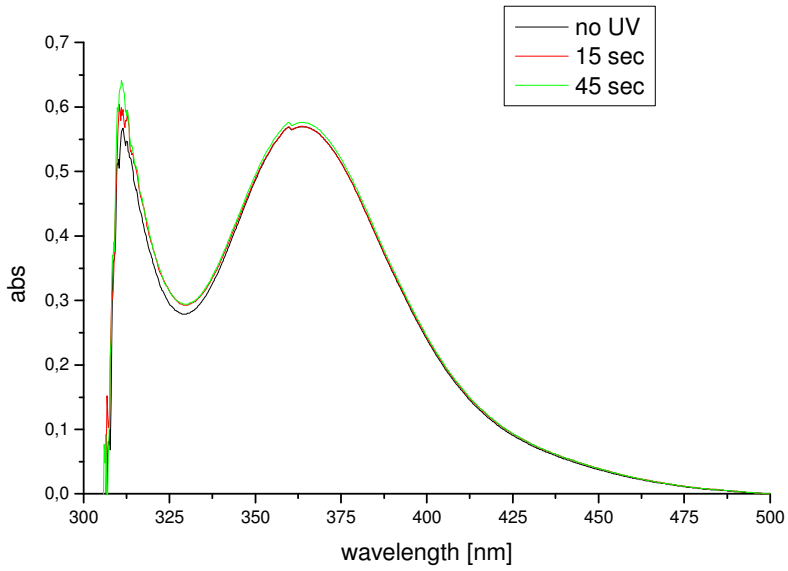

fig. 42: absorption spectra of a iodine/triodine electrolyte solution in MPN before and after UV treatment

Based on these results we can say that an electrolytic solution based on a redox couple iodide/triodide in MPN can be used in a process that also involve the use of UV curable resins.

3.3.11 *UV light effects on the titanium paste*

UV degradation test was performed also on titanium paste, in particular a tin layer of titanium paste (dyesol) was deposited by screen printing to obtain a thickness of about (8 µm) on a borosilicate substrate. The absorption spectrum of this sample was measured before and after an exposure of 30 seconds of continuous strong UV radiation. results can be observed in (Fig. 43). Also in this case the exposure to UV, for such so limited time, do not damage the titanium component of the solar cell.

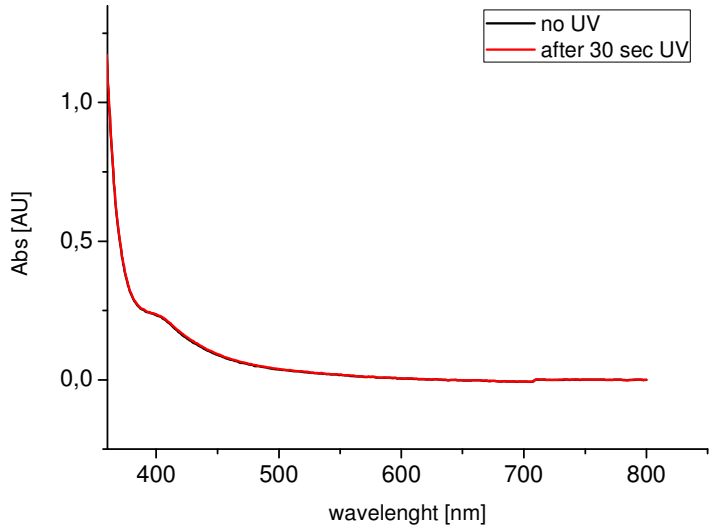

Fig. 43: TiO_2 Absorption spectra before and after 30 seconds strong UV light exposure

The inferior limit of the absorption spectra measurement has been fixed at 360 nm because it is the glass substrate wavelength cut off.

3.3.12 *UV light effects on a sensitized titanium film*

To complete the analysis of the effect of ultraviolet radiation on the components of the DSC solar cell for short-term exposure, we now analyze the effect of UV on a titanium film, similar to the one presented in the previous paragraph, but this time sensitized by the use of N719 Dye. Also in this case the absorption spectra was measured before and after an exposure of 30 seconds of strong UV light (Fig. 44).

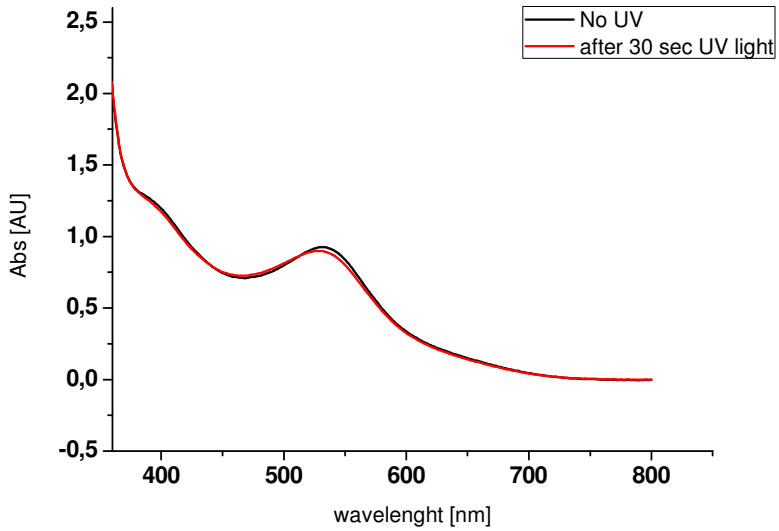

Fig. 44: TiO_2 sensitized absorption spectra before and after 30 seconds of strong UV exposure

As it can be seen from the previous figure no appreciable change in the absorption spectrum of the sensitized titanium film is detectable.

Longer exposure to strong UV radiation can therefore damage the organic molecules as it can be observed in Fig. 45, in this figure is shone the absorption spectra of a sensitized TiO_2 layer before and after 10 minutes of strong UV exposure.

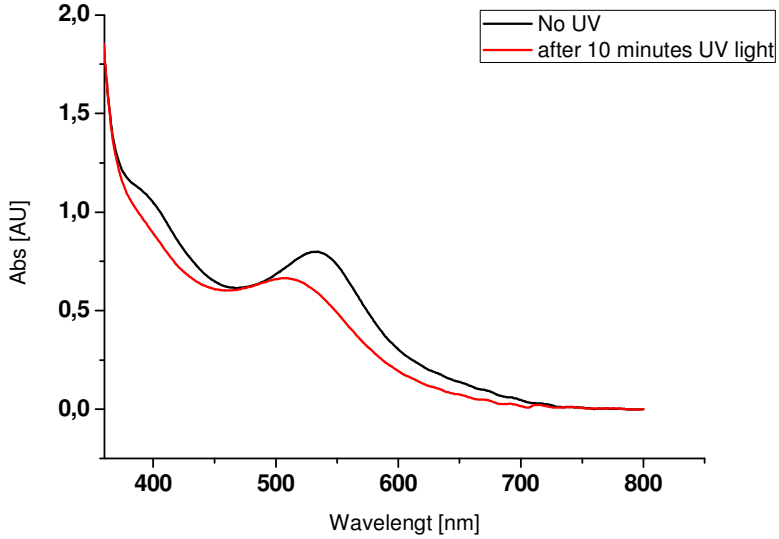

Fig. 45: Sensitized TiO_2 absorption spectra before and after 10 minutes of strong UV exposure

The temperature of the UV chamber at the end of the 10 minutes measurement was about 95°C. So in order to understand if the blue shift shone in Fig. 45 is due or not to a thermal degradation of the N719 Dye, the absorption spectra of a similar sample was taken before and after a thermal stress (100°C) for 10 minutes in the dark. The result

is shone in Fig. 46. No appreciable change was revealed, so the blue shift shone in Fig. 45 can be achieved only to the interaction between the UV radiation and the Dye molecules.

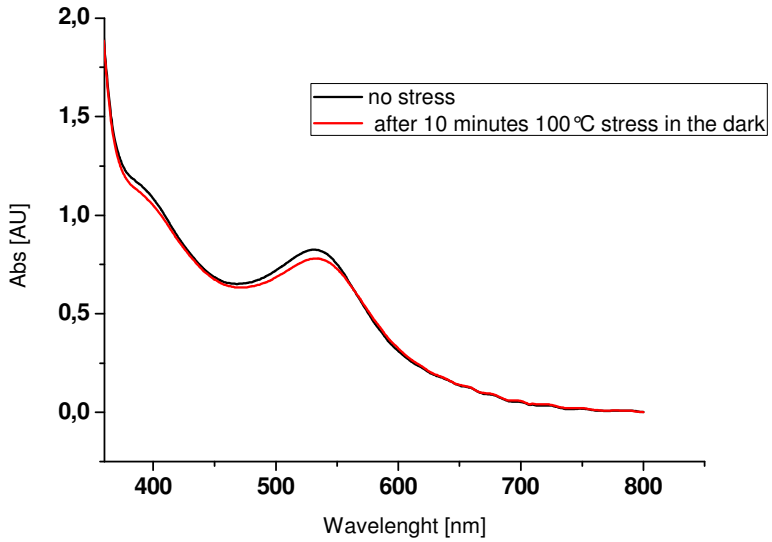

Fig. 46: Sensitized TiO_2 absorption spectra before and after a 100°C thermal stress in the dark

Therefore, based on the results obtained and shown in the previous sections we can state that the use of UV curable resin in the building process of the DSC cell is compatible with the constituting elements of the cell (in terms of the addition of the UV component used in the resin curing process). The use of UV curable resins permit to achieve a very fast room temperature sealing process very important in the optics of an industrialization. The main problem of this approach is the interaction between the resin and the electrolyte.

3.3.13 *Interaction among UV resin and cell constituents*

The problem to use UV resins as primary sealer is undoubtedly their possible interaction with the solar cell components, especially with the electrolyte. For this reason the use of such materials must be selective, in the sense that it has to be chosen materials that once cured are inert towards the electrolyte.

Some kinds of UV resins show a strong interaction with the electrolyte, some of them, though keeping their cohesion but not hermetic characteristics , damage one or more

electrolyte compounds, for example causing the reduction of concentration of I_3^- ions and/or with the onset of crystallization in the liquid electrolyte itself (Fig. 47) .

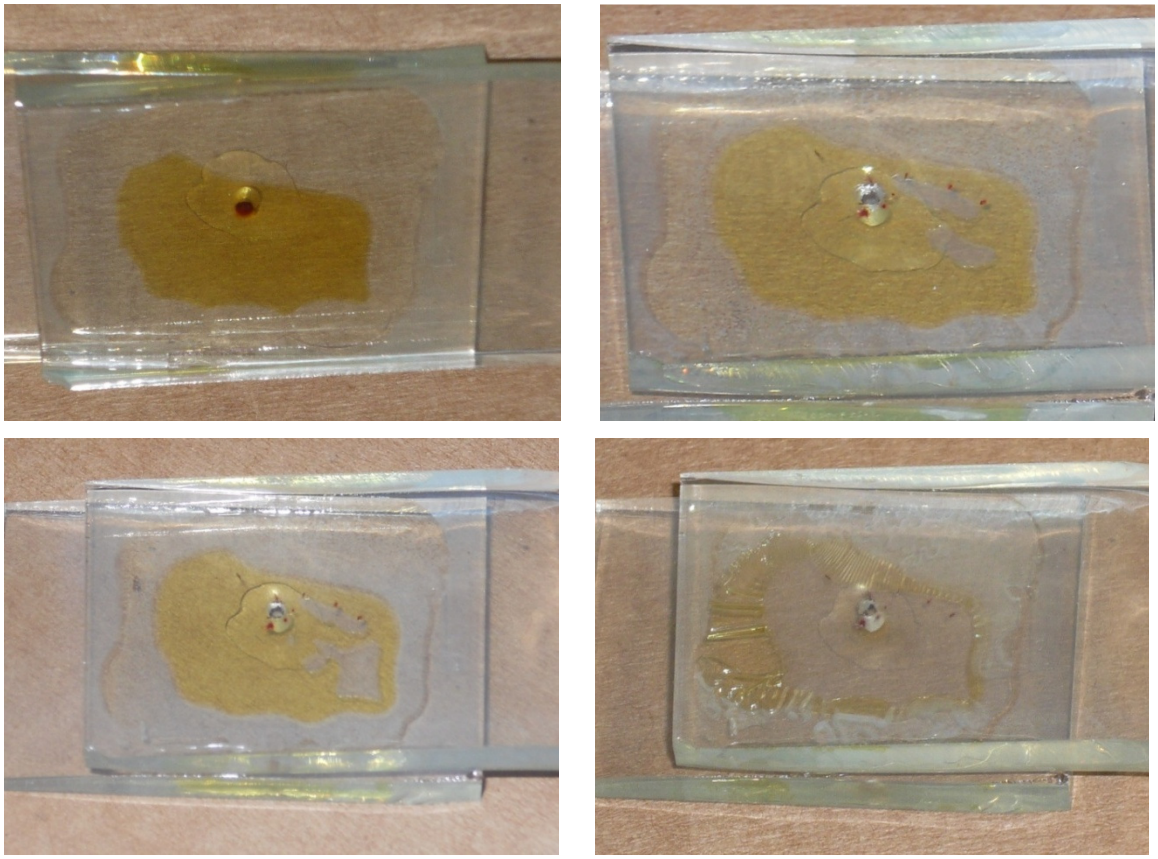

Fig. 47: device sealed with Vitralit respectively at the beginning, after 10 h, after 24 h, after 35 h

Others resins are attacked from the compounds of the electrolyte and more or less rapidly change their chemical-physics properties loosing their cohesion characteristics letting the electrolyte leakage from the inner chamber.
Others, instead, seems not to interact with the electrolyte keeping well sealed the device like 3022 special UV epoxy (Dymax).

3.3.14 *Dymax 3022 special UV epoxy*

Light curing plastic bonding adhesives cure in seconds upon exposure to ultraviolet light and visible light, even through UV-blocked plastics. These solvent-free, worker-friendly plastic adhesives from DYMAX form high-strength, environmentally resistant bonds to plastics and other substrates, including polycarbonate, PVC, phenolic, acrylic, metal, glass, and ceramic. Because DYMAX plastic adhesives bond

so many different substrates, they are exceptional adhesives for bonding dissimilar materials, something that cannot be done with traditional welding methods and other types of adhesives.

The use of this UV resins as primary sealer gave good results. 3022 UV resin was mixed with microspheres of silica for gas-chromatography with a diameter of 40 µm in order to fix the high of the internal chamber. By the use of an automatic dispenser to deposit 3022 resin, presented previously, they were realized several structures FTO-electrolyte-FTO, after more than 9 months of room temperature storage the devices are still in the same conditions of the beginning. To confront the goodness of 3022 as sealer in the same period we realized others FTO-electrolyte-FTO structures sealed this time with commercial silicon for DSC (natural assembly polymer 2 parts, Dyesol) . In this case progressively always more air appear inside the internal chamber (Fig. 48: Substrates sealed with Dymax 3022 (left) and with commercial silicon for DSC (right)).

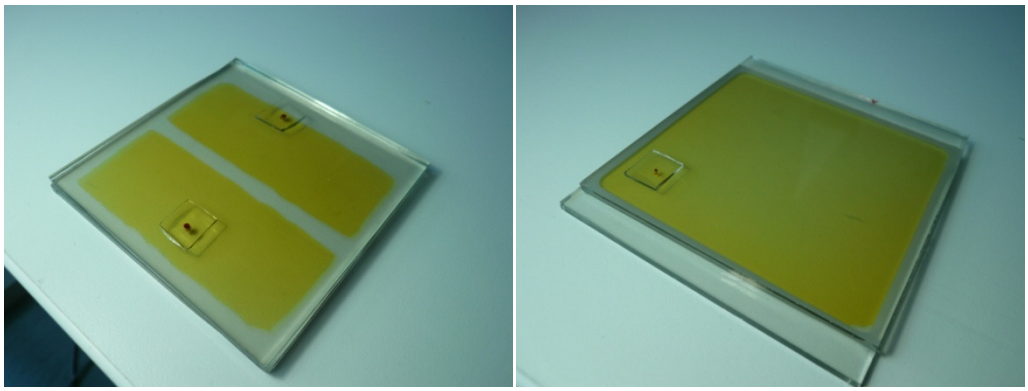

Fig. 48: Substrates sealed with Dymax 3022 (left) and with commercial silicon for DSC (right) [beginning]

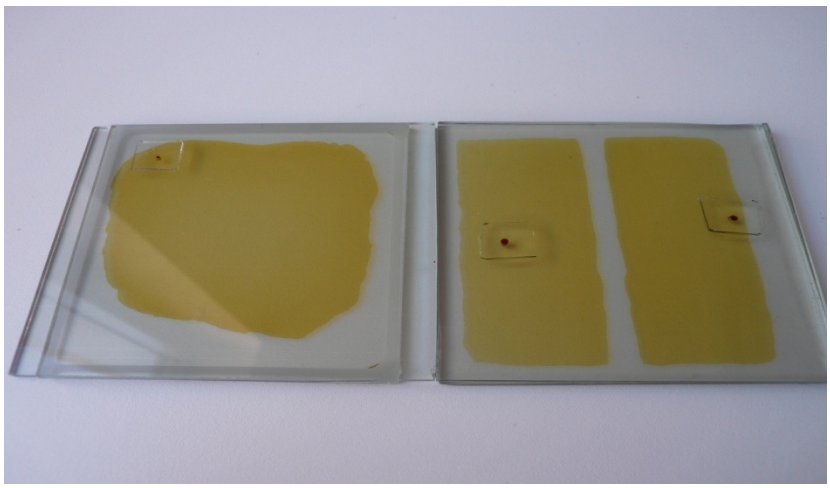

Fig. 49: after 3 months at room temperature

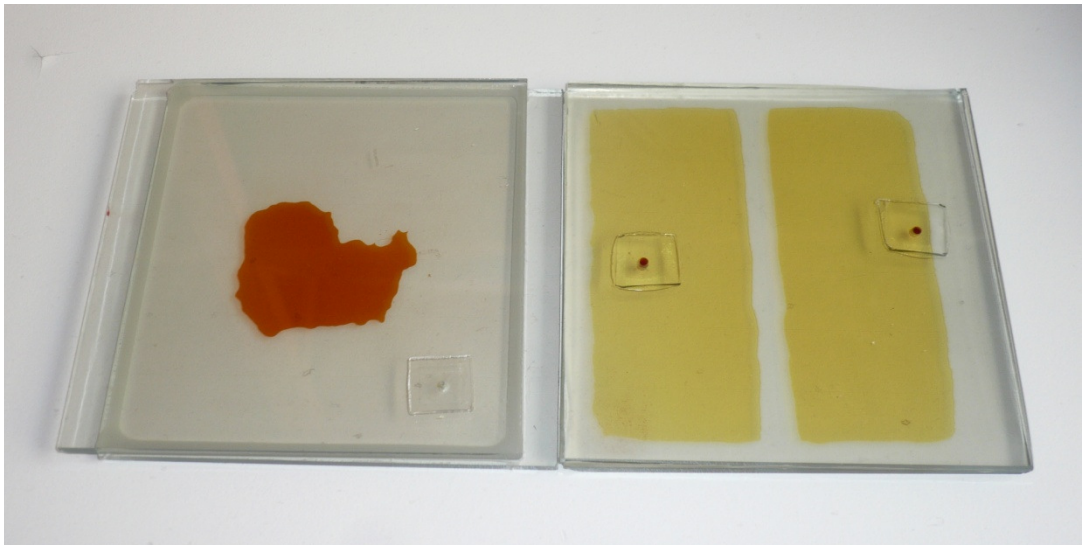

Fig. 50: after 10 months at room temperature

Thus, 3022 UV resin seems to be a good sealer for DSC, but this only at room temperature. In fact if the device is thermally stressed at more than 50°C the temperature catalyzes chemical interaction between the resin and the electrolyte, interactions that at room temperature does not happen. The results is a sort of crystallization of the cured UV resin leading to a delamination of the device as it can be seen in Fig. 51.

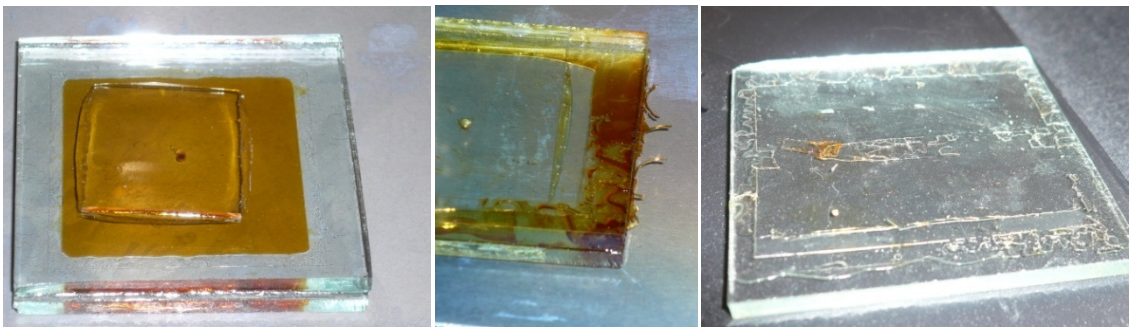

Fig. 51: Before thermal treatment (left) and after thermal treatment (center and right)

These test shows that UV resins like Dymax 3022 cannot be used as they are in DSC technologies as primary sealer, but starting from this kind of materials, for example modifying the base molecule, it can achieve a stronger resistance towards the attack of the electrolyte also a higher temperature.

3.4 Summary table

In this paragraph there will be summarized the sealing activity of this work showing in a table (Tab. 6) the principal chemical families of sealants tested and the results of their experimentations in terms of cohesion to substrates, visible interaction with cell compounds and capacitance to not let leakage the electrolyte. It has to be noticed that from each material family comes decades and decades of different products differentiating from each other in the greatest part by only some additives. A lot of commercial products coming from the same families there were tested, but by sure not all. The trend that comes out from this analysis was that if a product seems to be good for an application, also the others, coming from the same chemical family, present good feedback from their applications.

Tab. 6: Summary of all the resins/adhesives chemical families tested

	Composition If known	Type of sealant	Cohesion to substrate	interaction	Electrolyte Leakage
Bynel® DuPont	LLDPE	thermoplastic	Good	No	> 90 °C
Surlyn® DuPont	Ethilene & polyetilene	thermoplastic	Good	No	> 60 °C
Temobond 3M	Polyester	thermoplastic	Sufficient	No	Room temperature
Hyflon ®	Semi-crystalline Perfluoropolymers	Resin	Good	No	Room temperature
LJF pr 1782	polysuphide	resin	Good	yes	Room temperature
Loctite Super Attack	cyanoacrylate	adhesive	Good	yes	Room temperature
Super colla saratoga	cyanoacrylate	adhesive	Good	yes	Room temperature
Acciaio liquid PATTEX	bisfenolo-A-epicloridrina	Two component epoxy	Good	yes	Room temperature
Salda rapido BOSTIK		Two component epoxy	Good	yes	Room temperature

Vitralit ® 9140 VL PANACOL	Urethane	UV & light curing adhesivs	Good	yes	Room temperature
Multilink® automix IVOCLAR VIVADENT	dimethacrylate and HEMA	UV & light adhesives	Good	> 45°C	Room temperature
Enamel plus Hfo MICERIUM	BisGMA 1,4, Butandioldimethacrylat	UV & light adhesives	Poor	yes	Room temperature
GC Gradia Direct	Urethane Dimethacrylate (UDMA)	UV & light adhesives	Sufficient	yes	Room temperature
Silicone universal BOSTIC	Acetic Silicone	silicone	Good	no	Room temperature
Natural assembly polimer DYESOL		Two part silicone	Good	no	Room temperature
3022 DYMAX	Urethane Acrylate - epoxy	UV & light curable resin	Good	> 55°C	> 55°C

952 DYEMAX	Urethane (Meth) Acrylate	UV & light curable resin	Good	> 55°C	Room temperature
Uhu exstra		Adhesives	Good	yes	Room temperature
9482 3M	Rigid acrylic	Adhesive tape	Good	yes	Room temperature
VHB™ 9460 3M	Extra rigid Acrylic	Adhesive tape	Good	yes	Room temperature
Adesivo plastic trasparente BOSTIK	vinyl	adhesive	Poor	yes	Room temperature
Sista PU 198 Henkel	polyuretanic	Adhesive	Good	yes	Room temperature

4. Long term stability

For all solar cell technologies long term stability is a basic requirement. Especially for building integrated applications, long term stability must be warranted for at least 20 years. The product certification for solar modules is based on international standards from the series IEC 68 “Environmental Test Procedures”. A different standard exists for crystalline silicon solar modules (IEC 61215) and thin film solar modules (IEC 61646). The IEC qualification testing includes a number of tests, from hot-spot endurance over mechanical load test to hail endurance. Other test are the heat test under 85 °C in the dark, continuous strong light soaking and UV stability. After each test, the degradation of maximum power at standard testing conditions should not exceed 5 %.

Especially for large area DSC modules, stability is related to hermetic sealing. The sealing material must be mechanically and thermally stable and be chemically inert against the I^- / I_3^- redox couple. The sealing material must protect eventual conductor rid and prevent mass transport between the electrolytes of neighbouring cells. Intrinsic stability of the DSC can only be studied if the extrinsic stability (the encapsulation) is assured. Intrinsic long term stability tests are performed on small test cells (A = 2.5 cm²). As electrolyte a commercial iodine/triiodine redox couple electrolyte (Dyesol HSE) are used. The accelerated ageing tests include continuous strong light soaking (0,8 sun) at room temperature (25°C) without UV filtering. Stability in the range pre-fixed was achieved, but a very complex degradation behavior were observed.

Several studies were presented on DSC long term stability by several authors like Naohiko Kato at all. or Michael Grätzel [(75), (76)].

In the following paragraphs will be presented a work done with the intent to understand whether or not there is a transient before getting a stabilizing in performance of the DSC device.

4.1 2000 hours test

A 2000 h test was performed to observe three parameters:

- how the DSC devices behave over time under certain conditions.
- if the deterioration in performance remains in an acceptable range (-20% in efficiency).
- if there is or not a transient before the stabilization in performance.

To verify the tasks and observe the dynamics, both internal and external, the devices were subjected to different types of stress, in particular light and working-light stress. The dynamics of these devices, therefore, were analyzed by the observation of the characteristic electrical parameters , namely: current density at short circuit and at maximum power point, voltage at open circuit and at maximum power point, maximum power point photogenerated, fill factor and efficiency (Jsc, Jmax, Voc, Vmax, Pmax, FF and ŋ). These observations were made by scanning current-voltage curve (IV), power-voltage curve (PV) both under light soaker and under sun simulator, while electronic impedance spectroscopy (EIS) was carried out only under sun simulator. All testing was performed at constant temperature with a tolerance varies according to the light source used. To perform these measurements were used both specific homemade setup and commercial setup.

4.1.1 *Light sources*

During this test we have used two different light sources depending on whether the aim was light aging or the detection of the reference electrical parameters. This differentiation has occurred because the lamps that are closest to the solar spectrum have lifetimes (about 750 hours) much shorter than others (ie 5000 hours) which, however, deviate slightly more from the solar spectrum (fig. 52).

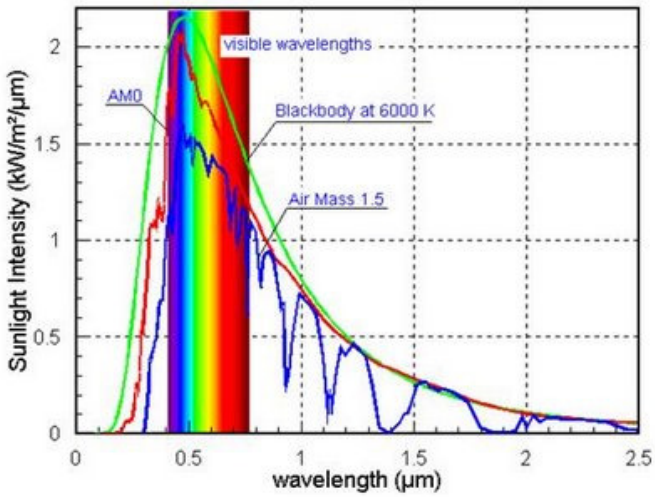

fig. 52: solar spectrum

The type of lamp used for the aging test was a light soaker chamber (LSC) Dyesol Class C equipped with a metal halogen lamp Mercury vapor 1000W with the following spectrum (fig. 53).

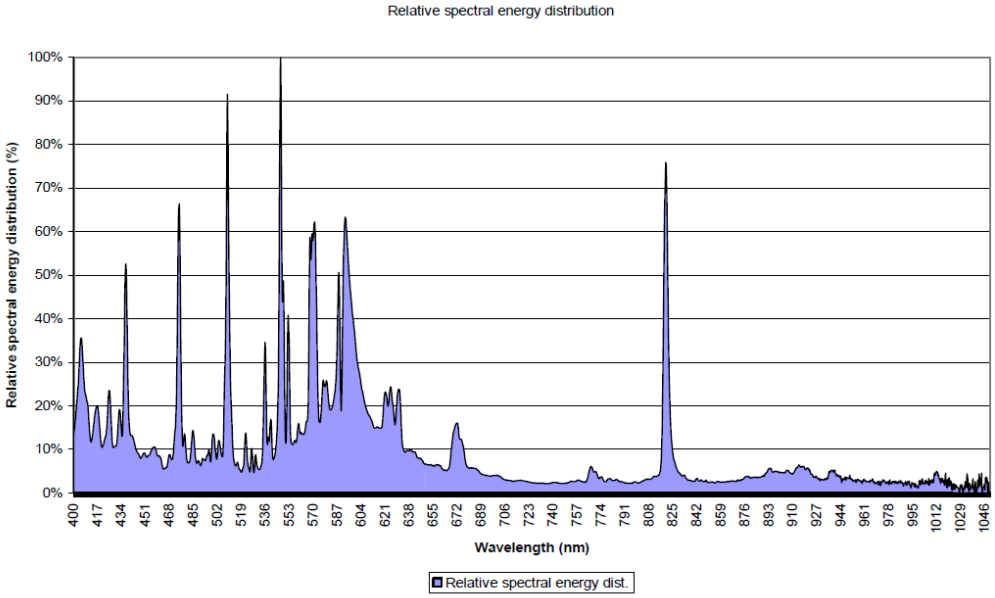

fig. 53:metal halogen lamp spectrum

while the type of lamp used during the measurements to obtain the electrical parameters of control is a sun simulator KHS Class B equipped with a xenon lamp fig. 54 (Ushio Xenon short arc lamp UXL 553)

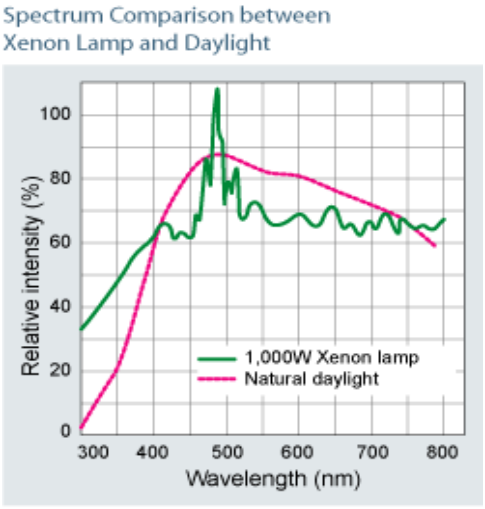

fig. 54: xenon arc and daylight spectrum

In fig. 55 it is shown the comparison between the spectra of the two light sources used.

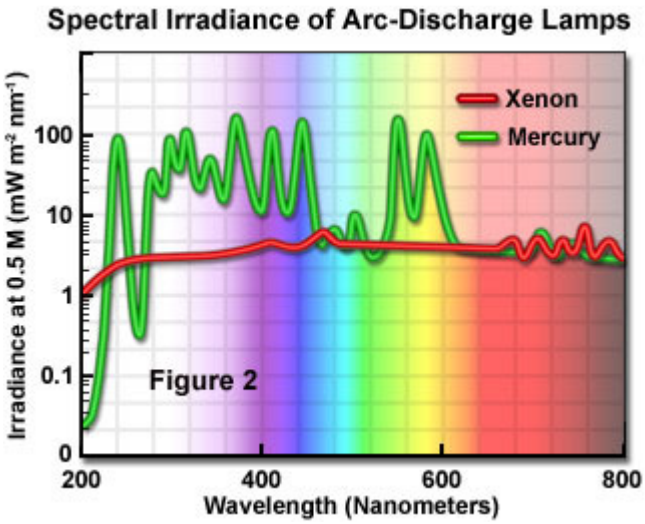

fig. 55 xenon and metal halide lamp spectrum

4.1.2 *Acquisition setup*

Depending on the type of acquisition performed it was used a dedicated measurement system

• For IV and PV reference measurements it was used an Agilent E5262A

• EIS measures were performed employing an AUTOLAB

• The program that manages the IV, PV and soaking measures is in LabVIEW with specific configurations depending on the type of measure. For EIS measurement it was used dedicated commercial program.

• The acquisition of light soaking measures was performed using a dedicated acquisition system developed by us.

4.1.3 *Temperature control system*

The temperature control of the device under test is ensured through the use of Peltier cells integrated on a thermal-well water cooled controlled by power supplier with a digital output. The temperatures of the devices are detected by K-type thermocouples simultaneously with the detection of the maximum power points during the light soaking process, while they are detected manually, by the use of a FLUKE, during the recording of reference electrical parameters and EIS parameters under sun simulator. In fig. 56 it is shone the schematic upper view of the described system.

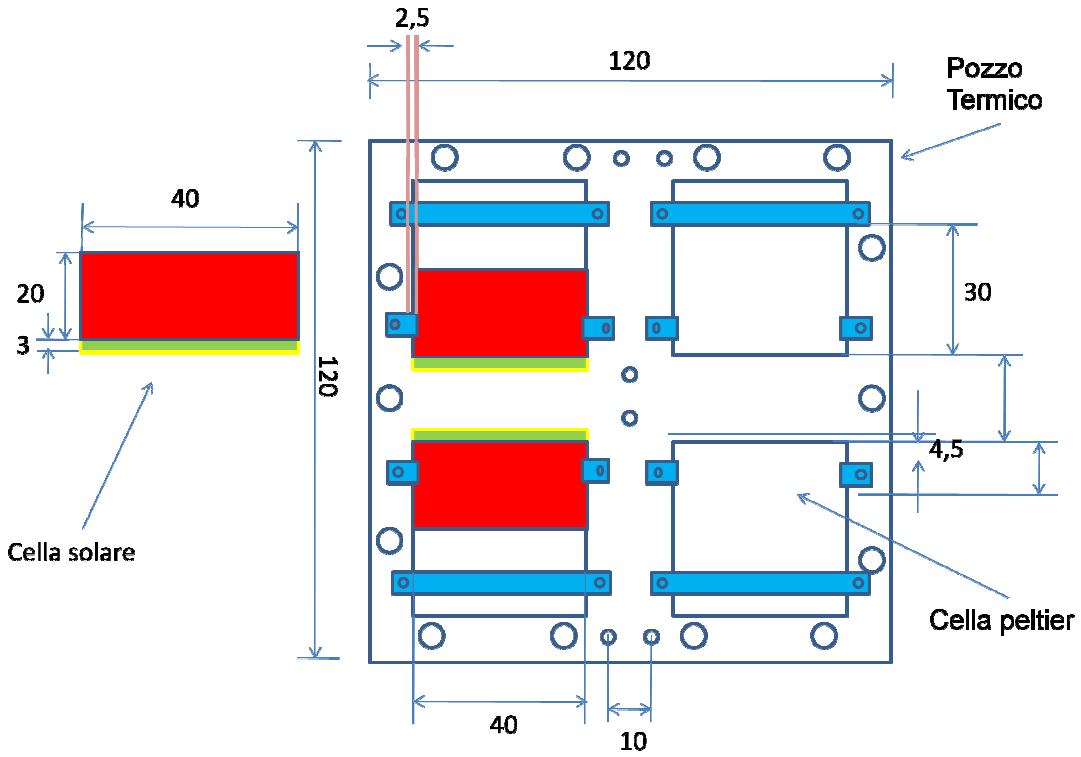

fig. 56: schematic view of the temperature control setup

whilst in Fig. 57 it can be seen the prototype realized in anodized aluminum.

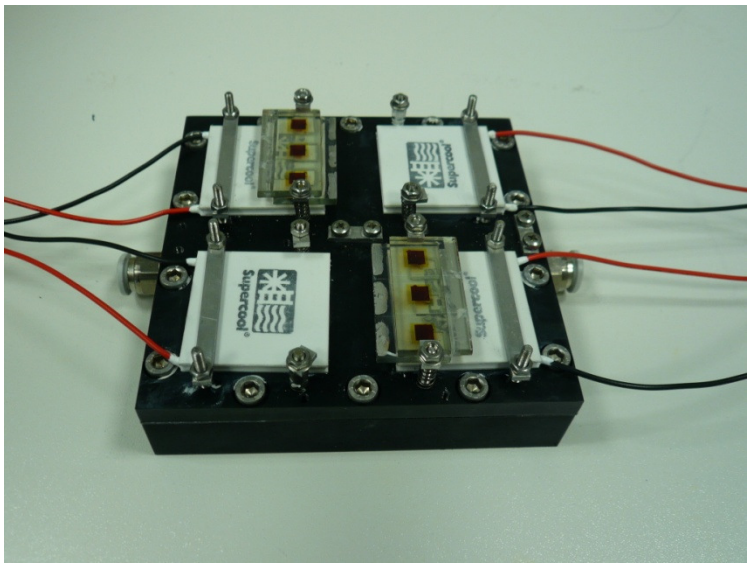

Fig. 57: temperature control system

4.2 Devices

The devices used for this test were made as follows:

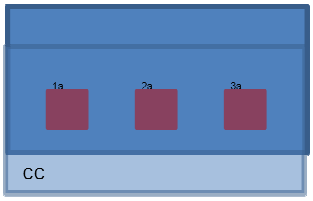

Fig. 58: Device layout with identification codes (CC) and active areas (1st 2nd 3rd) location

Single device dimension is 4 cm X 2 cm X 0,6 cm.

On every devices there are three active areas of 0,5 cm X 0,5 cm.

4.2.1 Construction method and materials

4 devices were realized, equals in pairs, differing only for the primary sealing, the identification codes are the follows:

1. Q_4 and S_8
2. R_3 and S_4

The identification code is on the outside of the photoelectrode, the individual areas are progressively named as follows: 1^{st} - 2^{nd} -3^{rd} starting from the nearest identification code (Fig. 58).

The photoelectrodes were realized with 18NRT Dyesol deposited by screen printing, the average thickness of each active areas are the follows:

- Q_4
  - 1_a 15 µm
  - 2_a 14 µm
  - 3_a 15,5 µm
- S_8
  - 1_a 14,5 µm
  - 2_a 15,5 µm
  - 3_a 16 µm
- R_3
  - 1_a 15 µm
  - 2_a 14,5 µm
  - 3_a 14,5 µm

- S_4
  - 1_a 14,5 µm
  - 2_a 14,5 µm
  - 3_a 14 µm

The active areas profiles are shown below: 1st 2nd and 3rd respectively:

Q_4

S_8

R_3

S_4

- Sensitization process: Dyesol N719 0.05 M in 100 ml of pure ethanol, dipping time 24 hours.

- Electrolyte: Dyesol HSE inserted through injection chamber with vacuum assisted system.
- Counter electrode: Dyesol PT1 deposited by screen printer.
- Substrates: TEK 8 Pilkinton FTO.
- Sealant: Q4 and S8 surlyn 60 μm solaronix pressed to 0.5 atm at 90 ° C for 45 sec, S4 and R3 Bynel 50 μm Dyesol pressed to 0.3 atm at 150 ° C for 35 sec.
- Secondary sealer DYMAX 3022 U.V. curable.
- Hot approach sealing procedure (see pag 58)

4.3 Measurements

To characterize the devices there were performed the following types of measures:

- During the period of light soaking the second active area of each device is forced to work to the maximum power point (Work-light stress), recalculated periodically. While the first and third active area are left at their open circuit voltage (only light stress)
- IV and PV curves made under sun simulator (1 sun Class B) at intervals of about 20 days at 25 ° C ± 0.5 ° C, this is to observe how these parameters change after a light stress and work-light stress.
- EIS measurements performed at intervals of about 20 days at 25 ° C ± 0.5 ° C. To see how the internal dynamics varies after the application of continued work-light and only light stress. This type of measurement is performed under sun simulator.
- IV and PV characteristics every 45 minutes during the light soaking retaining only for the active areas aged at P_{max}. This is to observe how the characteristic electrical parameters (J_{sc}, V_{oc}, J_{max}, V_{max}, P_{max}, FF and ŋ) vary over time while the device is subjected to stress as described above. Such measures are carried out directly under light soaker with an incident power of 0.8 sun and at 25 ° C ± 1.5 ° C.

4.4 Data acquisition under light soaker and sun simulator

Regarding the test under light soaker the acquisitions of electrical parameters were made via a homemade hardware and customize software. In this way we had the possibility to observe the degradation process continuously without having to interrupt the stress applied to perform the acquisition of the characteristic electrical parameters. The reliability of this system was tested by comparing same measurements with a commercial setup. Instead, the reference measurements were carried out under solar simulator and the data acquisitions were obtained by a commercial setup, so during these measurements the sample was moved from the light soaker to the sun simulator.

4.5 P_{max} and V_{oc} ageing test analysis

In the following paragraphs there were presented the analysis of a cell aged under light soaker at room temperature (25°C ± 1.5 °C) at its own maximum power point (periodically recalculated) and at V_{oc}. The other cells aged under the same conditions present an analogous trend.

4.5.1 Device Q_4 cell 2_a aged under P_{max}

The active area was aged under light with a incident power of 800 W/m^2, AM 1.5 and with a constant temperature of 25 ° C ± 1.5 ° C. For the time between a detection of the IV/PV curve and its subsequent the cell worked at its own maximum power point, recalculated periodically. From data it was observed that the efficiency degradation of the solar cell in question was approximately of the 20% respect to the initial value. Fig. 59 shows the trend of the efficiency with readings every 24 hours.

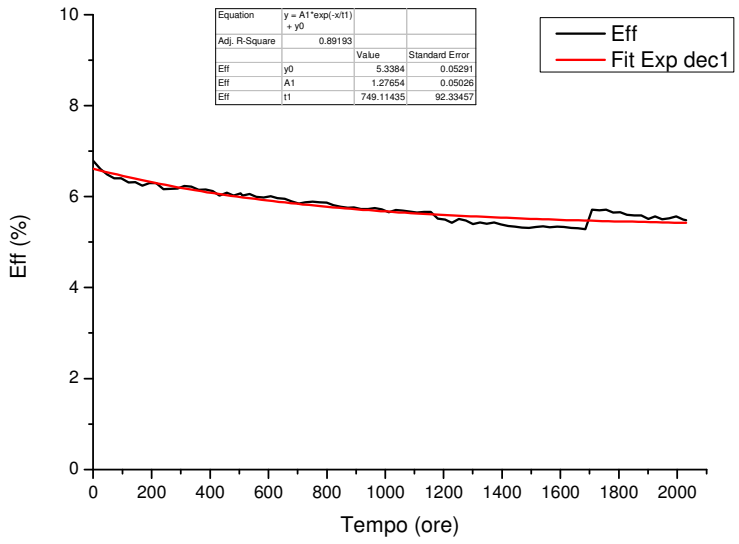

Fig. 59: Efficiency vs Time device Q_4 cell 2_a

Looking at Fig. 59 we can see that the efficiency trend is monotonously decreasing with a slope more pronounced during the first 150 hours, during the following hours the decrease was slower and it seems almost to stabilize around a value of about 5.4%. The loss at the end of test, as previously mentioned, it is approximately of the 20%.

The discontinuity in the efficiency curve, around at 1100 hours and then around 1700 hours, is mainly due to two reasons:

1) At approximately 1100 hours the sun P_{inc} was 0.8 while at the next control (1700 hours) was 0.68 sun. This decline may have been due to a partial deterioration of the light bulb and / or an incidental move of the light source during the positioning of new samples. At about 1700 hours P_{inc} was reported at the value of 0.8 sun.
2) At around of 1700 hours the outer contact of the device (silver paste), partially oxidized, was regenerated with the placing of new silver paste. This may have caused a decrease in series resistance due to contacts and so increased the value of the efficiency detected.

The efficiency curve seems to be fitted well through grade 1 exponential decay curve, as shown in Fig. 59.

Whilst the device performance in terms of efficiency detected under the sun simulator (1000 W/m^2 AM1,5 25°C ± 0,5 °C xenon arch lamp) it is shown in Fig. 60. Also in this case there is the presence of a more pronounced decrease in efficiency during the first operating period, while the subsequent trend seems to remain constant at a value of about 4.8%.

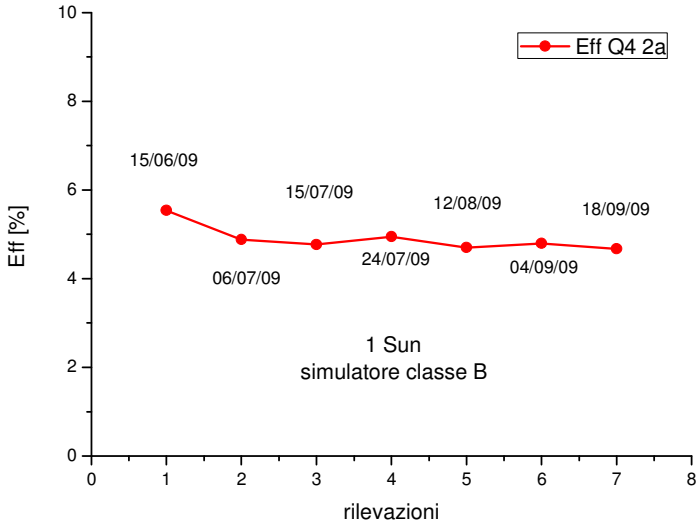

Fig. 60: efficiency vs time under sun simulator

In this case the lost in efficiency is of the 16%.

To better understand the behavior of the solar cell there will be presented the analysis of the others characteristic electrical parameters (J_{sc} & V_{oc}) vs time measured under sun simulator and light soaker.

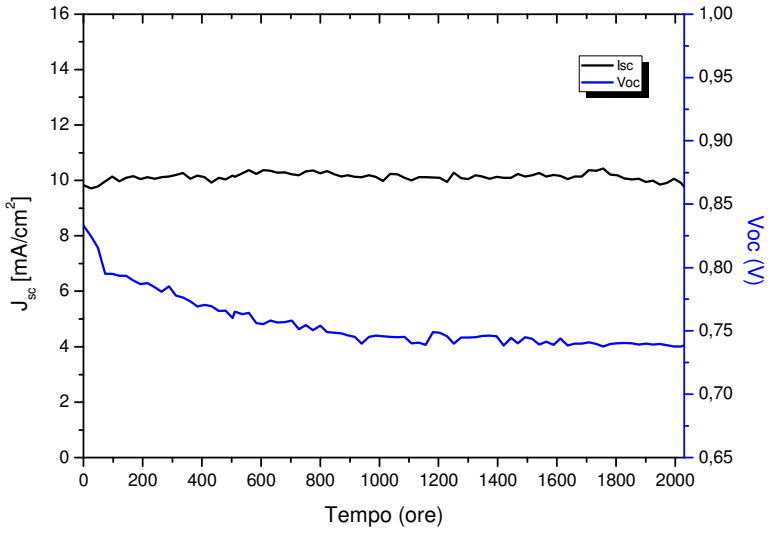

Fig. 61: J_{sc} and V_{oc} vs time under light soaker

In Fig. 61 it is shown the time evolution of short circuit current density (Jsc) and open circuit voltage (V_{oc}) under light soaker . What it can be seen it is an almost monotonous decreasing trend of V_{oc} with a loss of about 11.3%. Concerning the J_{sc} it is can be observed a quick and short initial decay followed, in the middle part, by a practically monotonous increasing trend, whilst at the end curve it is present an almost constant trend. The J_{sc} end value returns about at the same value of the beginning and both curves have a slope more pronounced during the first hours of operation.

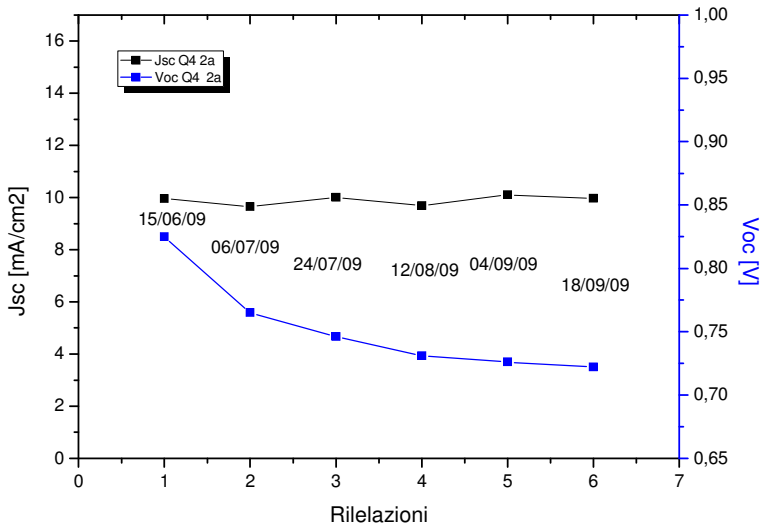

Fig. 62: J_{sc} and V_{oc} vs time under sun simulator

In Fig. 62 it is shown the reference J_{sc} and the reference V_{oc} vs time trend detected under sun simulator in standard conditions. It can be observed that the J_{sc} slowly assume an increasing trend after a beginning stabilization and also in this case, at the end of the test, its value is practically the same of the starting one. Whilst The V_{oc} trend decrease almost monotonically, most evidently in the first part of the test leading to obtain at the end to a loss of about 12,5%.

Tab. 7: Test percentage variation of the principal cell electrical parameters

Stress P_{max}	Eff	V_{oc}	J_{sc}	FF
Light soaker (0,8 sun)	-20%	-11,3%	0%	-8,5%
Sun simulator (1 sun)	-16%	-12,5%	0%	-4%

In Tab. 7 there are reported the percentage variations of the principal electrical parameters detected under light soaker and sun simulator (the negative marker imply that the final value is minor of the beginning one).

In Fig. 63 is shown the comparison of the IV characteristics of the cell detected during the reference measurements under sun simulator. In this figure it can be observed what shown in Fig. 62, but also how the FF (fill factor) change. In this case all the changing are concentrated in the first part of the test keeping a constant trend in the remaining part.

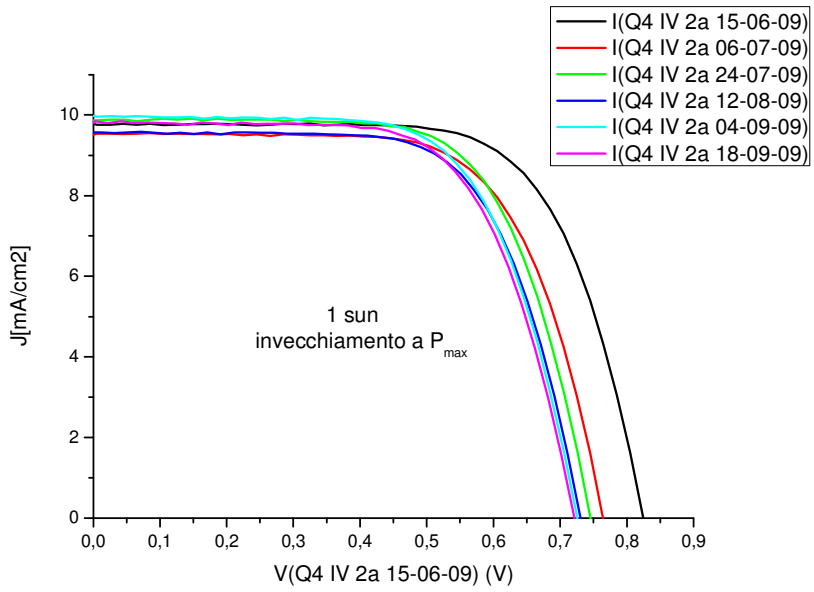

Fig. 63: Comparison of the IV curves detected during the reference measurements under sun simulator

In Fig. 64 it can be observed the comparison of the PV (power to voltage) curves detected during the reference measurements under sun simulator. The P_{max} point decrease drastically in the first part of the test keeping constantly in the in the rest part of the experience and moving progressively at lower voltage points.

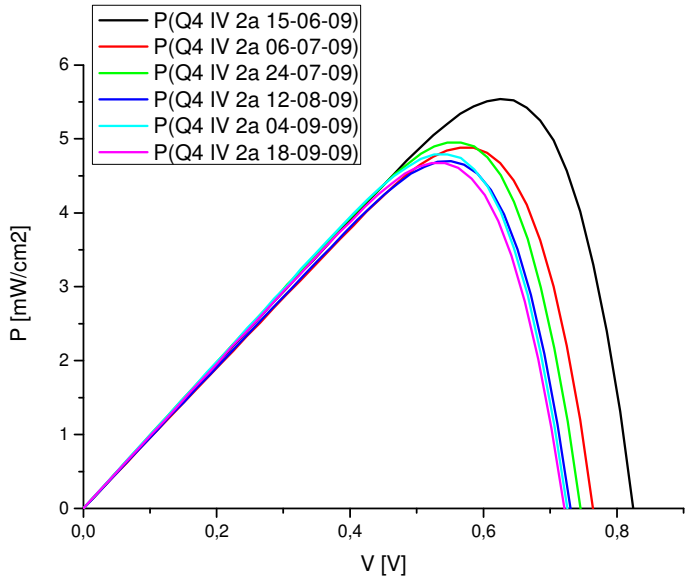

Fig. 64: Comparison of the PV curves detected during the reference measurements under sun simulator

To understand the internal dynamics of the cell and to see what it changes inside the device during time it was performed a series of electronic spectroscopy impedance reference measurements (EIS). These analysis it were performed under sun simulator with an incidence power of 1000 W/m^2 AM1.5 at 25°C ± 0,5 °C.

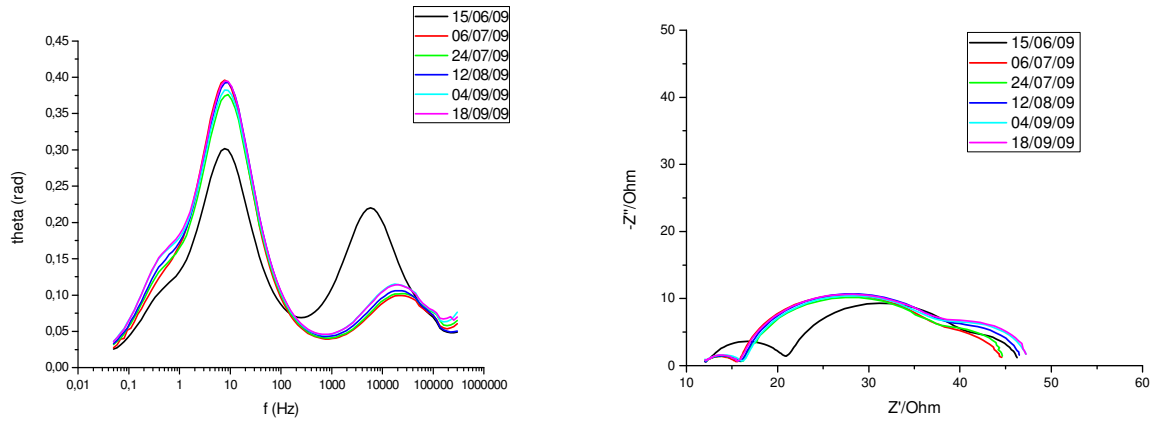

Fig. 65: Comparison of the EIS reference measurements of device Q_4 cell 2_a a) Bode diagram b) Nyquist diagram normalized at minimum starting value

Fig. 65 shows the comparison of Bode and Nyquist plots obtained with impedance spectroscopy around Voc. Measurements were normalized to the minimum starting value for two reasons:

1. To better observe the changes on the counterelectrode between a curve and its subsequent.
2. The starting value of the Nyquist curve was not constant over time (if it was it could imply a possible deterioration of the FTO) and its change is attributable, probably, only by not correct positioning of the contacts during reference measurements (Fig. 66).

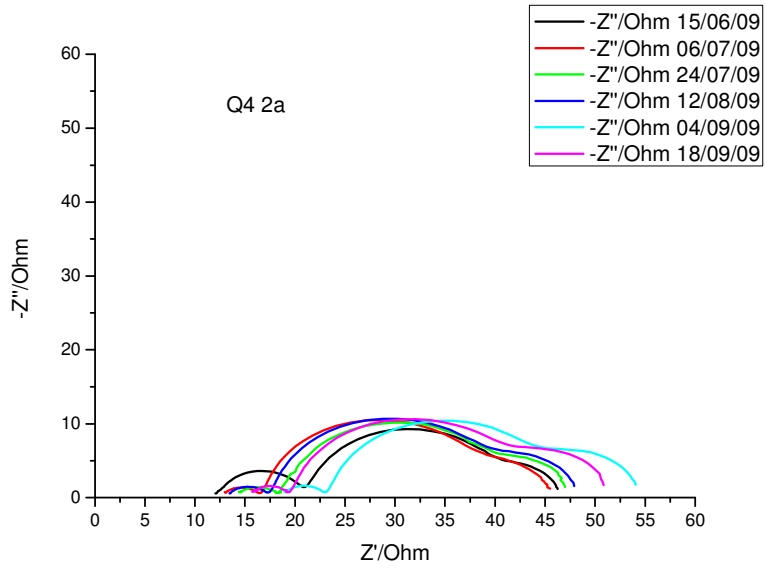

Fig. 66: Comparison of EIS diagrams (Nyqist diagram) not normalized at minimum starting value

Looking at the curve part that refers to the counter electrode on the Nyquist diagram (first semicircle, low resistance in Fig. 65b) what that can be observed is a decrease in charge transfer resistance. This decrease indicates the presence of a catalyst activation process, this phenomenon occurred during the first days of testing. Table 2 shows the values of constant phase elements (CPEct) and the resistance to charge transfer (R_{ct}) of the equivalent circuit (circ1) and the lifetime of the charge on the counter electrode (τ_{ct}).

Tab. 8: counter electrode constant phase elements, charge transfer resistance and minimum charge lifetime.

	CPE_{ct}			
	Y_0 [S*sec^n]	N	R_{ct} [Ω]	T_{ct} [sec]
Start	1,84E-5	0,8536	8,837	3,6E-5
End	5,093E-5	0,7117	4,556	7,8E-6

In the Bode plot Fig. 65a there is a shift of the peak relative to the interface between electrolyte and counter electrode towards higher frequencies, which means a reduction of the lifetime of the electron τ_{ct} (EQ1) (faster recombination) and therefore a more rapid reduction of iodine (Tab. 8). To obtain the equivalent circuit parameters the curves have been fit using the program ZsimpWin3.21 referring to the following model:

R(QR)(QR)O circ1

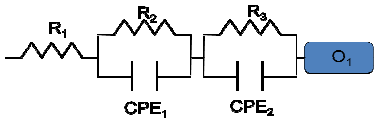

Always from the Bode diagram it can be observed that the peak frequency relative to TiO_2 - electrolyte interface remains almost stable. This value appears to be about 8 Hz (Fig. 65a), this implies that the lifetime of the electron inside the TiO_2 layer (τ) is approximately 20 ms (Eq1) (Table 3).

$$\tau \approx \frac{1}{2\pi f}$$

Eq.1: electron lifetime

Tab. 9: maximum frequency of nyquist plot and life time of the charge relative to the TiO_2 – electrolyte interface

	f [Hz]	T_{pe} [sec]
Start	7,76	20,5E-3
End	7,76	20,5E-3

Fig. 67 shows how the lifetime and the relative frequency varie during the test period. As you can see the trend is practically stable.

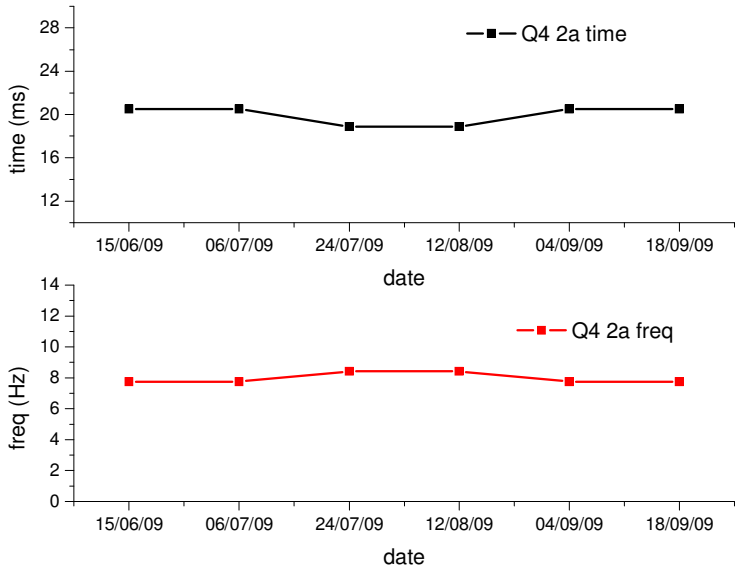

Fig. 67: charge lifetime and relative peak frequency trend

After the information obtained from the analysis of data on the interface between TiO_2 and counter electrode, let's see what happens in the electrolyte itself. With this type of measure what you are going to observed is the phenomenon of electronic diffusion. Its trend is clearly visible in Fig. 65b (Nyquist diagram) at a high resistance as an increase in the value of the diffusive resistance (enlargement of the second semicircle to the right), but also, albeit in a less clear way in Fig. 65a (Bode plot) at low frequencies (300 mHz) through a "shift" to lower values of the characteristic frequency peak. An increase in diffusive resistance of the electrolyte solution represents a major difficulty for ions to pass through the electrolyte itself. One reason for this phenomenon is the decrease in I_3^- ion concentration that may be due to various reasons such as, for example, leakage of electrolyte solution and / or contamination with environment compounds, especially oxygen and water, this because of an incorrect sealing. Precisely the role of oxygen and water is crucial in the deterioration of the solar cell, it has been observed that these elements in the presence of light (photo-bleaching) react irreversibly with the electrolyte components going, even if indirectly, to reduce the concentration of I_3^- ions and to form H^+ (the latter responsible of the sag of the pH and then of the partial desorption of the dye) Eq2 and Eq3.

$$2D^+ + 3I^- + 4O_2 + H_2O \underset{h\upsilon}{\Rightarrow} 3IO_3^- + 2H^+ + 2D \qquad \text{eq2}$$

$$I_{2+}I^- \Leftrightarrow I_3^- \qquad \text{eq3}$$

4.5.2 *Device Q_4 cell 1_a and 3_a aged under V_{oc}*

The active areas in question have been subjected to a light soaking stress with a incident power of 0.8 W/m2, AM 1.5 and constant temperature of 25 ° C ± 1.5 ° C. For the time between a detection and its subsequent the cell was kept on open-circuit voltage.

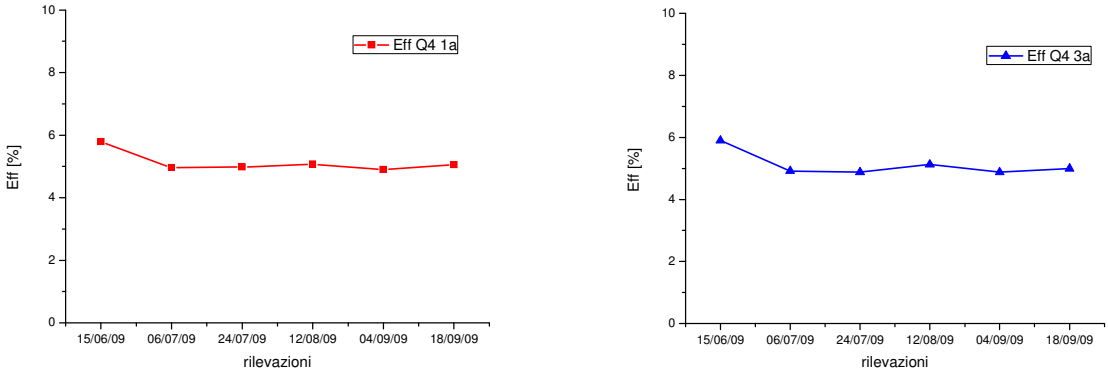

Fig. 68: Cells efficiency overtime a) Device Q_4 cell 1_a b) Device Q_4 cell 3_a

In Fig. 68, respectively, there is presented the efficiency trends of the first and third active area of device Q_4. In these cases, as it happened in the cell stressed at maximum power, it can be noted that the decrease in efficiency occurs almost entirely during the first days of operation, then the trend remains fairly constant around a value of 4,9% for both the active areas. At the end of the test period the efficiency decay was approximately 16% for both cells.

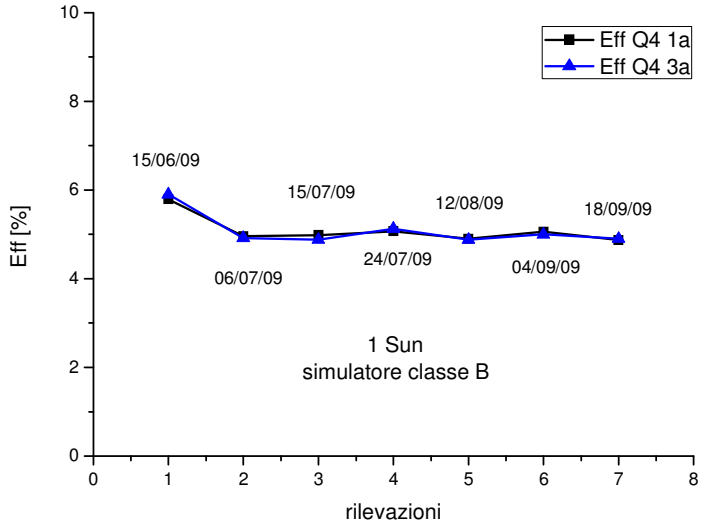

Fig. 69: Efficiency trend comparison of the cell aged at V_{oc}

In Fig. 69, shows the comparison between the efficiencies seen separately in Fig. 68, in this plot it can appreciate the performance repeatability of active areas built with the same process on the same substrate.

Fig. 70 shows the values of J_{sc} and V_{oc} trends of the device Q_4 respectively of cell 1_a and 3_a under sun simulator. As shown in the figure below the trends of the two solar cells are almost identical, this shows a good degree of repeatability in the construction of the devices and cells.

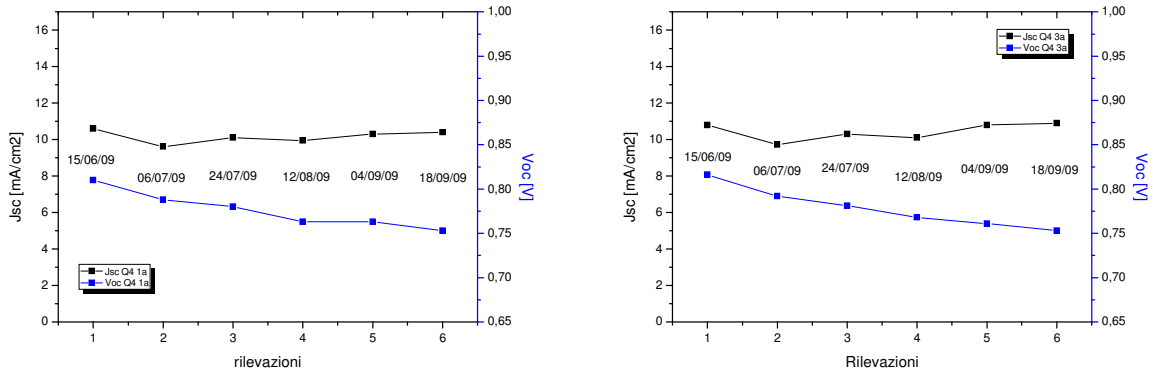

Fig. 70: J_{sc} and V_{oc} trend under sun simulator

The open circuit voltage for both cases decreases monotonously of about 5%, while the short circuit current density after an initial decline start to grow back, almost going to recover at the end of testing what lost during the stabilization of the first part of the test. Tab. 10 summarizes the initial and final values of the main electrical parameters of the cells in question.

Tab. 10: Main electrical parameters of cell 1_a and 3_a of the device Q_4

		V_{oc} [V]	J_{sc} [mA/cm^2]	FF [%]	ŋ [%]
Q4 1a	Start	0,8	10,6	67,4	5,7
	End	0,753	10,3	62,59	4,87
Q4 3a	Start	0,816	10,8	66,95	5,9
	End	0,753	10,9	59,45	4,9

To better observe the entire current to voltage characteristics overtime Fig. 71 shows the comparison of individual characteristics detected with a period of 20 days.
In this figure it can be noted what mentioned about the Fig. 70, but also the trend of the FF overtime, what can be noted is that, if we exclude the major period of adjustment, the trend has remained virtually constant, going to loose a few percentage points between the start and the end of the test.

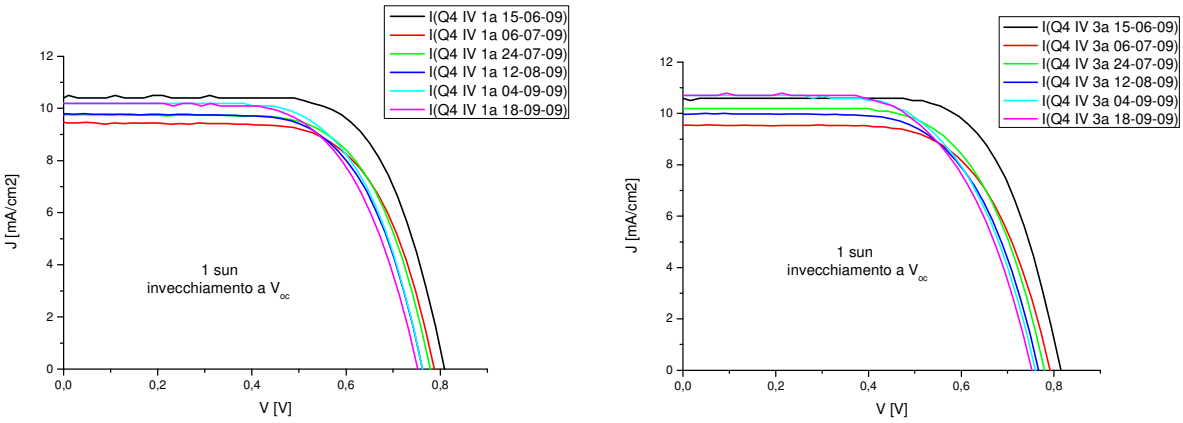

Fig. 71: Current to voltage characteristics overtime of device Q_4 cells 1_a and 3_a

Figure 20 shows the comparison of the power to voltage characteristics detected during the entire test with a cadence of 20 days under sun simulator. The curves trend of the two active areas are very similar and show a more marked drop in power during the first testing period and then an almost stabilization. The maximum power point had an ups and downs trend, in fact after a first decrease it slightly returned to rise and then remained almost constant, but moving at the same time to smaller voltages.

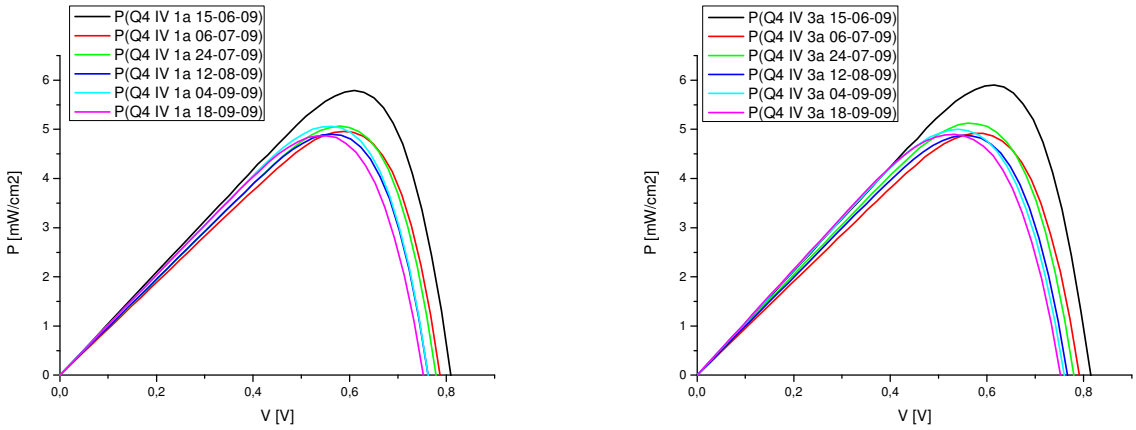

Fig. 72: Power to voltage characteristics overtime of device Q_4 cells 1_a and 3_a

To understand the internal dynamics of the cell and to see what it changes inside the device during time it was performed a series of electronic spectroscopy impedance reference measurements (EIS). These analysis it were performed under sun simulator with an incidence power of 1000 W/m^2 AM1.5 at 25°C ± 0,5 °C.

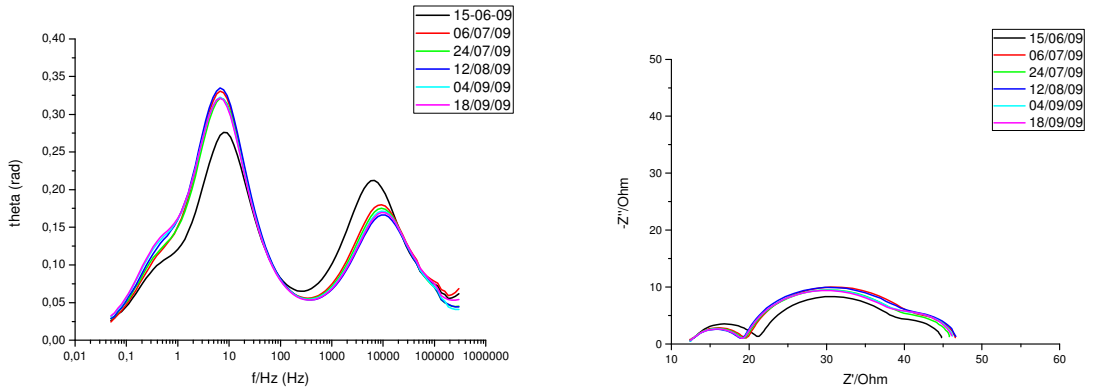

Fig. 73: Comparison of Bode and Nyquist diagram of the device Q_4 cell 1_a normalized at minimum starting value

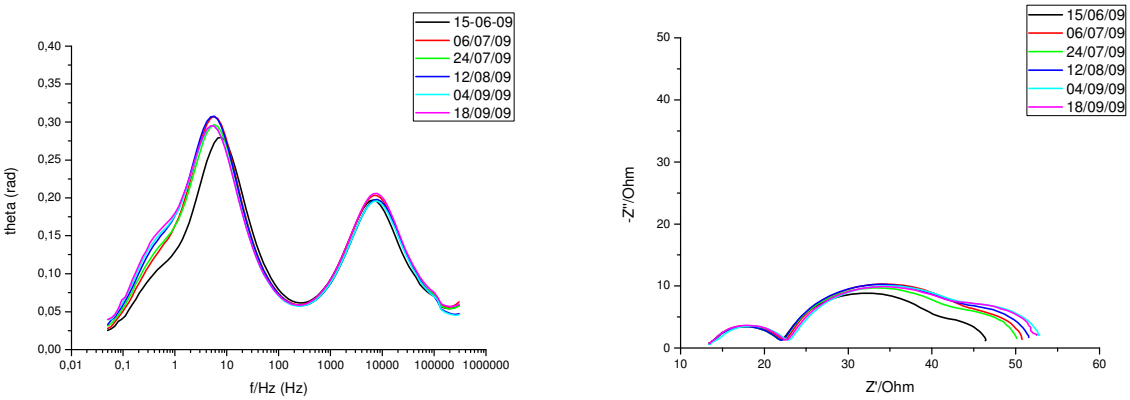

Fig. 74: Comparison of Bode and Nyquist diagram of the device Q_4 cell 3_a normalized at minimum starting value

In Fig. 73 and Fig. 74 are reported the comparison of Bode and Nyquist plots obtained from the electronic impedance spectroscopy reference measurements around V_{oc}. The measurements were normalized to the minimum starting value for the reasons stated in the case of the device Q_4 2_a. For completeness in Fig. 75 shows the comparison of measures of EIS (Nyquist diagram) without normalization to minimum starting value.

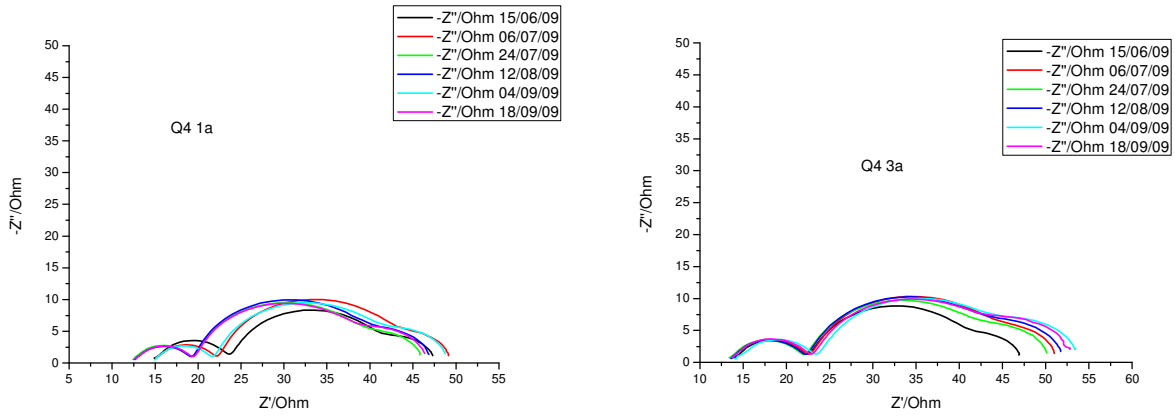

Fig. 75: Comparison of Nyquist diagrams of device Q_4 cell 1_a and 3_a

Looking at the semicircle relative to the counter electrode on Nyquist diagram (first semicircle, low resistance in Fig. 73b and Fig. 74b) what we can deduce is that for devise Q_4 cell 1_a that there has been an activation of the catalyst during the first hours of operation and then stabilization, it means a more efficient catalysis. In the cell 3_a of the device Q_4 is not appreciable any improvement or worsening of the catalysis process during the test period. Tab. 11 shows the initial and final values of the constant phase elements, the charge transfer resistance and time constant for the equivalent circuit of the counter electrode.

Tab. 11: initial and final values of the constant phase elements, the charge transfer resistance and time constant for the equivalent circuit of the counter electrode

	CPE_{ct}			
	Y_0 [S*sec^n]	N	R_{ct} [Ω]	T_{ct} [sec]
Q_4 1_a Start	1,886E-5	0,845	8,753	3,34E-5
Q_4 1_a End	2,238E-5	0,811	6,978	2,025E-5
Q_4 3_a Start	2,019E-5	0,8357	8,632	3,18E-5
Q_4 3_a End	1,727E-5	0,8376	9,108	2,88E-5

In Bode plot (Fig. 73a and Fig. 74a) it can be observed, for both devices, a shift of the frequency peak relative to the interface between electrolyte and counter electrode towards higher frequencies, this implies a reduction in the lifetime of the electron τ_{ct} (Eq1) on the counter electrode (faster recombination) and therefore a more rapid reduction of iodine (Tab. 11). The curves obtained have been fit to obtain the equivalent circuit using the program ZsimpWin3.21 referring to the following model:

R(QR)(QR)O

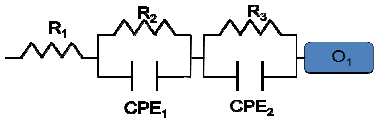

In the Bode plot is can be also observed that the peak frequency, this time referred to the TiO_2 - electrolyte interface, moves to lower frequencies during the first part of the test and then remain stable, this shift is a bit 'more evident in the cell 3_a of the device Q_4. In Tab. 12 there are reported the values of frequency peak referred to the TiO_2 - electrolyte interface of the cell 1_a and 3_a of the device Q_4. This values are derived from the lifetime values of the electron inside the TiO_2 layer (τ) (Eq1) Tab. 12.

Tab. 12: Frequency peak and charge lifetime values of the cell 1_a and 3_a of the device Q_4 at the beginning and at the end of the test

		f [Hz]	τ_{pe} [sec]
Q_4 1_a	Start	7,76	20,5E-3
	End	6,63	24E-3
Q_4 2_a	Start	776	20,5E-3
	End	5,25	30E-3

For both cells in Nyquist diagram it can be observed (Fig. 73b and in Fig. 74b) an enlargement towards right of the semicircle at high resistance (relative to electronic diffusion). This imply an increment of the diffusion resistance of the ionic solutions, that can indicate, as it was mentioned in previous paragraphs, a decries of I_3^- ions concentrations.

In Fig. 76 and Fig. 77 it is reported how the electron lifetime in the TiO_2 and its relative frequency peak vary overtime for the two cell analyzed. How it can be observe the increase is respectively of the 20% and of the 50%.

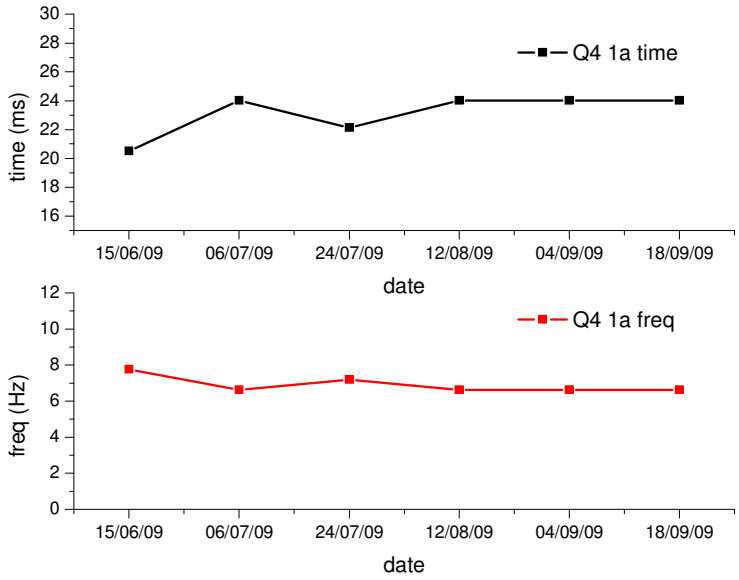

Fig. 76: Electron lifetime and relative frequency peak trend overtime of the cell 1_a of device Q_4

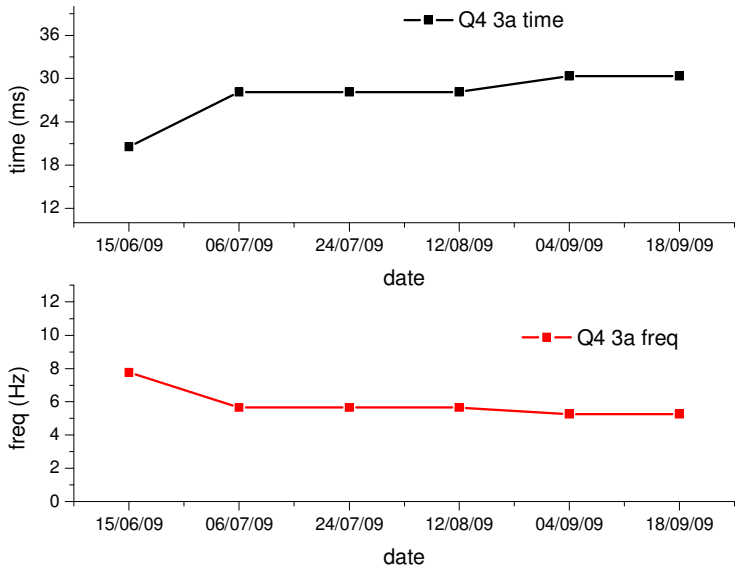

Fig. 77: Electron lifetime and relative frequency peak trend overtime of the cell 3_a of device Q_4

4.6 Comparison of cells aged under P_{max} and under V_{oc}

Analyzing the data obtained from the cells of the device Q_4 and looking at their efficiencies overtime it can be observed that the ageing performed under light at V_{oc} and P_{max} give very similar results (Fig. 78). For both ageing types, during the first part of the test, it can be observed the presence of a decries in efficiency, whilst in the rest part of the experience practically no further decries have been detected. From the point of view of the internal equilibrium of the cell the two ageing types produced different changes on the single electrical parameters, anyhow they compensate each other producing the same electrical response (same efficiency trend). The only notable thing is that the V_{oc} ageing produce a fasten stabilization of the device (Fig. 78).

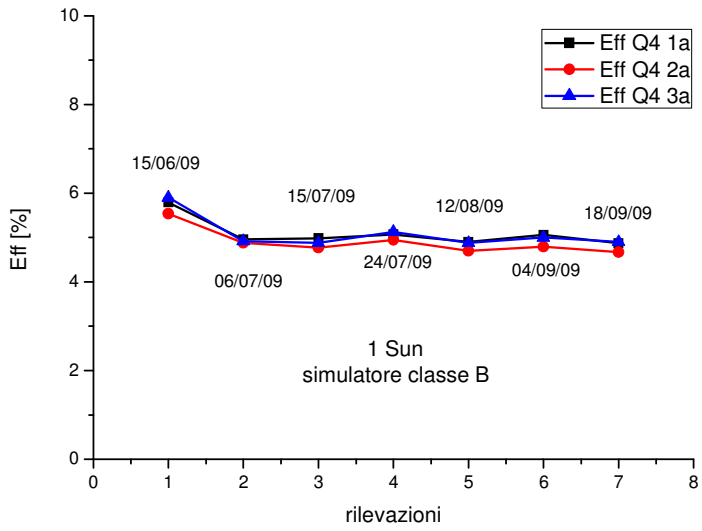

Fig. 78: Comparison of efficiency trends of the cells aged at V_{oc} and at P_{max}

4.7 2000 hours test result

In the previous paragraphs it was shown an example of the trend overtime of cells aged under light soaker (0,8 sun and A.M. 1,5 or 1 sun and A.M. 1,5), stressed at open circuit voltage and at their own maximum power point. In this paragraph there will presented, instead, the comparison of the efficiency trends of all the cells used in this experience, it will shown the entire curves and curves parts comparison, differentiating them on first test period (stabilization) and rest of the test (stable curve).

4.7.1 Comparison of all cells aged at V_{oc}

In Fig. 79 it is shown the comparison of the entire efficiencies trends curves off all the cells aged at V_{oc} , this figure show that the trends follow practically the same profiles showing in all cases that the loose in efficiency occurs in the first test period (about in the first 150 – 200 hours, as it can be seen in previous paragraphs efficiency trends figures obtained under light soaker).

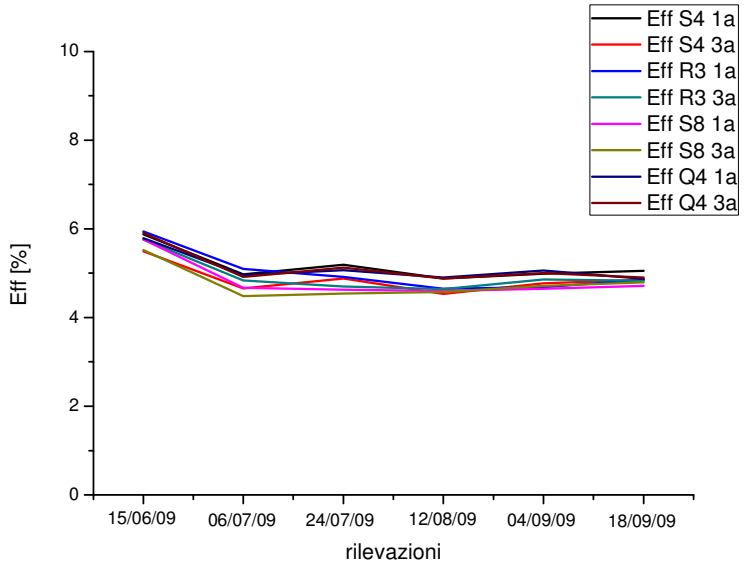

Fig. 79: Comparison of all efficiency trends curves obtained from reference measurements under sun simulator (entire curves)

If we do not consider the first part of the test (stabilization) the efficiency curve assumes a constant trend as it can seen in Fig. 80.

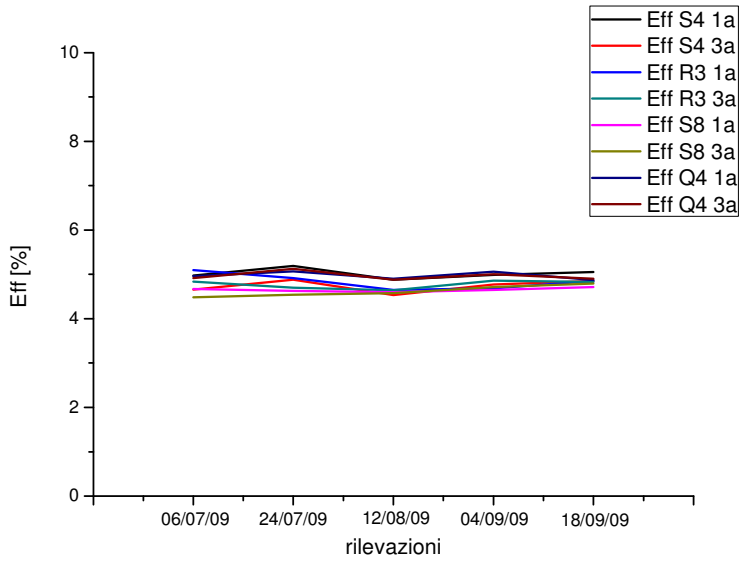

Fig. 80: Comparison of all efficiency trends curves obtained from reference measurements under sun simulator (only stable curves)

This stabilization process it must be considered in the case of evaluation of real performance of a DSC solar cell, something analogous at what occurs in the standard test of the amorphous silicon.

As it can be seen in Fig. 79 e Fig. 80 the efficiencies curves trends are very similar, differentiating each other practically only for the starting values, this small differences are due to construction process, in fact some construction passages are still manually.

In Fig. 81 is reported the mean of the efficiencies trends presented in Fig. 79 (all the cells aged at V_{oc}) with its standard deviation.

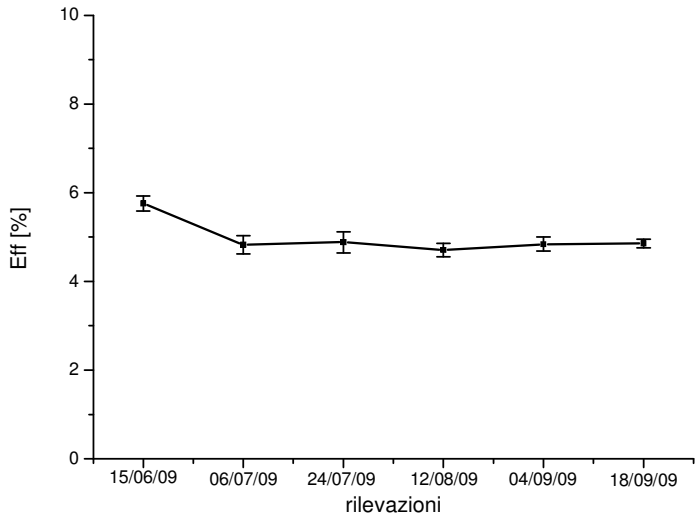

Fig. 81: Mean of efficiencies trends of the cells aged at V_{oc}

In tab. 13 in the first three rows there are reported the efficiencies values respectively of the starting of the entire curve, of the starting of the curve without the stabilization period and of the end of the curve. In the following three rows there are shown the differences between the efficiencies starting values of the entire curve and the curve without the stabilization period, the total decries in efficiency and the decries or rise (values with + before) in efficiency of the curve without the stabilization period.

tab. 13: Differences between the efficiencies of the entire period (E) and the ones without stabilization period (WS) of cells aged at V_{oc}

	Q_4 1_a	Q_4 3_a	S_8 1_a	S_8 3_a	S_4 1_a	S_4 3_a	R_3 1_a	R_3 3_a	Mean [%]
Eff [%] starting value (E)	5,79	5,9	5,76	5,52	5,88	5,49	5,94	5,76	5,75
Eff [%] starting value (WS)	4,96	4,92	4,67	4,48	4,97	4,66	5,1	4,84	4,82
Eff [%] end value	4,87	4,9	4,71	4,79	5,05	4,85	4,85	4,83	4,85
difference [%] (E) starting – (WS) starting	14,4	16,5	19	19	15,5	15	14,5	16	16,2
$Diff_{start-end}$ [%] (E)	16	17	18	13	14	12	18	16	15,5
$Diff_{start-end}$ [%] (WS)	2	0,5	**+1**	**+6,5**	**+1,5**	**+4**	5	0,3	**+0,65**

Indeed , from Fig. 79, Fig. 80 and from tab. 13 we can deduce that to consider a cell stable it has to be fist wait a stabilization period of about 150-200 hours to be spent under light soaking (0,8 sun, 1.5 AM and 25 °C) at open circuit voltage. In fact if the measurements would have been started after the observed stabilization period the variation of the efficiency after 2000 h test would has a mean of + 0,65 % .

The attendance of a stabilization period before the evaluation of a cell performance it is clear to be necessary, the open point is to find if and how to accelerate this stabilization process. As mentioned before this ageing test was performed under light

soaker 0,8 sun, AM1.5 at a 25 °C ± 1,5 °C, further tests are in progress to understand which is the right combination among thermal-electric-light stresses to obtain the best result, that is how to achieve a faster stabilization.

4.7.2 *Comparison of all cells aged at P_{max}*

The P_{max} stress result to be little harden than the one at V_{oc} , in fact taking in consideration all the cells used in this experience the decries of the mean of the efficiencies at the end of test for the first case is about 20,5 % against the 15,5 % of the second type of stress. Also in this case the greater part of the decries in efficiency is achieved in the first 200 hours, but for this type of stress the complete stabilization is achieved in a much longer time, about 1500 - 1800 hours . If we would not consider the stabilization period (150-200 hours) at the end of the test the decries in efficiency would has been of about 8,5 %, as it can be seen in Fig. 82 and Fig. 83, that is just a bit less of the middle of the entire efficiency decries.

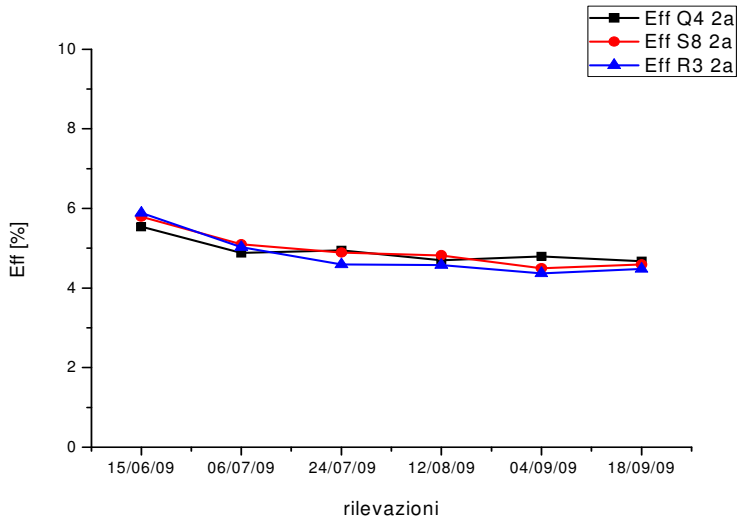

Fig. 82 Comparison of efficiencies trends of cells aged at P_{max} (entire curve)

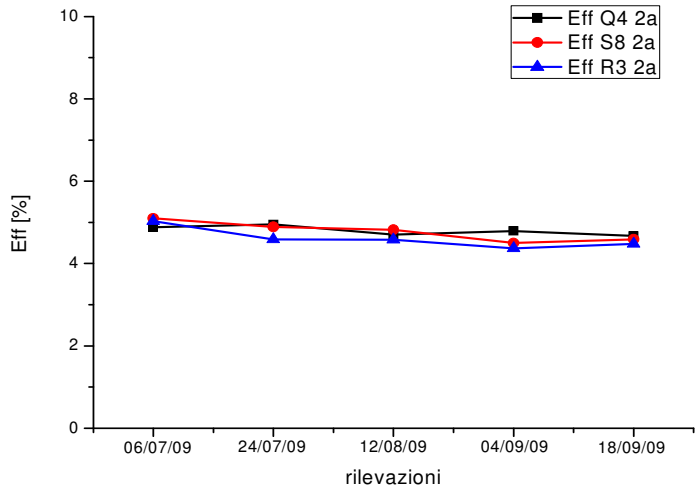

Fig. 83: comparison of efficiencies trends of cells aged at P_{max} (without stabilization period)

In Tab. 14 in the first three rows there are reported respectively the starting efficiency value of the entire curve (E), the starting efficiency value of the curve without the stabilization period (WS) and the end value. In the following three rows there are reported the decries between the entire curve and the curve without the stabilization period efficiencies starting values, the complete efficiencies decries and the efficiencies decries of the cases without the stabilization periods.

Tab. 14: Differences between the efficiencies of the entire period (E) and the ones without stabilization period (WS) of cells aged at P_{max}

	Q_4 2_a	S_8 2_a	R_3 2_a	Mean [%]
Eff [%] starting value (E)	5,54	5,79	5,89	5,74
Eff [%] starting value (WS)	4,88	5,1	5,03	5,03
Eff [%] end value	4,67	4,59	4,48	4,58
Difference [%] starting (E) – starting (WS)	12	12	15	13
$Diff_{start-end}$ [%] (E)	16	21	24	20,03
$Diff_{start-end}$ [%] (WS)	4	10	11	8,3

Also in this case, as it happens for the stress at V_{oc} , the singles cells efficiencies curves trends are very similar, differentiating each other practically only for the starting values, this small differences are due to construction process, in fact some construction passages are still manually. In Fig. 84 there is reported the curve of the means of the efficiencies of the cells aged at P_{max} with its standard deviation, here it can be observed that the stabilization is achieved only after 1500 – 1800 hours, much later than of what happens in the case of the ageing at V_{oc} .

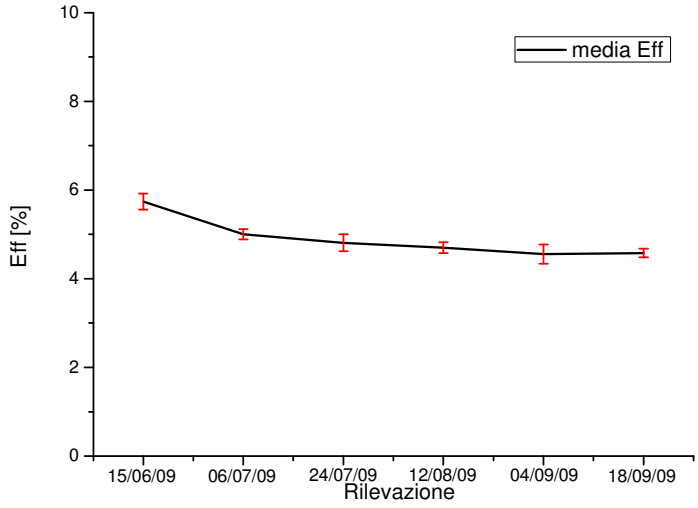

Fig. 84: means of efficiencies of the cell aged at P_{max} with its own standard deviation.

The curve can be fit quite good with an ExpDec1 as it can be observed in Fig. 85, especially in the last part of the curve.

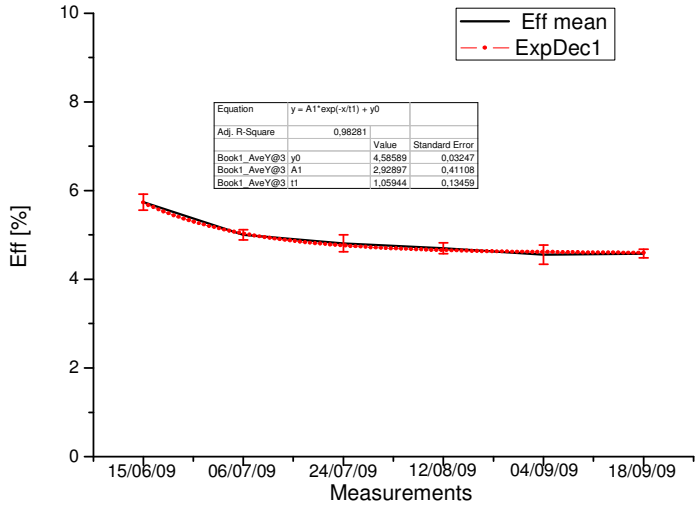

Fig. 85: Comparison between the efficiencies trend and an ExpDec1 curve

the extrapolated values of the obtained curve are reported in Tab. 15

Tab. 15: ExpDec1 extrapolated values

Equation	y = A1*exp(-x/t1) + y0	
Adj. R-Square	0,98281	
	Value	Standard Error
y0	4,58589	0,03247
A1	2,92897	0,41108
t1	1,05944	0,13459

4.7.3 *Comparison of the mean of the efficiencies trends of the two stress analyzed*

Analyzing the efficiencies trends comparison of aging at V_{oc} and P_{max} appears that using the first type of stress (V_{oc}) the cell quickly reaches stability in efficiency. In fact, as mentioned in previous paragraphs, the efficiency trend in this case becomes stable after about 200 hours, whilst if we consider the second stress type (P_{max}), the efficiency reaches a stable trend only after about 1600 hours. What exposed it can be observed in Fig. 86.

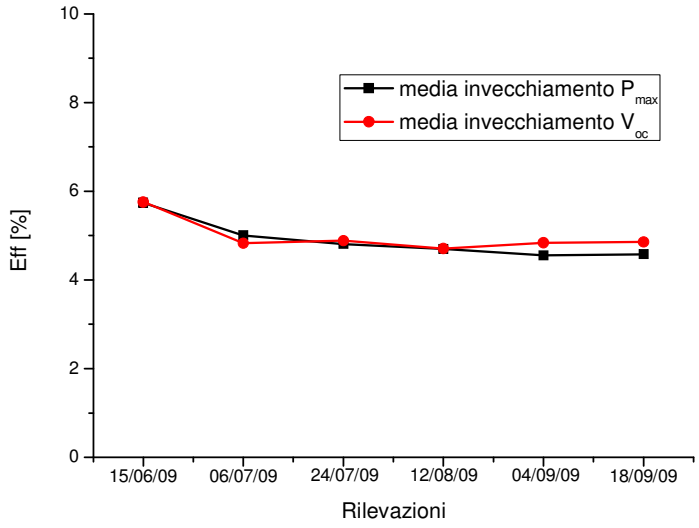

Fig. 86: Comparison of the means of efficiencies trends for the two types of tress analyzed (V_{oc} and P_{max})

4.7.4 *Eis data analysis*

From the analysis of EIS data, in all the cases analyzed, it has been observed that in the first part test (about 200 hours) there is an improvement on the catalysis effect on the counter electrode (this means an highest speed reduction of the electrolyte) and an increase in the life time of the electron in the TiO_2 layer (greater chance of being taken on external contacts). Both these effects, after the initial variation, remained roughly constant.

Concerning the electrolyte, there was a progressive enlargement of the diffusive ion curve over time especially during the first part of the test, most evident in the curves relative to the cells aged at P_{max}. This phenomenon is reflected in an increase of the diffusive resistance of the ionic solution, in a first approximation (considering constant or pseudo constant the diffusion coefficient of ionic species itself) this can be attributed to a decrease of the I_3^- ion concentration. This phenomenon is due, probably even if indirectly, to a non-hermetic sealing which allow oxygen and moisture to go in contact with the liquid electrolyte. Those elements, in the presence of light radiation (especially UV component), bind irreversibly with the I^- ions. The reduction in concentration of the latter produce a decrease of the I_3^- ions, since the two species are related dall'Eq2 and Eq3. This effect is particularly evident in the cases where there was a visible polluting of the electrolyte solution by moisture and oxygen.

5. Conclusions

My Ph.D. experience has begun nearly with the start of the research on DSC in Tor Vergata. This combination of events permitted me to analyze the greatest part of the aspects of this technologies, but also it led to the fact that during these three years my job has not been concentrated on a single line of project, but as people and efforts involved increased it has been more and more focused.

In these three years, thanks to funds of Lazio region the activity of Tor Vergata on DSC has expanded considerably (Polo solare organico regione Lazio) so my tasks have been gradually specialized in certain areas, leaving progressively project lines that became too heavy to be carried out alone. The main areas where I worked on have been:

- Sealing materials and procedures
- Indoor ageing test

As the best redox couple for DSC applications is also one of the most aggressive, among the dozens of different types of glues and resins tested, as primary and secondary sealer, only one of them proved to be potentially a good candidate to be used in DSC technology, all the others sealers tested revealed interaction with the electrolyte compounds since the beginning. This sealer is a UV curable Urethane acrylates based special epoxy. This resin has shown a very good resistance against the electrolyte compounds, but only at temperatures under 50 °C. Higher temperatures catalyze chemical reactions between the resin and the electrolyte leading to the crystallization of the sealer and consequently to the leakage of the electrolyte. A functionalization of the main molecule of this special epoxy can provide a good alternative to the classical thermoplastics. In parallel it was also demonstrated that UV curable technology can be used in DSC construction process without damaging the cell elements with a big saving of time and energy (very relevant in view of an industrialization).

Efficient pre-treatments were identified to be applied to thermoplastic Bynel to improve its sealing characteristics (no primers applied). 65°C one night in a ventilated

oven storage with and without active vacuum permits the cell to resist to 80°C 3 days thermal stress , whilst a microwave 30 seconds at 700W bynel pre-treatment was found that can let the cell resist to a 100°C 3 days thermal stress without any apparent structural modifications. Also going down in temperature (2°C test and -18°C test) it didn't produced any structural modifications of the devices. From the EIS analysis it appears that the diffusion resistance gradually increase after each temperature step (from room temperature to 80°C), whilst in parallel the charge transfer resistance decrease. Whilst considering the cold thermal stress the EIS measurements revealed an increase of the charge transfer resistance, this increase is reversible, in fact, after another 80°C test the R_{ct} decreases again.

The 2000 h ageing test under light soaking, with and without load applied, revealed that the devices present a transient before to achieve a constant trend in terms of photo to current conversion efficiency (ŋ). Doubtless to establish if there is and how long is the transient period of a DSC solar cell is fundamental in an industrialization optics, something similar to what happen for the amorphous silicon (*CEI/IEC 61646*). It was observed that the speed with which the device reaches its stability in performance depends strongly on which kind of stress is applied at the cell during the transient period. In fact it was demonstrated that leaving cells under light soaking (0,8 sun AM 1,5) at 25°C at open circuit voltage leads to reach the stability after 150-200 hours (about 1 week), whilst leaving devices under the same conditions, but this time stressed at maximum power point, the stability is reached only after about 1500 hours (nearly two months and a half). Also in this case the greatest part of the loss in performance happen in the first about 200 hours of testing (such as at V_{oc}), but this time the loss continues also if in a progressively less evident manner. Test are ongoing to fasten this transient period combining these and others type of stress with different operating temperatures and incident powers. The electron impedance spectroscopy analysis (EIS) revealed that during the transient some changing occurs inside the internal dynamics of the cell, new equilibria are reached. In particular the charge transfer resistance decries (positive effect), whilst the recombination resistance and the diffusion resistance increase (respectively positive and negative effects), the last in a more strongly way. The reduction in concentration of I_3^- ions seems to be the main cause of efficiency loss. In fact the diffusion resistance (R_{dif}) of devices stressed at V_{oc} after the first increase (in the first 150 hours) keeps more or less constant (from 150 h to end test), practically following the photo to current efficiency conversion trend.

What said is confirmed from the P_{max} stressed devices too, in fact in this case the increase of R_{dif} is less marked, but more progressive in reaching the stabilization value and this trend mirror itself in the fact that the stabilization in photo to current efficiency conversion occurs only after about 1500 hours. Comparing the performances of the two type of stresses overtime it appears that the loss is efficiency (ŋ), in P_{max} case, it is some percentage points higher than the one at V_{oc} .

In the Appendix there are shown the effects of the polluting of the electrolyte solution by air and moisture on internal dynamics and electrical parameters. A contamination of such elements produces a progressive reduction of I_3^- ions concentration in the electrolyte solution and then to a constant increase of the R_{dif}, this lead to a monotonic decries of the photo to current efficiency conversion value overtime.

6. Appendix

In the following paragraphs there are presented the differences in terms of performance and internal dynamics changing between a properly and not properly well sealed cell.

6.1 A quite well sealed cell

In this paragraph there is reported an example of a cell that can be considered sealed quite well, in fact this device, excluding the first stabilization period, remained constantly on the same efficiency value without notable changing in the others electrical parameters. The adopted sealing it is not hermetic, so some little changing are visible, especially on the diffusion resistance, but in this case this increases resulted very small.

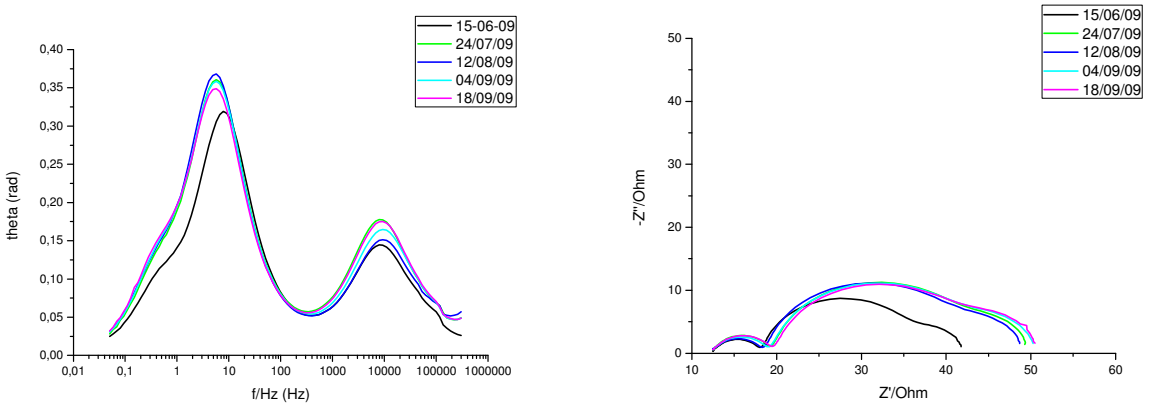

Fig. 87: Comparison of the Bode and Nyquist diagrams of the cell S_8 1_a

In Fig. 87 there are reported the Bode and Nyquist diagrams obtained from the reference measurements of the cell S_8 1_a , if we do not consider the first curve, the rest of the curves are quite similar presenting very small differences. This performance was achieved thanks to a quite good sealing procedure that isolated quite well the internal compounds from the interaction with the moisture and oxygen.

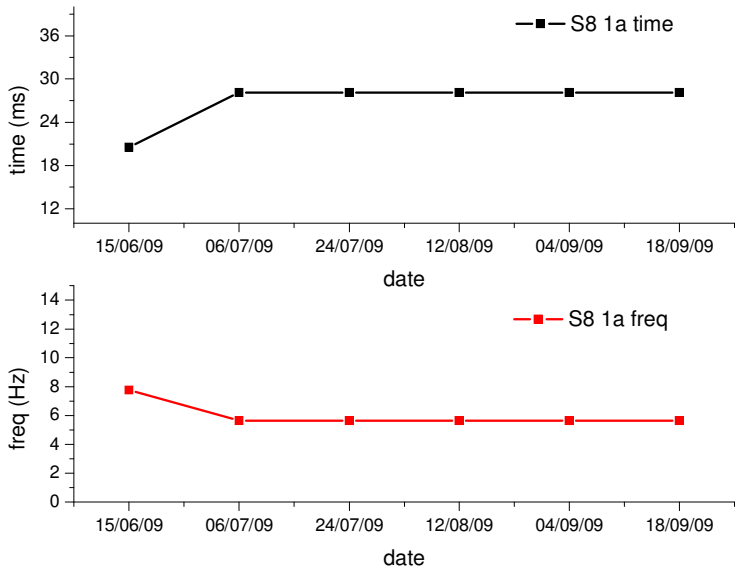

Fig. 88: Electron time life in the TiO_2 layer over time

Also the life time of the charge in the TiO_2 layer remains constant over time excluding the starting value (Fig. 88), this value is about 28,1E-3 seconds.

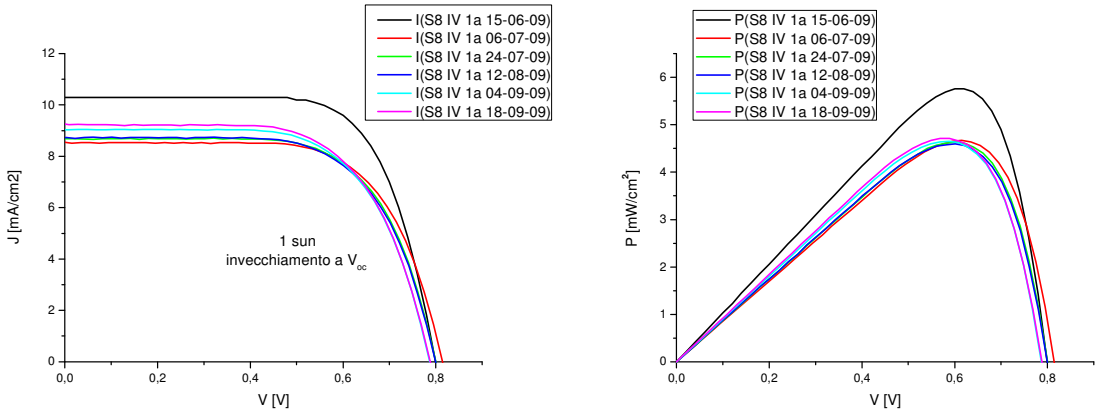

Fig. 89: Comparison of the IV and PV curves obtained from the reference measurement of the cell S_8 1_a

What previously stated is reflected also looking at the main electrical parameters (Current density, voltage and output power), in fact looking at Fig. 89 it can be appreciate the stability of this cell (always excluding the stabilization period).

6.2 Not properly well sealed cell

In this paragraph there is presented an example of a not properly sealed cell, in this device something went wrong during the main lamination process, this reflected in a progressive polluting of the electrolyte solutions by moisture and oxygen during the ageing test Fig. 90.

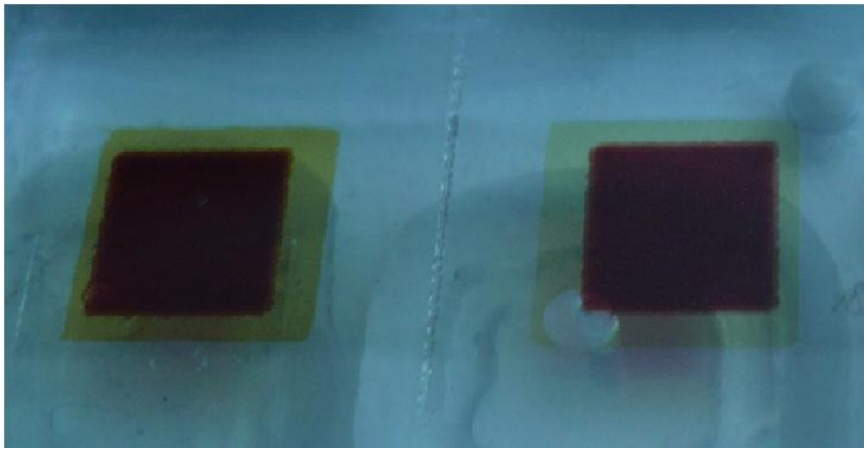

Fig. 90: Cell properly sealed (left) and polluted by moisture and oxygen (right)

Until the middle of the test the efficiency trend is similar to the ones of the other cells involved in this test, then the main lamination ceased to be efficient and an air bubble, progressively larger, appear in the internal chamber and the orange color, typical of the electrolyte, started to become more clearer. After the appearance of these phenomena the efficiency trend stated to go down again (Fig. 91).

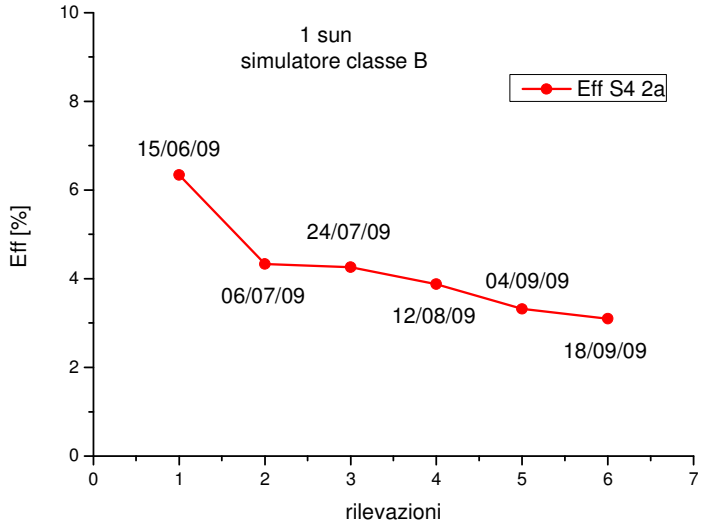

Fig. 91: Efficiency trend over time of the cell S_4 2_a

If we analyze what happened to the J_{sc} and to V_{oc} (short circuit density and open circuit voltage) trends (Fig. 92) we note that between the two electrical parameters the one that has been the greater decrease was the short circuit current density.

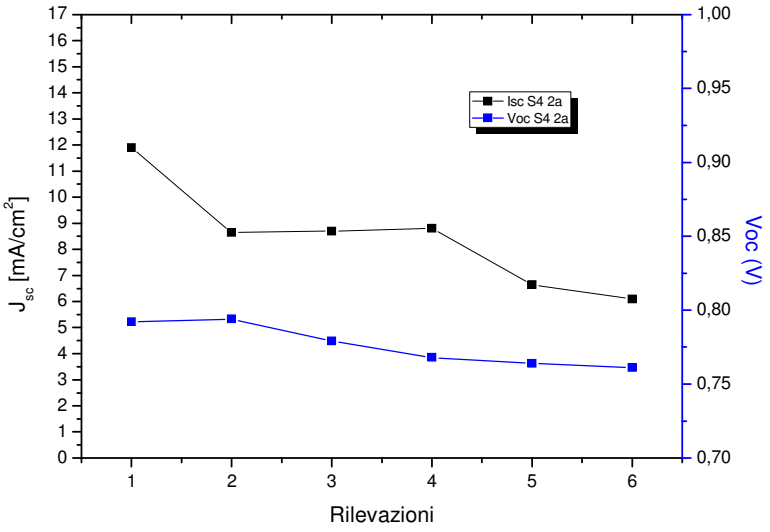

Fig. 92: J_{sc} and V_{oc} trend over time of the cell S_4 2_a

In Tab. 16 there are reported the percentage variations of the main electrical parameters of this cell.

Tab. 16: Percentage variations of the main electrical parameters of the cell S_4 2_a

Stress P_{max}	Eff	V_{oc}	I_{sc}	FF
Sun simulator (1 sun)	-49%	-4%	-44%	+1%

The strong reduction in the efficiency is due to the drop of the short circuit density so it is interesting to see how the IV and PV curves evolves over time, the P_{max} point decries with time and also in this case the current component (I_{max}) is the one that drop down, whilst the voltage component (V_{max}) remains practically constant (Fig. 93).

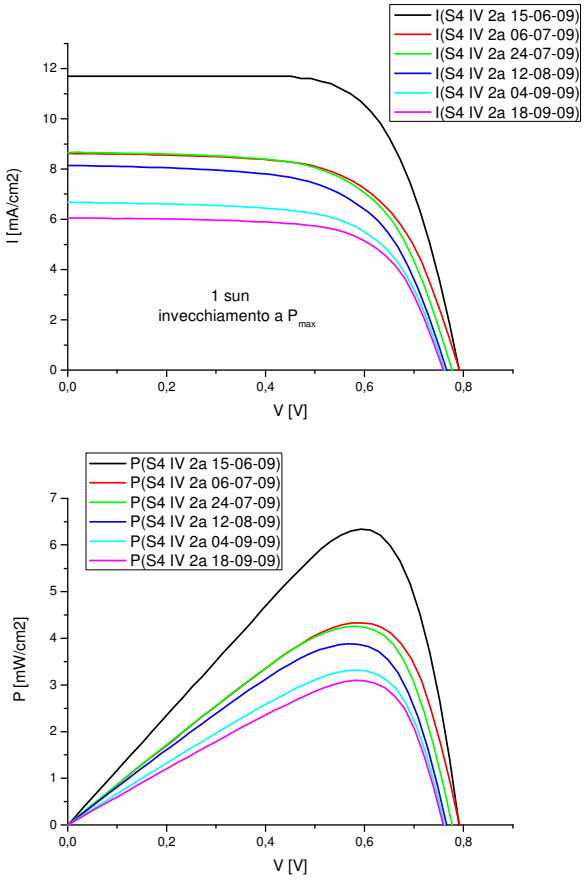

Fig. 93: Comparison of IV and PV curves of the device S_4 2_a

From the analysis of the reference EIS measurements we can observe which parts of the cell are damaged from the interaction with oxygen and moisture. In Fig. 94 there is presented the comparison between all the reference EIS measurements detected overtime.

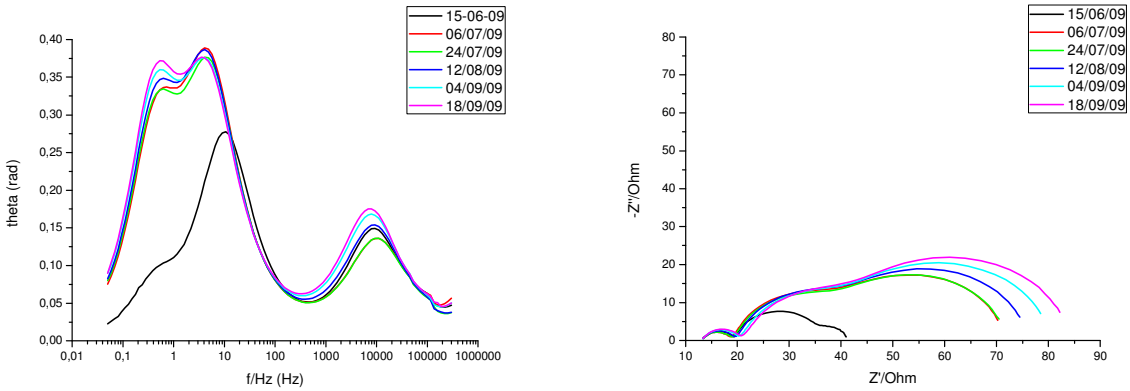

Fig. 94: Comparison of Eis measurement Of the device S_4 2_a a) Bode diagram b) Nyquist diagram

In this figure it is particularly evident that the component of the cell that has been damaged most was the electrolyte. For example in the Nyquist diagram (Fig. 94b) at high resistance is located the part of the curve that represent the ionic diffusion (third semicircle), it enlarge very much toward higher resistances overtime, this means that the diffusion resistance increase. This increase is mainly due the reduction of I_3^- ions concentrations, the causes of this phenomena was discussed in previous chapters.

7. Acknowledgements

Special tanks go to professors, friends and colleagues who helped and supported me during these three years, they are too many to be reported one by one, they will remain always in my thoughts and in my heart.

Thanks also to the people with whom I had discussions, these events made me grow and become ever more consciousness of my qualities.

Thanks above all to my parents and my brothers that with their sacrifices have allowed me to get to this point.

A very big thanks to the other two parts of my heart Ines and my little Sara, I cannot find words that can express how they have been me helpful to go forward.

And last, but not the least thanks to myself, without my determination I have give up long ago accepting offers of which today I would certainly regret.

8. Publications

Papers published on international journals in printing 2010:

- Enrico Leonardi, Stefano Penna, Thomas M. Brown, Aldo Di Carlo , Andrea Reale,
  Stability of Dye-sensitized Solar Cells under light soaking test

  Journal of non crystalline solid

Other publications in journals or conference, or book chapters:

- F.De Rossi, F. Giorgulli, P. Chiella, E. Leonardi,A. Reale*, T. Brown, A.Di Carlo
  Comparative Study of Natural and Synthetic Dyes for Dye Sensitized

  Solar Cells

  ICOE 2007

- T. M. Brown, P. Chiella, F. Giorgulli, M. Cecchetti, F. De RossiM. Suriano, E. Leonardi, A. Reale, A. Di Carlo, F. Giannini
  Dye Sensitized Solar Cells: Materials and Engineering

  Gruppo di elettronica 2007

- F. De Rossi, F. Giorgulli, P. Chiella, M. Cecchetti, E. Leonardi, A. Reale, T. M. Brown, A. Di Carlo
  Textile and Food Dyes for Dye-Sensitized Solar Cells

  ECOER 2007

Publications in journals or international conference produced before the beginning of the PhD:

- A. Reale, A. Di Carlo, F. Giannini, F. Brunetti, E. Leonardi, M. Lucci, M.L: Terranova , S.Orlanducci , E. Tamburri, F. Toschi, V. Sessa. **Nanocomposites for Organic and Hybrid Organic-Inorganic Solar Cells**

  SPIE 2006

- F. Toschi, E. Tamburri, S. Orlanducci, V. Sessa , M. L. Terranova, M. Lucci, A. Reale, A. Di Carlo, E. Leonardi
  Nanosized titania and carbon nanotubes for new generation photovoltaic cells

  NANOFASICI 2006

9. Bibliography

1. **Gerischer, H. and Tributsch, H.** 437-445, s.l. : Phys. Chem., 1968, Vol. 72.

2. **Tributsch, H. and Gerischer, H.** 251-260, s.l. : Phys. Chem., 1969, Vol. 73.

3. **Anderson, S.** 571-573, s.l. : Nature, 1979, Vol. 280.

4. *Faraday Discuss.* **Dare-Edwards, M., al., et and Faraday Discuss. Chem. Soc. 70, 285–298 (1980).** 285-298, s.l. : Chem. Soc., 1980, Vol. 70.

5. **Mohammad, K., Graetzell, M. and al, et.** 16835-16847, s.l. : J. AM. CHEM. SOC., 2005, Vol. 127.

6. **Nazeeruddin, Md., Péchy, P. and Graetzel, M. Chem. Commun. 1705–1706 (1997).** 1705-1706, s.l. : Chem. Commun. , 1997.

7. **Nazeeruddin, Md. and Chem. Soc. 123, 1613–1624 (2001).** 1613-1624, s.l. : Chem. Soc. , 2001, Vol. 123.

8. *Metal Complexes as Photosensitizers in Photoelectrochemical cells.* **Kalyanasundaram, K. and Graetzel, M.** 247-271, Dordrecht, Netherlands : Kluwer Academic Publishers, 1993.

9. **Hagfeldt, A. Graetzel, M.** 269-277, s.l. : Acc. Chem. Res., 2000, Vol. 33.

10. **Laque, A. and Hegedus, S.** *Handbook of Photovoltaic Science and Engineering.* s.l. : Wiley, 2003. ISBN 0-471-49196-9.

11. **Argazzi, R. and al., et.** 5741-5749, s.l. : Inorg. Chem., 1994, Vol. 33.

12. **Sayama, K., et al.** 3825-3832, s.l. : Chem. Mater, 1998, Vol. 10.

13. **Liu, Y., et al.** 267-281, s.l. : Sol. Energy Mater. Sol. Cells, 1998, Vol. 55.

14. **Hara, K., al., et and 70, 151–161 (2001).** 151-161, s.l. : Sol. Energy Mater. Sol. Cells, 2001, Vol. 70.

15. **Nazeeruddin, Md. and al., et.** 6382-6390, s.l. : J. Am. Chem. Soc, 1993, Vol. 115.

16. **Vlachopoulos, N., et al.** 1216-1220, s.l. : J. Am. Chem. Soc., 1988, Vol. 110.

17. **Kalyanasundaram, K. Graetzel, M.** 347-414, s.l. : Coord. Chem. Rev, 1998, Vol. 77.

18. *Light-Induced Redox Reactions in Nanocrystalline Systems.* **Hagfeldt, A. and Grätzel, M.** s.l. : Chemical Reviews, 1995, Vols. 95(1): 49-68.

19. **Zaban, A., Ferrere, S. and Gregg, B.** 452-460, s.l. : J. Phys. Chem. B , 1998, Vol. 102.

20. **Tachibana, Y. and al., et.** 20056-20062, s.l. : J. Phys. Chem. , 1996, Vol. 100.

21. **Huber, R., et al.** 6494-6499, s.l. : J. Phys. Chem. B , 2002, Vol. 106.

22. **Hannappel, T., et al.** 6799-6802, s.l. : J. Phys. Chem. B, 1997, Vol. 101.

23. *Interfacial Electron Transfer Dynamics of Photosensitized Zinc Oxide Nanoclusters.* **Murakoshi, K., et al.** 221-238, Washington, DC : American chemical society, 1997.

24. **Asbury, J., Wang, Y. and Lian, T.** 6643–6647, s.l. : J. Phys. Chem. B , 1999, Vol. 103.

25. **Asbury, J. and al., et.** 4545–4557, s.l. : J. Phys. Chem. B , 2001, Vol. 105.

26. **Tachibana, Y. and al., et.** 1198-1205, s.l. : J. Phys. Chem. B, 2000, Vol. 104.

27. **Huber, R. and al., et.** 8995–9003, s.l. : J. Phys. Chem. B, 2000, Vol. 104.

28. **Haque, S., et al.** 1745–1749, s.l. : J. Phys. Chem. B, 1998, Vol. 102.

29. **Kuciauskas, D., al., et and B, J. Phys. Chem.** 392-403, s.l. : J. Phys. Chem. B, 2001, Vol. 105.

30. **Nasr, S., Hotchandani, S. and Kamat, P.** 4944–4951, s.l. : J. Phys. Chem. B, 1998, Vol. 102.

31. **Huang, S. and al., et.** 2576–2582, s.l. : J. Phys. Chem. B, 1997, Vol. 101.

32. **Kumar, A., Santangelo, P. and Lewis, N.** 834–842 , s.l. : J. Phys. Chem., 1992, Vol. 96.

33. **Stanley, A. and Matthews, D.** 1293–1300 , s.l. : Aust. J. Chem., 1995, Vol. 48.

34. **Gregg, B., et al.** 1422–1429, s.l. : J. Phys. Chem. B, 2001, Vol. 105.

35. **Salafsky, J., et al.** 766–769, s.l. : J. Phys. Chem. B, 1998, Vol. 102.

36. **Cao, F., et al.** 17021–17027 , s.l. : J. Phys. Chem. B, 1996, Vol. 100.

37. **Kambe, S. and al., et.** 2967–2972, s.l. : J. Phys. Chem. B, 2002, Vol. 106.

38. **Sommeling, P. and al., et.** 399–410, s.l. : Sol. Energy Mater. Sol. Cells, 2000, Vol. 62.

39. **Schwarzburg, K. and Willig, F.** 2520–2522, s.l. : Appl. Phys. Lett., 1991, Vol. 58.

40. **Konenkamp, R., Henniger, R. and Hoyer, P.** 7328–7330, s.l. : J. Phys. Chem., 1993, Vol. 97.

41. **Wah.l A, Augustynski J, J. Phys. Chem. B 102, 7820–7828 (1998).**

42. **Solbrand, A. and al., et.** 2514–2518, s.l. : J. Phys. Chem. B, 1997, Vol. 101.

43. **Solbrand, A. and al., et.** 1078–1083 , s.l. : J. Phys. Chem. B , 1999, Vol. 103.

44. **Smestad, G., Bignozzi, C. and Argazzi, R.** 259–273, s.l. : Sol. Energy Mater. Sol. Cells , 1994, Vol. 32.

45. **Smestad, G.** 157-178, s.l. : Sol. Energy Mater. Sol. Cells, 1998, Vol. 55.

46. *Cyclic tetrapyrrole based molecules for dye-sensitized solar cells.* **X.F.Wang and H.Tamiak.** 2010, energy & enviromental science, pp. 3, 94-106.

47. **S.Ito and H.Miura.** 2008, chem.commun., pp. 5194-5196.

48. *Conversion of Light to Electricity by Cis-X2bis(2,2'-Bipyridyl-4,4'-Dicarboxylate)Ruthenium(Ii) Charge-Transfer Sensitizers (X= Cl-, Br-, I-, Cn-, and Scn-) on Nanocrystalline Tio2 Electrodes.* **Nazeeruddin, M. K., et al.** s.l. : Journal of the American Chemical Society, 1993, Vols. 115(14): 6382-6390.

49. *Untersuchung zum Elektronentransport im nanoporösen TiO2 von.* **Würfel, U.** s.l. : Fakultät für Physik, Albert-Ludwigs Universität, Doctoral dissertation, 2006.

50. *Untersuchungen zur Langzeitstabilität von Farbstoffsolarzellen mittels.* **R.Kern.** s.l. : Fakultät für Physik, Albert-Ludwigs Universität, Doctoral Dissertation , 2001.

51. *Electron transport and back reaction in dye sensitised nanocrystalline photovoltaic cells.* **Peter, L. M. and Wijayantha, K. G. U.** s.l. : Electrochimica Acta, 2000, Vols. 45(28):4543-4551.

52. *How Important is the Back Reaction of Electrons via the Substrate in Dye-Sensitized Nanocrystalline Solar Cells?* **Cameron, P., Peter, L. and Hore, S.** s.l. : J. Phys. Chem. B, 2005, Vols. 109: 930-936.

53. *Influence of scattering layers on efficiency of dye-sensitized solar cells.* **Hore, S., et al.** 2006 : Solar Energy Materials and Solar Cells, Vols. 90(9): 1176-1188.

54. **P.Würfel.** s.l. : Physik der Solarzellen. Heidelberg, Spektrum, Akad. Verl., 1995.

55. **H.Ibach and H.Lüth.** s.l. : Festkörperphysik, Einführung in Grundlagen, Springer, 1995.

56. **H.J.Lewerenz, H.Jungblut Photovoltaik, Springer Verlag.** s.l. : Photovoltaik, Springer Verlag, 1995.

57. **P.W.Atkins.** s.l. : Physikalische Chemie, VCH Verlag, 1990.

58. *Instrumental Methods in Electrochemistry.* **Electrochemistry-Group.** Southampton : John Wiley & Sons, 1985.

59. *Diffusion und Grenzflächen an der Platinelektrode in farbstoffsensibilisierten Solarzellen.* **A.Hauch.** s.l. : Fakultät für Physik, Albert-Ludwigs-Universität Diploma Thesis, 1998.

60. *Sonnenenergie: Photovoltaik Teubner Studienbücher.* **A.Goetzberger, B.Voß and J.Knoobloch.** 1994.

61. *On the modeling of the dye-sensitized solar cell.* **R.Stangl, J Ferber and J.Luther.** s.l. : solar Energy Materials and Solar Cells, 1998, Vols. 54(1-4): 255-264.

62. *Modeling of photovoltage and photocurrent in dye-sensitized titanium dioxide solar cells.* **Ferber, J and J.Luther.** s.l. : J. Phys. Chem. B, 2001, Vols. 105(21): 4895-4903.

63. **Sastrawan, Ronald.** Ph.D. Thesis Photovoltaic modules of dye solar cells. Freiburg : s.n., 2006.

64. *A new Palaeolithic discovery: tar-hafted stone tools in a European Mid-Pleistocene bone-bearing bed.* **P.Mazza.** s.l. : Journal of Archaeological Science, 2006, Vol. 33: 1310.

65. *From the Cover: Implications for complex cognition from the hafting of tools with compound adhesives in the Middle Stone Age, South Africa.* **L.Wadley, T.Hodgskiss and M.Grant.** s.l. : Proceedings of the National Academy of Sciences of the United States of America, 2009 june, Vols. 106 (24): 9590–4. ISSN 0027-8424.

66. *Studies in organic archaeometry I: identification of the prehistoric adhesive used by the "Tyrolean Iceman" tofix his weapons.* **F.Sauter, et al.** s.l. : ARKIVOC, 2000, Vols. 1:[5] 735-747.

67. **A Guide to IUPAC Nomenclature of Organic Compounds, Blackwell Scientific Publications, Oxford.** 1993.

68. *Nomenclature of regular single-strand organic polymers.* **J.KAHOVEC, R.B.FOX and K.HATADA.** 1921–1956, s.l. : Pure and Applied Chemistry, 2002, Vol. 74 (10).

69. *Commission on Nomenclature of Organic Chemistry.* s.l. : Blackwell Scientific, 1993.

70. **dymax.** *dymax and electrolux meeting.* 22 september 2009.

71. *TWI.* [Online] 2007. [Cited: 26 gennaio 2010.] http://www.twi.co.uk/content/kssmt001.html.

72. Special Chem. *http://www.specialchem4coatings.com.* [Online] 2010. [Cited: 16 01 2010.] http://www.specialchem4coatings.com/tc/radiation-curing/index.aspx?id=urethane_acrylate.
73. *Long-term stability of low-power dye-sensitised solar cells prepared by industrial methods.* **Pettersson, H and T.Gruszecki.** s.l. : Solar Energy Materials and Solar Cells, 2001, Vols. 70(2): 203-212.
74. *Long-term stability of dye-sensitised solar cells.* **A.Hinsch, et al.** s.l. : Progress in Photovoltaics, 2001, Vols. 9(6): 425-438.
75. *Degradation analysis of dye-sensitized solar cell module after long-term stability test under outdoor working condition.* **Naohiko, K., et al.** 893–897, s.l. : Solar Energy Materials & SolarCells, 2009, Vol. 93.
76. *Photovoltaic performance and long-term stability.* **Grätzel, M.** 578–583, s.l. : C. R. Chimie, 2006578–583, Vol. 9.
77. **A., Wahl., Augustyski, J. and J. Phys. Chem. B 102, 7820–7828 (1998).** 7820–7828 , s.l. : J. Phys. Chem. B, 1998, Vol. 102.